

# STAVEBNÍ OBZOR

ČÍSLO 4/2016

Obsah čísla:

<b>NEGATIVE INTEREST RATES AND HOUSING BUBBLES</b> <i>Stroukal Dominik, Kadeřábková Božena</i>
<b>COMPARISON OF PROPAGATION CHARACTERISTICS OF EXCITED STRESS WAVES IN PILE AND ANCHORAGE WITH BOLT SYSTEMS</b> <i>Zeng Sheng, Zhang Jing and Sun Bing</i>
<b>GEOTECHNICAL PROPERTIES OF LATERITIC SOIL STABILIZED WITH THE ASHES OF OIL PALM FRONDS</b> <i>Nnochiri Emeka and Aderinlewo Olufikayo</i>
<b>HISTORICAL PLASTER COMPOSITION DETECTION USING REFLECTANCE SPECTROSCOPY</b> <i>Matoušková Eva, Hůlková Martina and Šedina Jaroslav</i>
<b>IMPACT OF IMAGE RESOLUTION ON PAVEMENT DISTRESS DETECTION USING PICUCHA METHODOLOGY</b> <i>Salini Reus, Xu Bugao and Souliman Mena</i>
<b>NUMERICAL ANALYSIS OF THE EFFECT OF SURCHARGE ON THE MECHANICAL BEHAVIOR OF GEOCELL REINFORCED RETAINING WALL</b> <i>Song Fei, Chai Haibo, Zhao Jian, Yang Mingrui</i>
<b>SEISMIC ANALYSIS OF NUCLEAR POWER PLANT CANNED MOTOR PUMP UNIT BASED ON INTEGRAL CALCULATION METHOD</b> <i>Zhenggui Li, Muyu Li, Jiarong Zhang, Bo Li, Xiaobing Liu, Fengyu Yang</i>
<b>COMPLEX ANALYSIS AND DOCUMENTATION OF HISTORICAL BUILDINGS USING NEW GEOMATICS METHODS</b> <i>Faltýnová Martina, Raeva Paulina, Poloprutský Zdeněk, Matoušková Eva, Housarová Eliška</i>

## NEGATIVE INTEREST RATES AND HOUSING BUBBLES

*Dominik Stroukal<sup>1</sup>, Božena Kadeřábková<sup>2</sup>*

1 *University of Finance and Administration, Department of Economics and International Relations, Prague, Estonská 500, Czech Republic; stroukal@vsfs.cz*

2 *University of Economics, Faculty of Economics, Department of Economics, Prague, Winston Churchill Square 4, Czech Republic; bozena.kaderabkova@vse.cz*

### ABSTRACT

In years after the financial crisis economists started to propose negative interest rates as a way how to escape from a liquidity trap. Negative interest rate was considered to be impossible but few countries have already set them below the lower zero bound. However, it has been done only in the central banks but not in the commercial banks. The main thesis of this paper is that low interest rates can inflate a housing bubble and as a result negative interest rates would only inflate it more. First, proposals how to make interest rate negative even in commercial banking are presented in the paper. Then we discuss general consequences of negative interest rates such as redistribution, initiation of a business cycle and most importantly, inflation. Finally, we look at the housing market and present theoretical and some empirical evidence of a possible ongoing bubble. The theory suggests that the negative interest rate would inflate the bubble necessarily. Consequences of a later decrease of housing prices have to be taken into account whenever negative interest rates are proposed.

### KEYWORDS

Negative interest rate, transmission mechanism, housing market, business cycle

### INTRODUCTION

It can be said, with a slight exaggeration, that all forms of human entrepreneurship are taxed, except one – the money hoarding. For almost a century policy-makers have been trying to solve this by more or less radical policies. The last attempt seems to be the negative interest rate. Although the negative nominal interest rate was considered to be impossible, proposals that can make it possible have already been presented and some forms of them have been applied. It is proved that this policy of raising the cost of holding money cannot work without a statutory anchor and enforcement. In this paper, we argue that since the originary rate of interest cannot be negative, the whole concept of negative nominal interest rates leads only to inflation of bubbles.

Because of this policy, we can expect higher spending in some sectors and hidden inflation in prices not represented in the consumer price index. We argue that the most notable examples of this inflation are in stocks, bonds and housing. Although all three bubbles can lead to tremendous social problems, we assume that policy makers should be worried most about the housing prices.

## BELOW ZERO

Until publishing the popular papers written by Buiter & Panigirtzoglou [1] and Buiter [2] there was a notable agreement on intuitive conclusion that nominal interest rates cannot be negative. But this constrain has become binding in the recent economic downturn. Policy makers of the USA, EU and especially Japan began thinking about lowering nominal interest rates below their zero bound. And it is not only for the lowering itself. Clearly, the main reason is to widen the field where they can manipulate with the economy but proposals how to do that imply another consequence, with such they can kill two birds with one stone. . As we will see later, those birds are of many forms, but one of them is crucial – inflation.

In 1990s the modern debate about relevancy of monetary policy started in nowadays world. Situation in '90s Japan, now called “the lost decade”, became threatening for them and at least interesting for the rest of the world. According to some economists, Japanese economy was the first economy trapped in the so-called liquidity trap since the big depression [3]. The term liquidity trap was first used by John Maynard Keynes, with a famous notion that he knows “of no example of it [other than an abnormal episode] in the United States at certain dates in 1932.” [4, 207-208]

Many authors, most notably Krugman [5] and Svensson [6], wrote papers opening and rethinking the liquidity trap issue. The second thing strengthening the discussion about this new exciting topic was beginning of the current crisis in 2008. In that time policy-makers “forced” the economists to explain what to do if the liquidity trap occurs. Krugman writes that this is “the third time in history that a major economy has found itself in a liquidity trap.” [3]. One of the solutions how to escape from the liquidity trap is to overcome the zero bound.

The zero bound can be described as a point where the crucial principles of modern macroeconomics stop working and are useless and even counterproductive. It is a remarkable point in the way that to some extent every school of economic thought recognizes here the failure of such instruments as the quantitative easing or interest rates setting. Even increased savings do not increase investment. And the list goes on. This is the point where the liquidity trap occurs.

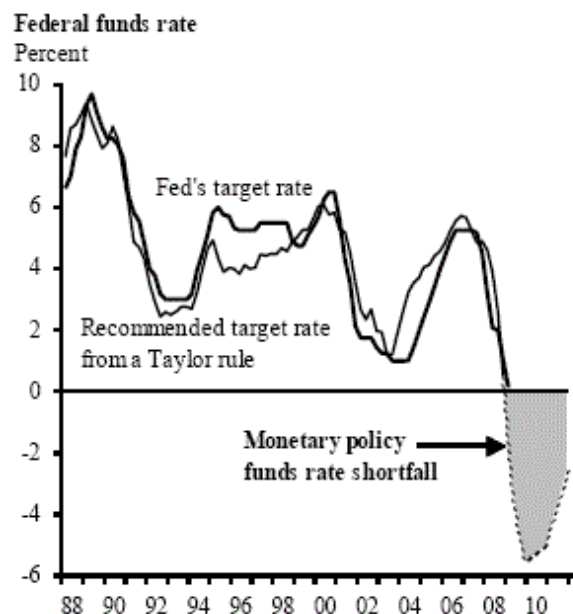


Figure 1 - Recommended target rate from a Taylor rule below zero [6]

At this point the question what to do arises, how to boost the economy when interest rates approach zero but they are still not sufficiently low to do so? How to escape from the trap?

Economists argue, that one of the propositions how to escape from the liquidity trap is the negative interest rate. It is a very simple proposition – going lower will make the boost. Even the Taylor rule had predicted a negative number [7], so economists were put in the belief that the negative interest rate is a must (see *Fig. 1.*). This is a rule for central bank interest rates and it is plausible to do so, and so countries such as Sweden, Switzerland and Japan did. It is even technically possible to set commercial bank interest rate below zero, but who will lend the money if the simple holding of it will earn him more? If holding money yields zero return who wants to earn less by lending it? Keep your money in mattress is always a better choice. Therefore the solution must make the storing in mattress more expensive. How to do that?

If we want to seek the policy that can make holding money more expensive, we have to understand what money we are talking about. There are plenty theories of money and many types and forms, but the only distinction that we have to do for our analysis is to distinguish between the cash and the money on a bank account. These two forms of money differ in costs and benefits.

The benefits of money on bank account are numerous, e.g. the interest or additional services within the bank. The costs might be numerous.

The benefits of cash are mostly connected with its liquidity, but someone uses them to show his wealth or for an art. They have benefits in a market change where the other side has no bank account etc. The costs relate to carrying, storing, stealing, destroying and losing the cash.

If we want to seek the possibilities of rising the costs of holding cash, we can either lower the costs of accounts or the benefits of holding cash. It is also possible to expand the benefits of accounts or the costs of holding. Higher benefits of bank accounts are the result of a market competition, there is not a problem, same as the lower benefits of cash since these two are connected in the term of the opportunity costs. And since the case is about very *low* interest rates (thus low benefits of accounts) the only policy-interesting point is in the rising the costs of holding cash. How?

As we state above, if a policy-maker wants to raise the cost of holding cash it can be done through the rising the cost of carrying or storing it, or the probability of stealing, destroying or losing. Since the rising of a probability is generally expensive (imagine the policy of rising the probability of stealing cash or making the notes “fragile” or “tiny”) and the rising of the cost of carrying it (probably in the form of “heavy” or “very big” notes) too, the only relevant policy is hidden in the increase of the costs of storing the cash. This is the so-called carry tax, a portion of money held that one must pay to a government. An example of such note is shown below in *Fig. 2.* Now it is clear that the policy of imposing the negative interest rate is *de facto* taxation, although more or less unconventional and for this paper most importantly that imposing a carry tax can lower the bound below the zero. I So negative interest rates are possible not only between the banks but also in mortgages and other retail loans.

100 DOLLARS FREE-MONEY														
10 Cents	10 Cents	10 Cents	10 Cents	10 Cents	10 Cents	10 Cents	10 Cents	10 Cents	10 Cents	1 Sept.	6 Oct.	3 Nov.	1 Dec.	
10 Cents	10 Cents	10 Cents	10 Cents	10 Cents	10 Cents	10 Cents	10 Cents	10 Cents	10 Cents	11 Aug.	8 Sept.	13 Oct.	10 Nov.	8 Dec.
10 Cents	10 Cents	10 Cents	10 Cents	10 Cents	10 Cents	10 Cents	10 Cents	10 Cents	10 Cents	18 Aug.	15 Sept.	20 Oct.	17 Nov.	15 Dec.
10 Cents	10 Cents	10 Cents	10 Cents	10 Cents	10 Cents	10 Cents	10 Cents	10 Cents	10 Cents	25 Aug.	22 Sept.	27 Oct.	24 Nov.	22 Dec.
		10 Cents				10 Cents				29 Sept.				29 Dec.

Federal Currency Office, Washington, 1 January 1960

Figure 2 - Gesell's free-money scheme [8]

Economics as a science about human action implies definition of interest rate different from the definition in the Keynesian view of Krugman. His statements about liquidity traps and the negative interest rate are relevant within the Keynesian paradigm, but the crucial juxtaposition lies in the comparison with the paradigm of so-called Austrian school of economic thought.

In the Austrian view the interest rate is the ratio of the value assigned to want-satisfaction in the immediate future and the value assigned to want-satisfaction in remoter periods of the future. This interest rate is called the *originary* rate of interest. Originary interest is a category of human action and as such it can be shown that it cannot be negative or zero. "The reason of this arises not because capital is productive, nor out of man's psychology. Rather, it is embedded in the very concept of human action." [9, 121]. The very reason for this lies in the concept of time-preferences that are always, for everyone and in every situation, positive.

The Austrian business cycle theory explains that it is mainly the low interest rate set by the central bank lower than the originary rate what leads to the business cycle. Since the originary rate of interest cannot be negative and every nominal negative interest rate thus leads to the business cycle, what is the purpose of the negative interest rate?

In our previous discussion we have found the negative interest rate capable of keeping the monetary policy working, whatever are the consequences.

Despite these facts, why there are still those who support it? What are the incentives to support such policy? They can be of three kinds, policy-makers can benefit from the carry the tax politically (through reelection), directly (in business) or they do not know the consequences.

As Mises [10] shows complexly, with grace Parkinson [11] or finally Buchanan [12], these incentives can be based on strengthening the political position of the policy-maker, most often a reelection. What side-effects are so desirable?

It lasts for centuries, but in the roughest form from exactly 1936, from the publishing of Keynes' General Theory of Employment, Interest and Money [4]; the most desirable side-effect is definitely to boost the aggregate demand. Why? According to Krugman [13]: "When the economy is in a liquidity trap, *government spending should expand up to the point at which full employment is restored*" (emphasis in the original). And how? Since the tax holding money is costlier, people are pushed to spend their money for goods. This spending is exactly what drives up the aggregate demand. The policy is relevant to this point. But economics can show that it is *not*

necessary. It may not be relevant and may be even counterproductive. Rothbard [14] provides some pieces of evidence, the whole process has all the properties of redistribution, it changes expectations about future and drives resources to alternative uses. We will show that the process can also inflate bubbles and lead to a later depression.

It is not a big conspiracy if we look at the other side of the carry tax to find out what is the purpose of this whole theory. First, there are some notable lines in papers proposing the carry tax. For example: "The carry tax would serve as a powerful deterrent to hoarding currency. Currency that was hoarded and "past due" would only be accepted at a discount sufficient to cover the arrears." [15]. Or this quotation can make the purpose clearer: "So incentives have to be created to induce private holders of currency to reveal their ownership of currency, come forward and pay any negative interest due. No government has, as yet, had the stomach for that." [2, 216]. There is *no* single line arguing that the carry tax is important for the escape from the liquidity trap.

But we can raise an objection to this conclusion. It is possible that these authors see the escaping purpose as implicit and thus do not mention it. Since we find this objection relevant, we have to take into account *both* possible purposes.

## THE TRANSMISSION TO THE HOUSING MARKET

In this paper, we argue that the most important consequence of the negative interest rates can be seen in the housing market. To understand the link between the rates and housing prices we have to follow the money from the initial setting of the rates by a central bank to final housing purchases.

In the current system money is created in commercial banks through loans. Then these new loans can be and mostly are spent in different sectors for goods and services and thus increase demands for these goods and services. Increased demands lead to higher prices, especially of goods with inelastic supply. Inelastic supply can be expected in goods limited in quantity or produced on markets with high costs to entry or exit.

The role of a central bank is crucial in this mechanism. Central banks provide liquidity to commercial banks and increase their motivation to earn money by provision of cheaper loans and thus creating new money. To provide the liquidity, central banks can buy foreign currencies or other assets from commercial banks, decrease their regulatory limits or decrease central bank's interest rates.

All these policies are targeted to incentivize commercial banks to loan-making and with people spending this money to increase inflation to the targeted level. The most important result is uneven distribution of this increase in general level of prices. Some goods and services are not represented in CPI even though these policies increase demands for them. Typical example is demand for financial assets such as bonds or stocks. They are not included in CPI and if they would be, official inflation rate would be arguably higher.

Central banks thus increase prices of goods and services directly through their outright purchases or indirectly through the transmission mechanism.

Arguably, in the case of transmission mechanism there are markets where the new money is spent earlier and those where the increase in demand is seen relatively later. Because there was more than 7 trillion EUR in outstanding lending in 2016 at the European mortgage market we would expect this additional demand to press on higher housing prices. These are shown in *Fig. 3* below, represented by house price indices.

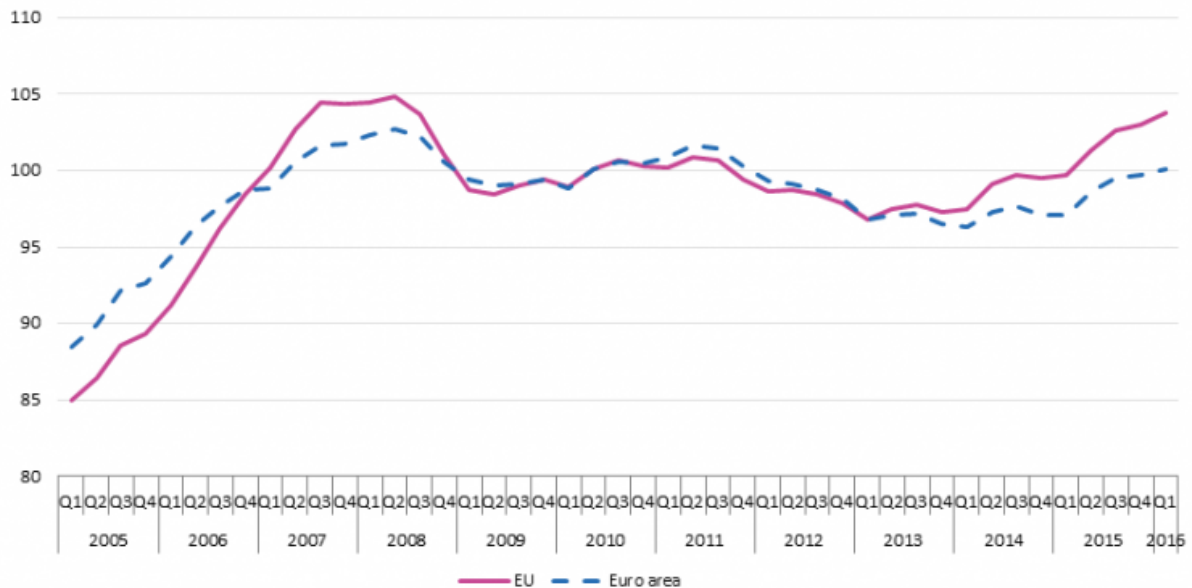


Figure 3 - House price indices - euro area and EU aggregates; index levels (2010 = 100) [16]

We see that low interest rates clearly led to higher housing prices before the crises. In 2008 crisis reverted the trend and prices went to 2006 level. The prices started to rise again in 2013 but went up only by about 3% per year. Compared to the average 5% growth in money supply (M3) we can be tempted to conclude that housing is less than proportionally represented in the new demand created with this money.

First objection to such claim has to be a possible effect of a change in housing supply. According to Hypostat [17] there is no significant change in housing supply: "Housing supply (as measured by the number of building permits issued, housing projects begun and housing projects completed) has remained more or less static since 2009, with building permits showing timid signs of increase during the last two years."

If this is so, then with stable supply and accelerating increase in demand the price of housing should increase proportionally to an increase in new mortgages. This is not seen.

However, the smaller increase in housing prices can be then explained with expectations and speculation. We argue, that the demand for housing itself is lower and is increased with speculative demand based on expectations of future increase in prices.

The effect of negative interest rates to the housing market is then the same as any other decrease in interest rates. Commercial banks are incentivized to provide more mortgages and increase demand for housing, partly because of speculative reasons. Moreover, stocks, bonds and other assets not represented or underrepresented in CPI will become more expensive but without increasing inflation rate.

**CONCLUSION**

Negative interest rates are discussed as a possible savior tool for central banks in their



effort to increase inflation in liquidity trap. With low growth and low inflation or even deflation central banks standardly decrease their interest rates. It was thought that the zero lower bound is binding but solutions how to go below zero were already presented. In today's world, it is possible to expect negative interest rates not only between central and commercial banks but also between commercial banks and firms or individuals. The goal is to motivate people to take and banks to grant more loans, especially mortgages.

But an effect of this new and alternative policy on inflation is limited. First, because it requires decrease in interest rates of commercial banks whose space to do that is limited by an alternative in holding cash. Proposals which make holding cash harder or more expensive were already presented. A possibility of a complete abolition of cash was also discussed in previous years.

Second step to overcome in the transmission mechanism can be insufficient demand for mortgages from the people. It is hard to push people to take more and higher mortgages if they do not demand more housing or more expensive housing. Thus, the demand is artificially increased through speculative demand of people who invest in increasing prices of housing in times of low interest rates. With negative interest rates, even stable prices of housing turn mortgages into profitable investment. There is a gap in empirical evidence for this claim but we have presented a limited evidence that this may be the case in EU.

We have to add to that a possibility of a housing bubble already exists. Based on the knowledge of the transmission mechanism we can argue that housing prices in 2008 would fall much lower than they did with the help of central banks. This shadow price of housing without added speculative demand can be lower and there can be significant gap between today's prices and the shadow price. Thus, a housing bubble can be present even when the prices are stable.

Policy makers, investors and lenders should be aware of this possibility and especially on the housing market where next to financial consequences defaulted mortgages create also well-known social problems.

## REFERENCES

- [1] **Buiter, W. and Panigirtzoglou, N. 2003.** Overcoming the Zero Bound on Nominal Interest Rates with Negative Interest on Currency: Gesell's Solution. *Economic Journal*. Volume 113, Issue 490, pp. 723-746.
- [2] **Buiter, W. 2009.** Negative Nominal Interest Rates; three ways to overcome the zero lower bound. *The North American Journal of Economics and Finance*. Volume 20, Issue 3, pp. 213-238.
- [3] Krugman, P. 2009. *Stay the Course*. June 15, 2009, New York Times.
- [4] **Keynes, J. M. 1936.** *The General Theory of Employment, Interest*. London : Macmillan.
- [5] **Krugman, Paul. 1998.** It's Baaack: Japan's Slump and the Return of the Liquidity Trap. *Brookings Papers on Economic Activity*. Volume 1998, Number 2, pp. 137-205.
- [6] **Svensson, L. E. O. 2003.** Escaping from a Liquidity Trap and Deflation: The Foolproof Way and Others. *Journal of Economic Perspectives*. Volume 17, Number 4, pp. 145-166.
- [7] **Rudebusch, G. D. 2009.** The Fed's Monetary Policy Response to the Current Crisis. *FRBSF Economic Letter*.
- [8] **Gesell, S. 1958.** *The Natural Economic Order*. London : Peter Owen Ltd.
- [9] **Block, W. 1978.** The Negative Interest Rate: Toward a Taxonomic Critique. *Journal of Libertarian Studies*. Volume 2, Number2, pp. 121-124.
- [10] **von Mises, L. 1944** *Bureaucracy*. s.l. : Yale University Press, 1944.
- [11] **Parkinson, C. N. 1958.** *Parkinson's Law: The Pursuit of Progress*. London : John Murray.

- [12] **Buchanan, J. 1975.** *The Limits of Liberty*. Chicago : The University of Chicago.
- [13] **Krugman, P. 1998.** *Optimal Fiscal Policy in a Liquidity Trap*. December 29, 1998, Memo.
- [14] **Rothbard, M. N. 1993.** *Man, Economy and State - A Treatise on Economic Principles*. s.l. : Ludwig von Mises Institute.
- [15] **Goodfriend, M.** Overcoming the Zero Bound on Interest Rate Policy. *Journal of Money, Credit and Banking*. 2000, Volume 32, Number 4, pp. 1007-1035.
- [16] **Eurostat. 2016.** House price index. *Eurostat*. [Online] 12 7 2016. [Cited: 1 9 2016.] [http://appsso.eurostat.ec.europa.eu/nui/show.do?dataset=prc\\_hpi\\_q&lang=en](http://appsso.eurostat.ec.europa.eu/nui/show.do?dataset=prc_hpi_q&lang=en).
- [17] **Hypostat. 2016.** Hypostat. *Hypo.org*. [Online] 7 9 2016. [Cited: 10 9 2016.] <http://www.hypo.org/Content/Default.asp?PageID=524>.

---

## COMPARISON OF PROPAGATION CHARACTERISTICS OF EXCITED STRESS WAVES IN PILE AND ANCHORAGE WITH BOLT SYSTEMS

Sheng Zeng<sup>1</sup>, Jing Zhang<sup>1</sup> and Bing Sun<sup>2</sup>

1 University of South China, Nuclear Resources Engineering College, NO28, West Changsheng Road, China; [usczengs@126.com](mailto:usczengs@126.com); [zjaimme@foxmail.com](mailto:zjaimme@foxmail.com)

2 University of South China, Institute of Urban Construction, NO28, West Changsheng Road, China; [sunbingnh@126.com](mailto:sunbingnh@126.com)

### ABSTRACT

Dynamic testing methods for pile systems and anchorage-with-bolt systems are similar and often confused with each other, possibly resulting in incorrect assessment of the quality of the pile and the anchorage systems. The stress wave velocity is one of the most important parameters for evaluating the quality of dynamic tests. In this paper, the stress wave velocities in standard concrete specimens of the free rock bolt and the different ages were a reference for comparing the stress wave velocities in a pile-and-anchor system. The tests were conducted using the low strain reflected wave method. Results indicate that the wave velocity in a pile is larger than that in the standard samples, and that the wave velocity in an anchorage-with-bolt system is smaller than that in a free steel bar, but larger than that in a pile and in standard samples. Wave velocities in the pile and in the standard samples were found to raise as the ages of samples increased. The wave velocity in the anchorage-with-bolt system initially decreased as specimen age increased, but increased with increasing specimen age afterward.

### KEYWORDS

Low strain reflected wave method, stress wave velocity, pile, anchorage with bolt system

### INTRODUCTION

A pile is the first or sometimes only choice of foundation support for many buildings, while an anchor is generally used to stabilize rock structures. Since both supports are hidden underground structures, it is very challenging to test accurately the quality of the pile and anchorage systems [1, 2]. The reflection wave method is very economical, rapid, simple and highly accurate, so it is most widely used in foundation pile integrity detection and it is the most representative of a dynamic measuring method [3]. Drawing on the principle of pile dynamic testing, use of the reflection wave method to detect the quality of anchor bolts is an effective way to solve the problem of real-time and rapid nondestructive testing of the anchorage quality of anchor bolts [4, 5]. However, care must be taken to address the dynamic testing results for an anchorage system because confusion and misjudgment can be induced if an inappropriate dynamic testing method is used. There is a significant and obvious difference between a pile and an anchorage system, such as the types of loading and defects, physical properties, and so on.

Many investigations have been performed to study the dynamic testing mechanism of both pile and anchorage systems. For instance, boltometer-instrument for nondestructive testing of grouted rock bolts was conducted [6], the stress reflected wave method was used to non-destructively test the bonding integrity of grouted bolts system [7, 8, 9], and high frequency stress wave was used to test grouted density of bolts [10]. Recently, guided ultrasonic wave was applied as a new type of non-destructive detection technique to detect the rock bolts [11, 12, 13]. Numerical simulation of low strain dynamic tests on attenuation and group velocity of guided ultrasonic wave was used to study the non-destructive testing of grouted rock bolts [14, 15, 16]. Researchers have put great efforts on studying stress wave non-destructive testing of anchorage quality for an anchorage system. However, the technology can not be effectively and accurately used to evaluate anchorage quality for bolt systems because the propagation of elastic stress wave in anchorage system is affected by many factors. The consolidation wave velocity is a key parameter for reflecting this propagation and evaluating the anchorage quality [17]. However, consolidation wave velocity has not been studied enough. Consolidation wave velocity was used to test the anchorage quality for an anchorage system [18]. For piles, the PIT (Pile Integrity Test) low strain instrument was used to test pile integrity [19], and the characteristics of stress wave propagation in pile were studied [20, 21].

These studies show that the stress wave velocity is the key reference parameter for evaluation of construction quality using the reflected wave method. However, these studies are intended either for an anchorage system or for a pile system. As there are similarities between a pile and an anchorage system, a comparative study between them needs to be conducted. In this paper, comparisons between the pile and anchorage systems will be described in terms of the stress wave velocity in the standard concrete specimens of the free rock bolt and the different ages in the standard concrete specimens of piles of different ages and of free rock bolts of different ages.

## THE THEORETICAL CALCULATIONS OF STRESS WAVE VELOCITIES IN BOTH SYSTEMS

### Stress wave velocity in pile

It is assumed that the medium is a continuous, homogeneous and isotropic elastic material. In a rectangular coordinates  $\{x, y, z\}$ , if the material damping is neglected, then the propagation of stress wave in an infinite elastic body satisfies a 3-D wave equation,

$$\rho \frac{\partial^2 \varepsilon}{\partial t^2} - c_3^2 \left( \frac{\partial^2 \varepsilon}{\partial x^2} + \frac{\partial^2 \varepsilon}{\partial y^2} + \frac{\partial^2 \varepsilon}{\partial z^2} \right) = 0 \quad (1)$$

where  $t$  is the elapsed time,  $\varepsilon$  is the strain, and  $c_3$  is the stress wave velocity under 3-D condition which is related to the density  $\rho$ , elastic modulus  $E$  and Poisson's ratio  $\mu$  of medium, and can be written as

$$c_3 = \sqrt{\frac{E(1-\mu)}{\rho(1+\mu)(1-2\mu)}} \quad (2)$$

Considering the diameter of a pile is far less than its length, the stress wave in the pile can be simplified as 1-D stress wave. When the pile vibrates in the longitudinal direction, the cross section is assumed to be a still plane with an uniform distribution of stress. Based on the d'Alembert's principle and Hook's law, the wave equation for the pile can be further given as,

$$\frac{\partial^2 u}{\partial t^2} - c_1^2 \frac{\partial^2 u}{\partial x^2} = 0 \tag{3}$$

where  $c_1$  is the stress wave velocity under 1-D condition. By neglecting the lateral influence, the wave velocity is only related to  $\rho$  and  $E$ , and Eq. 2. can be simplified as

$$c_1 = \sqrt{\frac{E}{\rho}} \tag{4}$$

For low strain condition, the 1-D wave equation given above is adopted. In the pile system, the wave velocity in pile is actually equal to that in medium as  $\rho$  and  $E$  representing density and elastic modulus of medium. Whenever the depth of shallow defects is required, a 3-D description of the wave velocity in the pile must be made using Eq.2 [22]. This can be illustrated by a simple calculation example. If  $\mu = 0.2$ , then we have  $c_3 = 1.05c_1$ , suggesting that the wave velocity in pile is bigger than that in medium, and 1-D simplification may deteriorate the testing accuracy. In addition, Eq.2.and Eq.4.only take into account the influence of medium but neglect that of steel bars, thereby obtaining a smaller value of wave velocity than the real one in pile.

### Stress wave velocity in anchorage system

The dynamic testing of pile is concerned with the problem of pile defects, while it is a little relation with the surrounding media. So the wave velocity mainly refers to that in the pile medium. For the anchorage system, the dynamic testing is purposely used to determine the bonding effect between the bolt and surrounding medium, and consequently wave velocity on the interface between the bolt and the surrounding medium is of interest. If the bolt can be seen as a 1-D rod member, the wave velocity in anchorage system can be obtained as

$$c' = \sqrt{\frac{E'}{\rho'}} \tag{5}$$

where  $c'$  is the wave velocity in anchor system, and  $E'$  and  $\rho'$  are equivalent elastic modulus and density of the anchorage system.

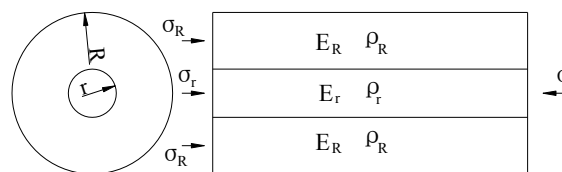


Figure 1 - Calculation model for anchorage systém

Figure 1 depicts a unit from the anchorage segment. Note that,  $r$ ,  $E_r$ , and  $\rho_r$ , are the radius, the elastic modulus and density of bolt, respectively; while  $R$ ,  $E_R$ , and  $\rho_r$ , stand for those of the anchorage system, correspondingly. It is assumed that both the bolt and anchorage medium are isotropic elastic, and that their longitudinal deformations are compatible.  $\sigma$  and  $\varepsilon$  are the stress acting on the unit body and corresponding strain, with the subscripts  $r$  and  $R$  denoting pile and anchorage systems, respectively. Based on the principle of mass conservation (Eq.6.), the

equilibrium condition of force (Eq.7.), the constitutive relation of materials (Eq.9.) and the condition of deformation compatibility (Eq.8.), as listed below:

$$\rho\pi R^2 = \rho_r\pi r^2 + \rho_R\pi(R^2 - r^2) \quad (6)$$

$$\sigma\pi R^2 = \sigma_r\pi r^2 + \sigma_R\pi(R^2 - r^2) \quad (7)$$

$$\varepsilon = \varepsilon_R = \varepsilon_r \quad (8)$$

$$\varepsilon = \frac{\sigma}{E}, \varepsilon_R = \frac{\sigma_R}{E_R}, \varepsilon_r = \frac{\sigma_r}{E_r} \quad (9)$$

the equivalent elastic modulus ( $E'$ ) and density ( $\rho'$ ) are obtained

$$E' = E_R \frac{R^2 - r^2}{R^2} + E_r \frac{r^2}{R^2} \quad (10)$$

$$\rho' = \rho_R \frac{R^2 - r^2}{R^2} + \rho_r \frac{r^2}{R^2} \quad (11)$$

substituting  $E'$  and  $\rho'$  back to Eq.5. leads to the wave velocity as

$$c' = \sqrt{\frac{E_R(R^2 - r^2) + E_r r^2}{\rho_R(R^2 - r^2) + \rho_r r^2}} \quad (12)$$

in extreme conditions, like for  $r \rightarrow 0$ ,  $c'$  is equal to the wave velocity in anchor medium, and for  $r \rightarrow R$ ,  $c'$  is then equal to the wave velocity in free steel bar.

## DETERMINATION OF WAVE VELOCITIES

### Test system

Based on the reflected wave method, the wave velocities in two (pile and anchorage) systems were obtained by a testing system including an AVANT-10 dynamic signal analysis system, an amplifier, two transducers and a computer. The wave velocities in the standard concrete test block were measured by using ZBL-U520 non-metal ultrasonic testing device.

### Measurement of wave velocities

In order to avoid effects of other factors on the wave velocities, tests for both pile and anchorage systems were carried out on the same laboratory model as shown in *Figure 2*. For pile, the force-hammer vertically acted on the medium close to the steel bar. For anchorage system, the force-hammer vertically acted on the steel bar. The reflection time was determined by the analysis of the time domain. If the travel time of reflection wave at the bottom of the pile is  $T_1$ , that at the bottom of the bolt is  $T_2$ , then these two respective wave velocities can be obtained,

$$c^p = \frac{2L}{T_1} \quad (13)$$

$$c^A = \frac{2L_2}{T_2 - 2L_1/V_b} \quad (14)$$

where  $c_P$  and  $c_A$  are the tested stress wave velocities in the pile and anchorage systems, respectively.  $L$ ,  $L_1$ , and  $L_2$  are the length of the pile, the free and grouted lengths of the bolt, respectively.  $V_b = 5100 \text{ m/s}$  is the wave velocity in the free bolt.

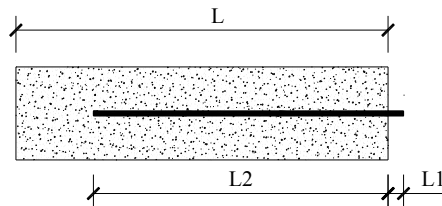


Figure 2 - Structure of member

### Laboratory test models

There were two test models constructed in a laboratory to study the stress wave velocity in both pile and anchorage systems, and their details are listed below. Model 1 (Figure 3) was cast into one standard concrete block with a dimension of  $600\text{mm} \times 600\text{mm} \times 2400\text{mm}$ , with the steel bars of 2.0 m in length and 28 mm in diameter embedded in the centre. The mixing proportion of water, cement, sand and gravel in the cubic concrete block was 1: 2: 4: 8. The grouted length of the steel bar in concrete was 1.9m, and the free length was 0.1m. The size of the standard cubic concrete specimens was  $150\text{mm} \times 150\text{mm} \times 150\text{mm}$ . Model 2 was built with mortar in a PVC pipe of 2.0m in length and 200mm in diameter, also with the same steel bar in the centre. The mix proportion of water, cement and sand in Model 2 is 1: 2: 4. The grouted and free lengths of the steel bars are the same as in the Model 1. The size of the standard cubic mortar specimens was  $70.7\text{mm} \times 70.7\text{mm} \times 70.7\text{mm}$ .



Figure 3 - Model in laboratory

### RESULTS AND DISCUSSIONS

Table 1 - Cube compressive strength of concrete and wave velocities related to Model 1 at various curing time

Curing time / d	Strength / Mpa	Anchorage system / m / s	Pile / m / s	Concrete / m / s
1	3.2	4864	2892	2891
3	11.7	4691	3070	2979
5	16.1	4578	3288	3072
7	17.9	4506	3357	3269
9	19.4	4343	3529	3339
11	23.1	4145	3582	3491
14	25.7	4099	3636	3518
21	27.3	4180	3692	3572
28	30.5	4193	3746	3686

Table 2 - Cube compressive strength of mortar and wave velocities related to Model 2 at various curing time

Curing time / d	Strength / Mpa	Anchorage system / m / s	Pile / m / s	Mortar / m / s
1	5.3			2215
3	7.9	4442	3113	2499
5	10.1		3171	2630
7	13.4	4422	3288	2778
9	15.6			3003
11	18.3			3066
14	19.2	4235	3390	3132
21	24.8	4285	3438	3269
28	26.3	4389	3518	3420

Tables 1 and 2 list the information about cube compressive strength of concrete and stress wave velocity related to the Model 1 and the Model 2, respectively, at different curing time intervals. The relationships between the cube compressive strength of the mediums, the curing time, and the stress wave velocity for both Model 1 and Model 2 are depicted in Figures 4 through 8 and Table 3. Discussions are provided below.

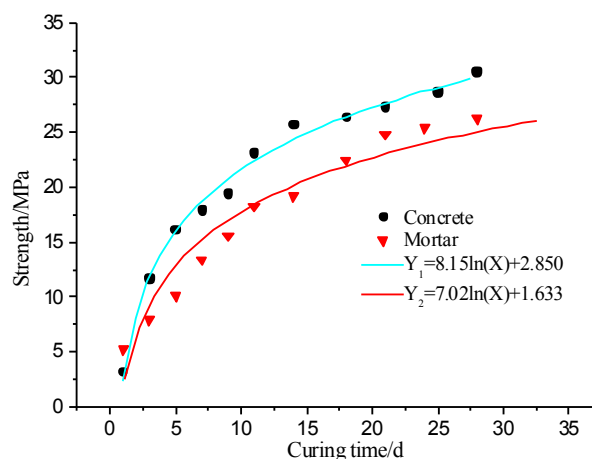


Figure 4 - Relationship between the cube compressive strength of medium and curing time

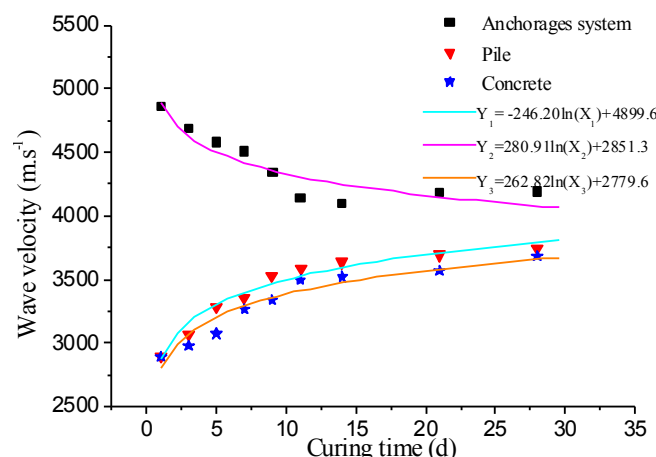


Figure 5 - Relationships between wave velocities of model 1 and curing time

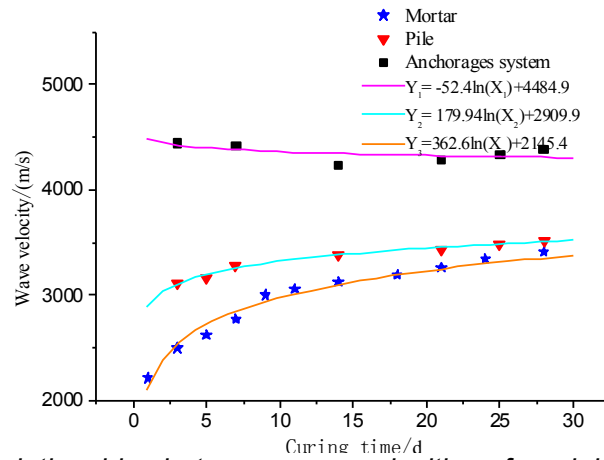


Figure 6 - Relationships between wave velocities of model 2 and curing time

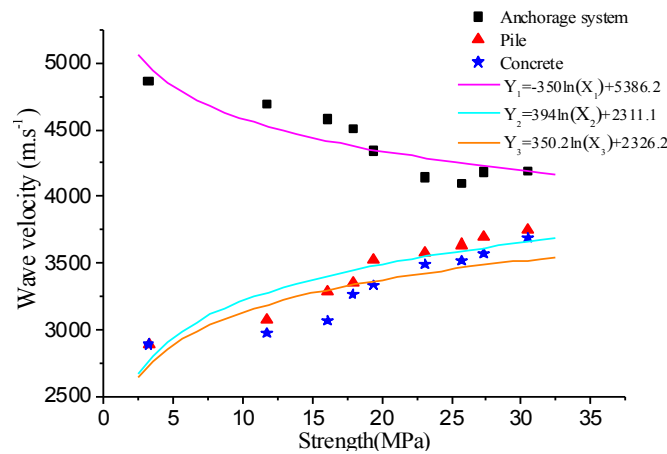


Figure 7 - Relationships between wave velocities of model 1 and cube compressive strength

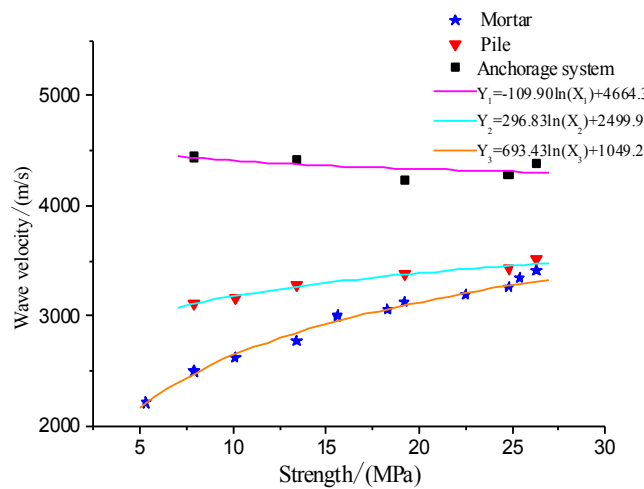


Figure 8 - Relationships between wave velocities of model 2 and cube compressive strength

Table 3 - Correlation coefficient of the fitting curve from Figures 4 to Figures 8

Figure	Fitting curve	Average	Variance	Coefficient
4	Y1	22.05	62.90	0.924
	Y2	18.44	48.22	0.922
5	Y1	3547.39	57523.06	0.921
	Y2	4289.52	44185.90	0.921
	Y3	3430.86	50352.89	0.921
6	Y1	4355.48	2160.05	0.914
	Y2	3354.33	25471.64	0.914
	Y3	3040.99	103432.50	0.914
7	Y1	4456.40	66814.47	0.942
	Y2	3352.63	83968.41	0.943
	Y3	3272.74	59375.54	0.949
8	Y1	4360.62	1883.41	0.985
	Y2	3320.10	13739.30	0.985
	Y3	2901.50	112519.40	0.977

(1) Characteristics of wave velocity in the anchorage system

In the early stage of curing process, the medium has a very low mechanical strength, and thus the reflection signal at the fixed end of the bolt is not obvious. The mortar medium does not closely envelop the bolt, resulting in low bond strength at the interface between the medium and the bolt. The wave velocity in an anchorage system is close to that in the free bolt during the early curing stage.

With the elapse of curing time, the strengths of both the medium and the bond at the concrete and bolt interface increase, the reflection signal at the fixed end gradually becomes stronger, and the travel time of reflection wave at the bottom of the bolt increases. It can be found that the wave velocity in anchorage system decreases with the curing time.

However, about 14 days later, the travel time of the reflection wave to the bottom of the bolt begins to decrease. The medium strength and bond strength are observed to slowly increase, indicating the gradual improvement in the anchorage quality. The wave velocity in the anchorage system steadily increases but lies between those measured in the free bolt and in the medium.

(2) Variation characteristics of wave velocity in pile

It can be seen that the wave velocity in the pile is the same as that in the medium of the pile, but different from that at the medium-bolt interface in the anchorage system and also different from that in standard specimen. As observed in figures, the evolution of wave velocity in the pile is similar to that in medium. The increases in the medium strength, and wave velocities in both pile and medium correspond to the curing time, but their variation magnitudes are greater during the first 14 days than subsequent 14 days.

(3) Comparison of wave velocities in the pile and anchorage systems

There are some similarities between the wave velocities in a pile system and in an anchorage system. The correlation coefficients between the wave velocities in both systems and curing time of samples are 0.914. Likewise, the correlation coefficients between wave velocities and cube compressive strength exceed 0.942, and the correlation coefficients between the cube compressive strengths of specimens and curing time exceed 0.922. Correlation coefficients that exceeded 0.8 were exhibited between the two variables. Thus, the wave velocities in a pile system

and in an anchorage system are very strongly correlated with curing time and cube compressive strength, whereas the cube compressive strengths of the surrounding medium in a pile system and an anchorage system have high correlations with curing time.

The previous analysis shows that the wave velocity in the pile system is mainly determined by the changing property of the medium, but also affected by the steel bar due to a 3-D effect mentioned before. However, the characteristics of wave velocity in the anchorage systems are quite different, which is controlled by the conditions of both the medium and the bond at the medium-bolt interface, or more concisely by the anchorage quality. The bigger the bond strength, the better the anchorage quality, and the closer the wave velocity in anchorage system to those in pile and medium. Contrarily, the smaller the bond strength, the worse the anchorage quality, and thus the closer the wave velocity in anchorage system to that in free steel bar.

## CONCLUSIONS AND DISCUSSIONS

In this paper, comparisons have been made on wave velocity in pile and anchorage systems. Different functional mechanisms have been identified and new equations for wave velocity have been proposed for pile and anchorage systems, respectively. The proposed method has been properly validated with laboratory experiments. Summary of the investigation on the propagation of wave velocity in pile and anchorage systems are given below:

(1) Wave velocity in a pile system is completely different from that in an anchorage system. In pile systems, wave velocity is closely related to the cube compressive strength and shows a rising trend as a function of curing time, and increasing amplitudes gradually stabilize as curing time increases. In anchorage systems, wave velocity is mainly dependent on the bond strength of the interface between the support medium and steel, decreasing in the early stage and then increasing afterwards. Wave velocity in anchorage systems is larger than that in both pile systems and the surrounding medium.

(2) Using the least square method to deal with the data, the regression equation and the fitting curve are got. The fitting curves are in line with the logarithmic function relationship. All the correlation coefficients of fitting curves reach more than 0.914.

(3) Using the least squares method to analyze data resulted in regression equations and fitting curves that described the test results. The fitting curves take the form of logarithmic functions. In practical work, the drawing datas of standard working curve are often used in a linear equation, and a linear equation can be reduced to a curve equation, which can be used to realize the curve fitting of the data.

## ACKNOWLEDGMENTS

The authors would like to acknowledge the support of the Scientific Research Fund of the National Natural Science Foundation of China (NO.51204098), the Natural Science Foundation of Hunan Province of China (NO.11JJ6045), and the Research and Development Plan of Hunan Province of China (NO. 2015SK2058-4).

## REFERENCES

- [1] Ivorra S, Garcia-Barba J, Mateo M et al., 2013. Partial collapse of a ventilated stone façade: Diagnosis and analysis of the anchorage system. *Engineering Failure Analysis* 31, 290-301.
- [2] Fang Z, Zhang KY and Tu B., 2013. Experimental investigation of a bond-type anchorage system for multiple FRP tendons. *Engineering Structures* 57, 364-373.
- [3] Xue DC, Wu Y and Zhang K., 2013. Experimental study and application on non-destructive testing

- of bolt axial force in coal mine. *Journal of Mining & Safety Engineering* 30(3): 375-379.
- [4] Wang C, Xu J and Yu X., 2013. The numerical simulation of the best stimulate wave on the end anchorage quality test. *Journal of Beijing institute of technology* 33(5): 454-458.
- [5] Thurner HF., 1988. Boltometer-instrument for nondestructive testing of grouted rock bolts; 2nd international symposium on filed measurements in geomchanics. Balkema, Rotterdam.
- [6] Wu R, Xu JH and Li C., 2012. Stress wave propagation in supporting bolts: A test for bolt support quality. *International Journal of Rock Mechanics and Mining Sciences* 22, 567-571.
- [7] Zhang SP, Zhang CS and Bai YL., 2011. Research on Method for Detecting Integrity of Grouted Rock Bolts. *Rock and Soil Mechanics* 32(11): 3368 -3372.
- [8] Deng DP, Li L and Zhao LH., 2015. Numerical Study on Dynamic Testing of Anchorage Quality of Rock Bolt (Cable) by Stress Wave Method 32(01): 62 – 69.
- [9] Z Zhou Y, Li Z and Liang GQ., 2012. Nondestructive technique for qualities of roofbolts and anchors in tunnel. *Nondestructive Testing* 34(12): 69-72.
- [10] Madenga V, Zou DH and Zhang C., 2006. Effects of curing time and frequency on ultrasonic wave velocity in grouted rock bolts. *Journal of Applied Geophysics* 59, 79-86.
- [11] Li DS, Ruan T and Yuan JH., 2012. Inspection of reinforced concrete delaminating using ultrasonic guided wave nondestructive test technique. *Science China-Technological Sciences* 55(10): 2893-2901.
- [12] Cui Y and Zou DH., 2012. Assessing the effects of insufficient rebar and missing grout in grouted rock bolts using guided ultrasonic waves. *Journal of Applied Geophysics* 79, 64-70.
- [13] He W, Wang C and Ning JG., 2009. Guided wave determination method of service load in partially grouted bolt. *Chinese Journal of Geotechnical Engineering* 28: 1767–1772.
- [14] Xu M and Zhang YX., 2003. Numerical study of low strain dynamic test for bolt. *Chinese Journal of Geotechnical and Engineering* 9, 1538-1541.
- [15] Zou DH, Cheng LL, Yue RJ et al., 2010. Grout quality and its impact on guided ultrasonic waves in grouted rock bolts. *Journal of Applied Geophysics* 72(2):102-106.
- [16] Zhang CS, Zou DH and Madenga V., 2006. Numerical simulation of wave propagation in grouted rock bolts and the effects of mesh density and wave frequency. *International Journal of Rock Mechanics and Mining Sciences* 43, 634-639.
- [17] Chen Y., 2014. Experimental study and stress analysis of rock bolt anchorage performance. *Journal of Rock Mechanics and Geotechnical Engineering* 6(5): 428-437.
- [18] Cheng JL, Sun XY, Feng L et al., 2012. Experimental study on non-destructive testing of rock bolts based on pseudo-random signal. *Safety Science* 50(4): 783-786.
- [19] Likins GE and Rausche F., 2000. Recent advances and proper use of PDI low strain pile integrity testing. In *Proceedings of Sixth International Conference on the Application of Stress-wave Theory to Piles*. St. Paulo, Brazil: 11-218.
- [20] Jing J, Dong JL, Zhi TL et al., 2014. A study on low strain integrity testing of platform-pile system using staggered grid finite difference method. *Soil Dynamics and Earthquake Engineering* 67, 345-352.
- [21] Xin XK, Wu MZ and Xie YT., 2005. Research on characteristics of wave propagation in pile enclosed by soils. *Chinese Journal of Geotechnical and Engineering* 24 (14): 2531-2536.
- [22] Chow YK, Phoon KK, Chow WF et al., 2003. Low strain integrity testing of pile three dimensional effects. *Journal of Geotechnical and Geoenvironmental Engineering* 129(11):1057-1062.

## GEOTECHNICAL PROPERTIES OF LATERITIC SOIL STABILIZED WITH THE ASHES OF OIL PALM FRONDS

*Emeka Nnochiri<sup>1</sup> and Olufikayo Aderinlewo<sup>2</sup>*

1 *Federal University of Technology, School of Engineering and Engineering Technology, Department of Civil and Environmental Engineering, Akure, P.M.B. 704, Nigeria; segunemeka@yahoo.com*

2 *Federal University of Technology, School of Engineering and Engineering Technology, Department of Civil and Environmental Engineering, Akure, P.M.B. 704, Nigeria; oluade2010@gmail.com*

### ABSTRACT

This study assesses the geotechnical properties of lateritic soil stabilized with the ashes of oil palm fronds. These properties are then compared with those of the same soil stabilized with cement to determine how well the ashes perform since cement is considered to be the best stabilizer. Laboratory tests such as specific gravity, moisture content, Atterberg limits, particle size distribution, compaction, unconfined compressive strength (UCS) and California bearing ratio (CBR) tests were first carried out to determine the basic properties of the lateritic soil (without the stabilizers). Based on the results of these tests, the soil was classified according to AASHTO soil classification system as an A-7-5 soil which is a poor soil. Hence, the need for stabilization. Thereafter, strength tests such as California bearing ratio (CBR), unconfined compressive strength (UCS) and compaction tests were performed on the soil to which the ashes and cement were added in percentages of 2, 4, 6, 8 and 10 by weight of the lateritic soil. The compaction test showed that the highest maximum dry densities (MDD) were recorded in the case of the oil palm frond ash (OPFA) and cement at 4% (MDD = 2.02kg/m<sup>3</sup>) and 6% (MDD = 2.40kg/m<sup>3</sup>) respectively. The highest CBR values obtained were 32.6% and 87.32% at 4% OPFA content and 6% cement content respectively. The unconfined compressive strengths (UCS) of the soil were highest at 4% OPFA content (234.86kN/m<sup>2</sup>) and 6% cement content (588.32kN/m<sup>2</sup>). The chemical tests performed on the OPFA and the cement showed that the highest oxide component were SiO<sub>2</sub> (33.67%) and CaO (60.83%) respectively.

### KEYWORDS

Geotechnical, stabilized, Atterberg limits, California bearing ratio, unconfine compressive strength, compaction.

### INTRODUCTION

Laterites are soil types rich in iron and aluminum that are formed in tropical areas. Most laterites are rusty-red because of the presence of iron oxides. They develop by intensive and long-lasting weathering of the underlying parent rock. Tropical weathering (laterization) is a prolonged process of chemical weathering which produces a wide variety in the thickness, grade, chemistry

and ore mineralogy of the resulting soils. The initial products of weathering are essentially kaolinized rocks called saprolites [1]. Lateritic soils are products of tropical weathering with red, reddish-brown or dark brown colour, with or without nodules or concretions and generally (but not exclusively) found below hardened ferruginous crusts [2]. Laterite formation factors include climate (precipitation, leaching, capillary rise and temperature), topography (drainage), vegetation, parent rock (iron rich rocks) and time of these primary factors. However, climate is considered to be the most important factor.

Soil stabilization aims at improving soil strength, controlling dust and increasing resistance to softening by water through bonding of the soil particles together thereby water proofing the particles or a combination of the two [3, 4]. The simplest stabilization processes are compaction and drainage (if water drains out of wet soil, it becomes stronger). The other process is by improving the gradation of particle size and further improvement can be achieved by adding binders to weak soils [5].

Soil stabilization can be accomplished by several methods, all these methods fall into two broad categories namely mechanical and chemical stabilization. Mechanical Stabilization is a physical process that involves altering the physical nature of native soil particles by either induced vibrations or compaction or by incorporating other physical properties such as barriers and nailing. Chemical Stabilization involves initiating chemical reactions between stabilizers (cementitious material) and soil minerals (pozzolanic materials) to achieve the desired effect of improving the chief properties of a soil that are of interest to engineers namely volume stability, strength, compressibility, permeability and durability [3, 6, 7].

### **Alternatives to Cement**

About 7% of CO<sub>2</sub> is released into the atmosphere during the cement production [8]. This has negative effects on the ecology and future of human beings one of which is global warming. Research on alternatives to cement has so far centred on the partial replacement of cement with different materials. In advanced countries, partial replacement of cement with pozzolans is well documented.

Reasons for finding alternatives to cement include the following: high cost of production, high energy demand and emission of CO<sub>2</sub> (responsible for global warming). In the third world countries, the most common and readily available materials that can partially replace cement without economic implication are bio-based materials and agro-based wastes; notable ones are Achahwok ash, Bambara groundnut shell ash, bone ash, groundnut husk ash, rice husk ash and wood ash, dried banana leaves, bagass, bamboo leaves, some timber species and periwinkle shell ash [8].

### **Need to Stabilize Laterites**

Lateritic soils are generally used for road construction in Nigeria. Lateritic soils in its natural state generally have low bearing capacity and low strength due to high clay content. The strength and stability of lateritic soil containing large amounts of clay cannot be guaranteed under load in the presence of moisture [9]. The use of lateritic soils consisting of high plastic clay content results in cracks in and damage to pavement, roadways, foundations or any civil engineering construction.

The need to improve the strength and durability of lateritic soil in recent times has become imperative, this has geared researchers towards using stabilizing materials that can be sourced

locally at a very low cost [10]. These local materials can be classified as either agricultural or industrial wastes [11]. In cases where sourcing for durable soil may prove economically unwise, the viable option is to stabilize the available soil to meet the specified requirements of construction [12, 13].

### Cement Stabilization

The addition of cement to a material, in the presence of moisture, produces hydrated calcium aluminate and silicate gels, which crystallize and bond the material particles together. Most of the strength of a cement-stabilized material comes from the physical strength of the matrix of hydrated cement. A chemical reaction also takes place between the material and lime which is released as the cement hydrates, leading to increased soil strength. The solubilities of Silica and Alumina are greatly increased in the stabilised clay soils to form calcium silicate gel which coats and binds lumps of clay together and occupies the pores in the soil [14].

### MATERIALS AND METHODS

The materials used for this research work were lateritic soil, oil palm fronds ash and ordinary portland cement. The disturbed lateritic soil samples were collected from within the campus of the Federal University of Technology, Akure (FUTA), Nigeria. The lateritic soil was collected at depths representative of the soil stratum and not less than 1.2m below the natural ground level. It was thereafter brought to the Geotechnical laboratory of the Federal University of Technology, Akure (FUTA) and marked, indicating the soil description, sampling depth and date of sampling. The lateritic soil was air-dried for two weeks to allow for partial elimination of natural water which may affect the analysis, then sieved with sieve no 4(4.75mm opening) to obtain the final soil samples for the tests. After the drying period, lumps in the samples were pulverised under minimal pressure.

Fresh oil palm fronds were obtained from a large abandoned farmland at the phase II site of the Federal University, Oye-Ekiti. The broom-stick part of the fronds were removed, the fronds were spread on the ground and air-dried to facilitate easy burning. The fronds were burnt into ashes and collected in polythene bags, stored under room temperature until used. Furthermore, the ashes were sieved through BS Sieve 75 $\mu$ m and kept covered before and after use to prevent moisture and contaminations from other materials. Figure 1 shows a sample of the oil palm frond ash.



Figure 1 - Sample of the oil palm frond ash

The following tests namely particle size distribution, Atterberg limit, British Standard (BS) compaction, unconfined compressive strength (UCS) and California bearing ratio (CBR) tests were carried out on the unstabilised samples to obtain its basic properties. Thereafter, compaction, unconfined compressive strength and California Bearing Ratio (CBR) tests were carried out on the stabilized samples in accordance with British Standard Methods of testing soil for Civil Engineering purposes [15, 16]. In addition, the chemical composition of the ordinary portland cement and the ashes of the oil palm fronds were determined through chemical analysis. Chemical analysis of the fine powdered ashes and cement was carried out at the central laboratory of the Federal University of Technology, Akure using the x-ray diffraction and SEM techniques.

## DISCUSSION OF RESULTS

### *Chemical Analysis of the OPFA and OPC*

The chemical analysis carried out on the oil palm frond ash (OPFA) and ordinary Portland cement revealed the oxide components as shown in *Table 1*.

*Table 1 - Chemical composition of the oil palm frond ashes (OPFA) and ordinary Portland Cement (OPC)*

Components (oxides)	OPFA (%)	OPC (%)
CaO	28.66	60.83
ZnO	0.89	NIL
MgO	3.97	3.02
P <sub>2</sub> O <sub>5</sub>	3.99	NIL
SiO <sub>3</sub>	5.59	NIL
Al <sub>2</sub> O <sub>3</sub>	14.79	6.47
Fe <sub>2</sub> O <sub>3</sub>	4.51	2.79
SiO <sub>2</sub>	33.67	20.05
K <sub>2</sub> O	3.41	0.51
Na <sub>2</sub> O	0.52	0.48
SO <sub>3</sub>	NIL	0.35
TiO <sub>2</sub>	NIL	0.38

*Table 1* shows that the OPC contains a high amount of CaO (60.83%) which aids in the stabilization process and invariably makes cement a very effective stabilizer. On the addition of water to cement, major cementitious products like calcium silicate hydrates and calcium aluminium hydrates are produced which provide the bond between the soil particles. On the other hand, the OPFA can be regarded as a pozzolana since it contains an appreciable amount of SiO<sub>2</sub> (20.05%). A pozzolana is a siliceous material which by itself does not possess cementitious properties but will in finely divided form and in the presence of water react with calcium hydroxide, Ca(OH)<sub>2</sub> to form

cementitious compounds [17]. The OPFA aptly qualifies as a pozzolana since the percentage sum of its SiO<sub>2</sub>, Al<sub>2</sub>O<sub>3</sub> and Fe<sub>2</sub>O<sub>3</sub> components (52.97%) exceeds the minimum requirement of 50% [18].

### Preliminary tests on the unstabilized soil sample

The tests carried out on the lateritic soil sample without the additives gave its natural moisture content as 13.4% and specific gravity as 2.40. The soil was classified as a silt-clay soil since the percentage passing the sieve no. 200 was than 35%. Based on its liquid limit of 45.5% and plasticity index 14.5%, the soil was further clasified as an A-7-5 “fair to poor soil” [19] which cannot be used in road construction without treatment. Hence, the need for stabilization. *Table 2* shows a summary of the properties of the natural lateritic soil used in this study. Compaction test on the soil gave a maximum dry density (MDD) of 1.94kg/m<sup>3</sup> with corresponding optimum moisture content (OMC) of 10.7%, while its California bearing ratio (CBR) and unconfine compressive strength (UCS) were 10.42% and 209.18kN/m<sup>2</sup> respectively.

*Table 2 - Properties of the natural lateritic soil*

Property	Value
Natural moisture content	13.4%
Specific gravity	2.40
Liquid limit	45.5%
Plastic limit	31.0%
Plasticity index	14.5%
AASHTO classification	A-7-5
Soil type	Silt-Clay
Maximum dry density (MDD)	1.94kg/m <sup>3</sup>
Optimum moisture content (OMC)	10.7%
California bearing ratio (CBR)	10.42%
unconfine compressive strength (UCS)	209.18kN/m <sup>2</sup>

### Compaction test on the lateritic soil containing the additives

*Table 3* shows the compaction properties of the soil containing the additives. In the case of the soil with OPFA, the MDD improved from the initial value of 1.94kg/m<sup>3</sup> for the natural soil to 1.98kg/m<sup>3</sup> at 2% OPFA content and this further increases to 2.02kg/m<sup>3</sup> (the highest value) when the OPFA content was increased to 4%. Thereafter, the MDD drops all through up to 10% OPFA content. This drop can be attributed to the fact that the specific gravity of the soil had been lowered on addition of the OPFA.

In the case of the lateritic soil containing the ordinary Portland cement (OPC), the MDD initially drops from the original value of 1.94 for the natural soil to 1.85 at 2% cement content after which it increases to 1.91 at 4% cement content (which is still lower than that of the natural soil).

The highest MDD (2.40) is reached at 6% cement content after which it drops at 8% and 10% cement contents.

*Table 3 - Compaction properties of the lateritic soil containing the additives*

Additives (%)	Soil with OPFA		Soil with OPC	
	MDD (kg/m <sup>3</sup> )	OMC (%)	MDD (kg/m <sup>3</sup> )	OMC (%)
2	1.98	11.3	1.85	18.6
4	2.02	11.2	1.91	17.3
6	1.99	13.4	2.40	15.7
8	1.87	14.15	1.96	17.9
10	1.86	16.60	2.30	19.1

### California bearing ratio (CBR) test on the lateritic soil containing the additives

Table 4 shows the unsoaked CBR of the soil containing the additives. In the case of the soil containing OPFA, the CBR increases from 10.42% for the natural soil to 31.06% at 2% OPFA content and to the highest value of 32.6% at 4% OPFA content. Thereafter, the CBR falls throughout up to 10% OPFA content.

In the case of the soil containing the OPC, the CBR increases from 10.42% for the natural soil to 57.62% at 2% OPC content, drops to 45.74% at 4% cement content, increases again to the highest value of 87.32% at 6% cement content, drops again to 78.32% at 8% cement content and finally increases to 80.41% at 10% cement content.

*Table 4 - CBR (unsoaked) of the lateritic soil containing the additives*

% of additives	unsoaked CBR (%) values	
	Soil with OPFA	Soil with OPC
2	31.06	57.62
4	32.6	45.74
6	21.19	87.32
8	19.29	78.32
10	9.52	80.41

Table 5 shows the soaked CBR of the soil containing the additives. In the case of the soil containing OPFA, the CBR increases from 10.42% for the natural soil to 15.41% at 2% OPFA content and to the highest value of 17.33% at 4% OPFA content. Thereafter, the CBR falls throughout up to 10% OPFA content.

In the case of the soil containing the OPC, the CBR increases from 10.42% for the natural soil to 42.63% at 2% OPC content, drops to 33.78% at 4% cement content, increases again to the

highest value of 74.62% at 6% cement content, drops again to 64.35% at 8% cement content and finally increases to 69.48% at 10% cement content.

*Table 5 - CBR (soaked) of the lateritic soil containing the additives*

% of additives	soaked CBR (%) values	
	Soil with OPFA	Soil with OPC
2	15.41	42.63
4	17.33	33.78
6	13.26	74.62
8	8.12	64.35
10	6.44	69.48

**Unconfined compressive strength (UCS) test on the lateritic soil containing the additives**

Table 6 shows the UCS of the soil containing the additives. In the case of the soil containing OPFA, the UCS increases from 209.18kN/m<sup>2</sup> for the natural soil to 226.73kN/m<sup>2</sup> at 2% OPFA content and further on to the highest value of 234.86kN/m<sup>2</sup> at 4% OPFA content. Thereafter, the UCS drops to 216.32kN/m<sup>2</sup> at 6% OPFA content, increases again to 227.85kN/m<sup>2</sup> at 8% OPFA content and finally drops to 198.44 at 10% OPFA content..

In the case of the soil containing the OPC, the UCS increases from 209.18kN/m<sup>2</sup> for the natural soil to 542.52kN/m<sup>2</sup> at 2% OPC content, drops to 430.86 kN/m<sup>2</sup> at 4% OPC content , increases again to 588.32kN/m<sup>2</sup> at 6% OPC content, drops again to 574.46kN/m<sup>2</sup> at 8% OPC content and finally increases to 575.22kN/m<sup>2</sup> at 10% OPC content.

*Table 6 - UCS of the lateritic soil containing the additives*

% of additives	Unconfirmed compressive strength (kN/m <sup>2</sup> )	
	Soil with OPFA	Soil with OPC
2%	226.73	542.52
4%	234.86	430.86
6%	216.32	588.32
8%	227.85	574.46
10%	198.44	575.22

## CONCLUSION

Based on the chemical test, the oil palm frond ash can be classified as a pozzolanic material because the percentage sum of its  $\text{SiO}_2$ ,  $\text{Al}_2\text{O}_3$  and  $\text{Fe}_2\text{O}_3$  components (52.97%) exceeds the minimum requirement of 50%.

The compaction, California bearing ratio (CBR) and unconfined compressive strength tests indicated that the highest values were obtained at 4% OPFA and at 6% OPC content. These represent the optimum values for the OPFA and OPC to be used as stabilizers in the lateritic soil.

It can be inferred from the tests that even though cement proved to be a better stabilizer, the OPFA could be used as an alternative if added in the right quantity. The oil palm fronds provide a readily available, easily sourced and affordable material that can be used to produce the OPFA stabilizer.

## REFERENCES

- [1] Dalvi A.D., Bacon W.G., Osborne R.C., 2004. The Past and the Future of Nickel Laterites. PDAC 2004 International Convention, Trade Show and Investors Exchange. Retrieved 2010.
- [2] Ola S.A. Geotechnical Properties and Behaviour of some Nigerian Lateritic Soils. In: Tropical Soils of Nigeria in Engineering Practice. Rotterdam: A. A. Balkema;1978, p. 61-84.
- [3] Sherwood P., 1993. Soil Stabilization with Cement and Lime. State of the Art Review. Transport Research Laboratory HMSO, London.
- [4] Amu O.O., Adetuberu A.A., 2010. Characteristics of Bamboo Leaf Ash Stabilization on Lateritic Soil in Highway Construction. International Journal of Engineering and Technology, vol. 2, no. 4: 212-219.
- [5] Rogers C.D.F., Glendinnings S., 1993. Modification of Clay Soils using Lime. In: Proceedings of the Seminar held at Loughborough University on Lime Stabilization, edited by C.A. Rogers, 99-114.
- [6] Ingles O.G., Metcalf J.B., 1972. Soil Stabilization: Principles and Practice. Sydney: Butterworths, p.374.
- [7] EuroSoilStab, 2002. Development of Design and Construction Methods to Stabilise Soft Organic Soils: Design Guide for Soft Soil Stabilization. European Commission, Industrial and Materials Technologies Programme CT97-0351.
- [8] Aribisala O.A., 1989. Sourcing of Local Raw materials and Investment Opportunity in Building/ Construction Industrial Sector. In: Proceedings of the National Workshop held at Central Hotel, Kano, 23 – 37.
- [9] Alhassan M., 2008. Potential of Rice Husk Ash for Soil Stabilization. AU Journal of Technology, vol. 71, no. 4: 246-250.
- [10] Bello A.A., Ige J.A., Hammed A., 2015. Stabilization of Lateritic Soil with Cassava Peels Ash. British Journal of Applied Science and Technology, vol. 7, no. 6: 642-650.
- [11] Amu O.O., Basiru N.T., Coker A.A., 2011. Effects of Forage Ash as Stabilizing Agent in Lateritic Soil For Road. Innovations in Science and Engineering, vol. 1: 1-8.
- [12] Mustapha M.A., 2005. Effect of Bagasse Ash on Cement Stabilized Laterites. Seminar Paper presented in the Department of Civil Engineering, Ahmadu Bello University, Zaria, Nigeria.
- [13] Osinubi K. J., 1999. Evaluation of Admixture Stabilization of Nigeria Black Cotton Soil. Nigerian Society of Engineers Technical Transaction, vol. 34, no. 3: 88-96.

- [14] Amu O.O., Faluyi S.O., 2005. Effects of Lime Stabilization and the pH values of Lateritic Soils in Ado-Ekiti, Nigeria. *Journal of Applied Sciences*, vol. 5: 192-194.
- [15] British Standard Institution, 1990. *Methods of Test for Soils for Civil Engineering Properties (BS 1377)*. London: British Standard Institution, p.143.
- [16] Head K.H., 1992. *Manual of Soil Laboratory Testing. Soil Specification and Compaction Tests*. 2<sup>nd</sup> Edition, vol. 1; London: Pentech Press.
- [17] Kadyali L.R., Lal N.B., 2008. *Principles and Practices of Highway Engineering*. 5th Edition; Delhi: Khanna Publishers.
- [18] Rochigo C.K., Kleber F.P., Mariana O.G.P., Marcelle M.B., 2013. Banana Leaves Ashes as Pozzolans for Concrete and Mortar of Portland Cement. *Construction and Building Materials*, vol. 54: 460- 465.
- [19] AASHTO, 1991. *Standard Specification for Classification of Soils and Soil-Aggregate Mixtures for Highway Construction Purposes*, AASHTO M 145.

# HISTORICAL PLASTER COMPOSITION DETECTION USING REFLECTANCE SPECTROSCOPY

*Eva Matoušková<sup>1</sup>, Martina Hůlková<sup>1</sup> and Jaroslav Šedina<sup>1</sup>*

*1 Czech Technical University in Prague, Faculty of Civil Engineering, Department of Geomatics, Thákurova 7, 166 29, Praha 6, Czech Republic; [eva.matouskova@fsv.cvut.cz](mailto:eva.matouskova@fsv.cvut.cz), [martina.hulkova@fsv.cvut.cz](mailto:martina.hulkova@fsv.cvut.cz), [jaroslav.sedina@fsv.cvut.cz](mailto:jaroslav.sedina@fsv.cvut.cz)*

## ABSTRACT

Reflectance spectroscopy is a non-invasive method that is based on the fact that a specific object/material provides various reflectances in different wavelengths across the spectral range. It can provide unique information regarding the material composition of the object of interest and has been used in many fields in recent years. Determining composition of historical plaster is very important when defining its individual components and possibly place of origin or even its age. This information can be a key issue for its future repairs that are desired to be done as similar to the original method as possible.

For a precise reflectance spectroscopy material detection, a fine spectral library is needed. Special mathematical methods are used for comparison of measured spectral curve with individual spectral curves stored in the used spectral library. The spectral analysis then shows similarity of the measured curve with the reference ones.

This paper introduces results of the new plaster composition spectral library created by Department of Geomatics, Faculty of Civil Engineering, Czech Technical University in Prague within the Czech Ministry of Culture Project (DF13P01OVV002). This spectral library has been tested on two historical plaster samples.

## KEYWORDS

Reflectance spectroscopy, plaster, composition detection, spectral library, QSdata software

## INTRODUCTION

Reflectance spectroscopy has been an area of active research and development in many different fields during past decades and its giant potential is becoming more visible with technical development. It provides full reflectance information from across the electromagnetic spectrum in given spectral range. This is done by collecting many (tens to hundreds) narrow, closely spaced spectral bands so that the resulting spectra appear to be continuous curves. Using these data, one can enable the extraction of reflectance spectra that can be directly compared with similar spectra measured in the field or in a laboratory. The number of measured spectral bands is sensor dependent and is not the key issue. It is rather the narrowness and contiguous nature of the measurements.

The percentage of the light hitting a material that is then reflected by that material is called the spectral reflectance. For most materials it varies within wavelength because of different absorption and scattering characteristics over the spectral range. These variations are shown in plots called spectral curves or reflectance spectrums, where wavelength is shown on x-axis and the reflectance on y-axis (see *Figure 1*). Some materials will reflect certain wavelengths of light, while other materials will absorb the same wavelength. These patterns of reflectance and absorption across wavelengths can uniquely identify certain materials.

Specific materials have their spectral curves defined earlier in laboratory and they are stored in spectral libraries. Using these differences and comparison with laboratory measurements one can compare spectral curves in order to detect measured material.

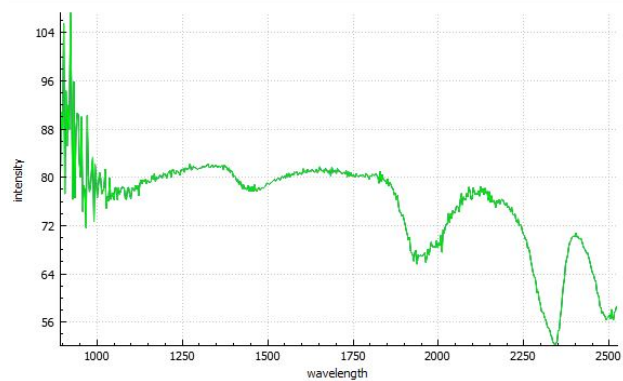


*Figure 1 – Example of spectral curve - limestone*

## INSTRUMENT

Reflectance spectrometers are devices that measure light which is emitted by or reflected from materials and its variation in energy with wavelength. One deals with sunlight or artificial illuminator that is diffusely reflected by measured materials. An optical dispersing element such as grating or prism in the spectrometer splits light into many narrow, adjacent wavelength bands and the energy in each band is measured by a separate detector. Using these detectors, the device can measure many spectral bands as narrow as hundreds of micrometres [1] over a wide wavelength range depending on the instrument.

An Ocean Optics NIRQuest2.5 512 modular spectrometer (*Figure 2*) is at disposal at the department of Geomatics, FCE, CTU in Prague and has been used in this study. It operates in 900 – 2500 nm spectral range where 512 bands are present and it is equipped with an InGaAs detector and cooling. Illumination is ensured by an external source Cool Red (*Figure 3*) that provides adequate light source in mentioned spectral range. An optic fibre then transfers the light into the scanning probe. Reflectance spectrometers give a spectral information about one single point of interest. Data is acquired by enclosing the end of the fibre optics to the object of interest. This device gains data from a single point in form of an ASCII file – wavelength and a corresponding count value.



Figure 2 - Spectrometer NIRQuest



Figure 3- Illumination source Cool Red

A spectroscopic measuring device (Figure 4) besides mentioned consists of a laptop with a control software, fibre optics and a measuring probe. The probe is composed of an optical fibre, that transfers information into the spectrometer as well as fibres bringing illumination from external source. End of the probe can be seen in Figure 5. A white reference material is a key issue for spectroscopic measurements. After several tests it was found that Spectralon from LabSphere [2], Figure 6 will be used as a white reference.

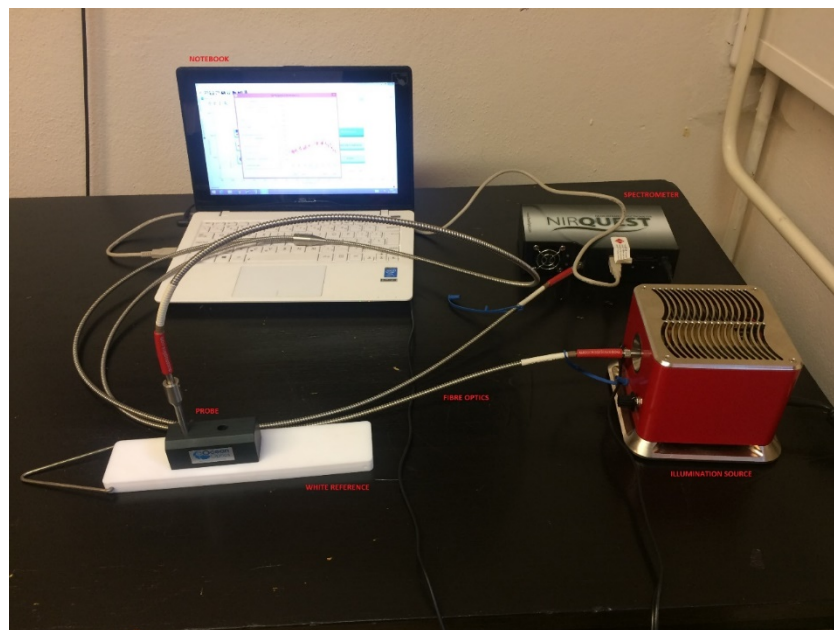


Figure 4 - Reflectance spectrometry measuring device



Figure 5 - Probe on the end of fibre optics



Figure 6 - White reference calibration (Spectralon)

## MATERIAL SPECTRAL LIBRARY

In order to analyse various historical samples a unique spectral library had to be created. This was performed in cooperation with Institute of Theoretical and Applied Mechanics, Academy of Science, Czech Republic that provided test samples of 20 most common materials used for plaster production. These samples were carefully prepared and a final set of twenty spectra was recorded. Namely: three different types of sandstone, quartzite, limestone, marlstone, brick, paving stone, five different types of mortar, geopolymer, quart sand, river sand, calcium hydrate, dolomite, gypsum and metakaolin. In order to create convenient etalons curves, many measurements had to be performed and the final spectral curve of each material is an average of 50 individual measurements. Spectral curves of five examples can be seen in *Figure 7*. In case of interest regarding this library, please contact an author via email [eva.matouskova@fsv.cvut.cz](mailto:eva.matouskova@fsv.cvut.cz).

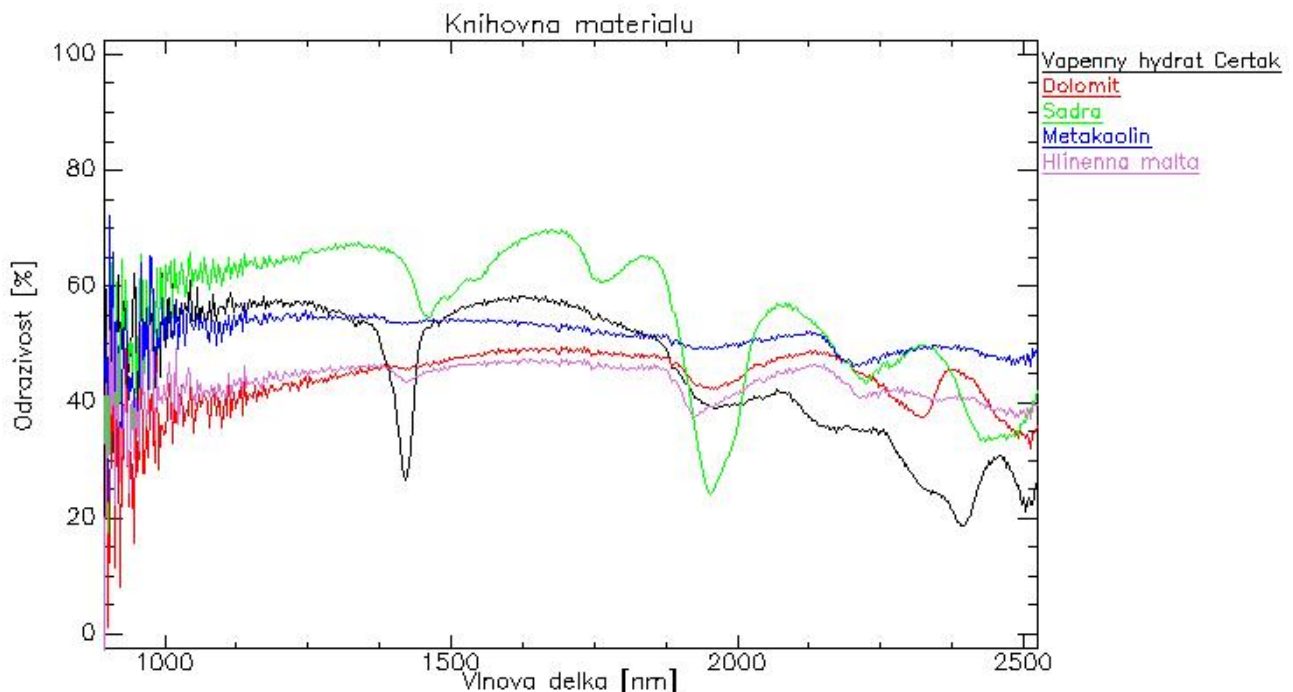


Figure 7 – Spectral curves included in the new library

## DATA PROCESSING

The first pre-processing step is the dark and white reference calibration. This can be done by the sensor itself (devices are equipped with a calibration workflow) or manually in processing software. The dark calibration is usually performed by the sensor operating software by subtracting the signal of the sensor (with closed optics) from the object signal. The general-purpose method for the white reference is to use an image processing software. A white reference material is recorded and then it is used as a 100% reflectance. The result will then be a reflectance ranging from 0 to 100% (100% is the reflectance of white reference). After the pre-processing the user can record the reflectance curve of samples of interest.

Final processing can be performed in any suitable software. The key issue is a composition determination that is very complex and provides information about the nature of specific pixel.

Absorption bands or peaks can be analysed in order to discover pixels attributes, other mathematical options can be used. One can mention Spectral Feature fitting that is based on least-squares method [3].

In this analysis a linear unmixing has been performed using the latest version of our spectroscopy analysis software QSdata (v0.9.5). This software has been developed at the Department of Geomatics, FCE, CTU in Prague under the Ministry of Culture Project (DF13P01OVV002) and can be downloaded free of charge from the project website <http://lfgm.fsv.cvut.cz/naki/vysledky.html>.

### SAMPLE ANALYSIS EXAMPLE

When a sample is recorded by the reflectance spectrometer an ASCII text file with wavelengths and corresponding values is stored. One must take into account the calibration procedure of a specific device. Mentioned file is then loaded into the QSdata software and analysis can be performed. Each sample has been measured at least five times and an average has been used in the analysis in order to provide more overall image of the sample of interest. Outlying measurements have been excluded from the average computation.

The final result is then given in the form of table where the most similar etalons are mentioned on the top. A linear combination of active etalons is calculated using non-negative least squares algorithm [3]. The similarity number shows the percentage of each material included in the sample. Samples with similarity number lower than 0,1 are not taken into account due to low similarity and expected calculation error. For more precise percentage determination repetition of the analysis has been performed. With the second analysis etalons with zero similarity have been excluded. The final percentage is then calculated by subtracting a previously defined value so that the final sum is equal to one.

Samples have been provided by the property owners in the Czech Republic. No historic object has been damaged while purchasing these samples, only those found on the ground have been used.



Figure 8 – First analysed sample



Figure 9 – Second analysed sample

The first tested sample (Figure 8) consists of 54% hydraulic lime mortar and 46% gypsum (Figure 10). Four repetitions of the analysis were performed to obtain this result. Figure 12 shows the result visualization. The second sample (Figure 9) has 49% of hydraulic lime mortar, 37% Božanov sandstone and small amount cca 4% quartzite (Figure 11), with three analysis repetitions. Visualization is shown in Figure 13.

Vzorek4.txt

Similarity	Etalon
0.5943	11-MalHydroVapno
0.5172	18-sadra

Figure 10 – Sample1 - QSdata unmixing outcome

Vzorek2-prumer.txt

Similarity	Etalon
0.6081	11-MalHydroVapno
0.6004	1-piskovec
0.1646	4-kremenec
0.0000	12-MalVapnoMetakaolin

Figure 11 - Sample 2 - QSdata unmixing outcome

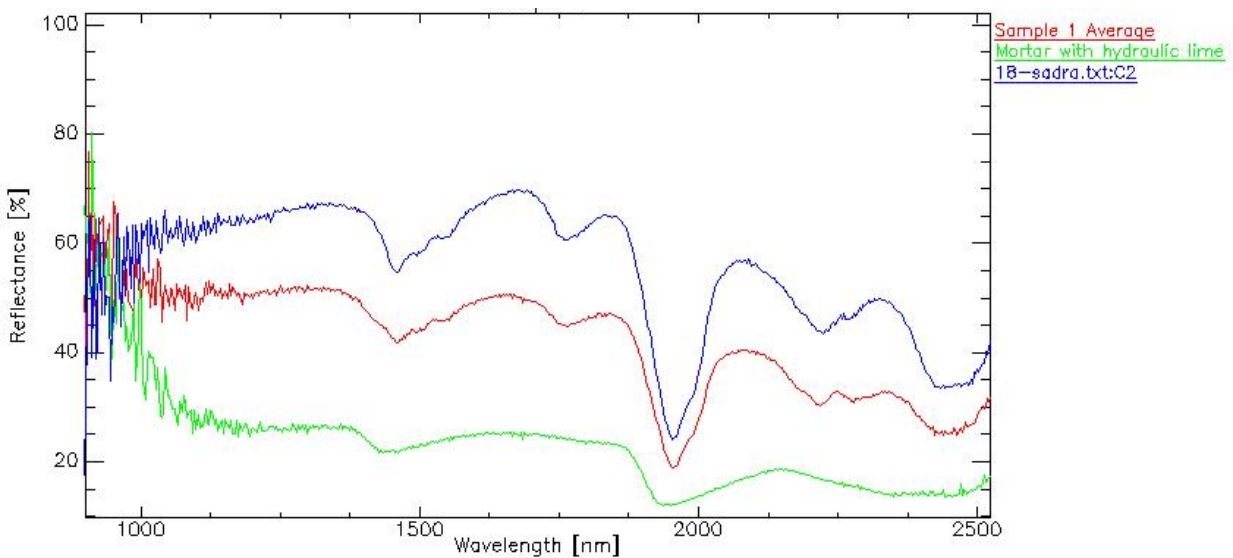


Figure 12 – Sample 1 visualization

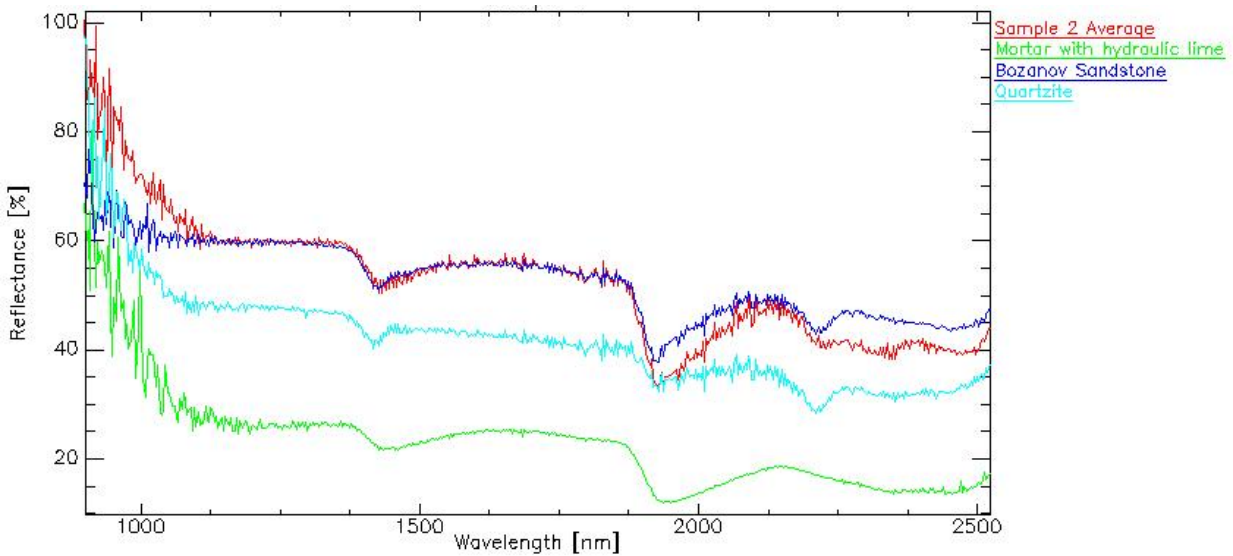


Figure 13 – Sample 2 visualization

## CONCLUSION

Reflectance spectroscopy has been tested to detect and analyse unknown plaster samples. The latest version (v0.9.5) of newly developed software QSdata has been tested and used for the analysis. Repetition of analysis with excluded low similarity number etalons from previous computations was tested. It was found, that this technique provides fine results, but the percentage of each component has to be recalculated at the end of the analysis. It is desired to include this workflow to the future version of the QSdata software.

Results show that reflectance spectroscopy can provide unique information for a plaster documentation and can help with a composition analysis of samples. Two historical plaster samples have been shown in this paper and their composition has been determined. Further research will be done in this matter to verify the sample material composition and the QS data software will be upgraded in order to visualize results and to provide more user-friendly employment.

The crucial issue of introduced workflow lies in the fact, that the reflectance spectroscopic device is fully mobile and thus can be moved to any location needed and ensures fine non-invasive analysis of the object of interest. The only limitation is the need of electrical power that can be provided by a generator of any kind.

## ACKNOWLEDGEMENT

This research has been created under the Czech Ministry of Culture Project "New methods of non-invasive cultural heritage documentation" (DF13P01OVV002). More information regarding this project can be found at the project website <http://ifgm.fsv.cvut.cz/naki/index.html>. Authors would like to thank prof. Ing. Aleš Čepek, CSc. for his time and support devoted to the creation of the QSdata software.

## REFERENCES

- [1] SMITH, Randal B. Introduction to hyperspectral imaging. In: *MicroImages* [online]. 2012 [cit. 2012-08-09]. Available from: <http://www.microimages.com/documentation/Tutorials/hyprspec.pdf>
- [2] Calibrated Diffuse Reflectance Targets. *LabSphere* [online]. [cit. 2015-11-25]. Dostupné z: <https://www.labsphere.com/products/reflectance-reference-standards-targets/reflectance-targets/calibrated-diffuse-reflectance-targets/>
- [3] Franc, Vojtěch; Hlaváč, Václav; Navara, Mirko (2005). "Computer Analysis of Images and Patterns". *Lecture Notes in Computer Science*. **3691**: 407. doi:10.1007/11556121\_50. ISBN 978-3-540-28969-2

## IMPACT OF IMAGE RESOLUTION ON PAVEMENT DISTRESS DETECTION USING PICUCHA METHODOLOGY

*Reus Salini<sup>1</sup>, Bugao Xu<sup>2</sup> and Mena Souliman<sup>3</sup>*

1 *Neogennium Technologies, Florianópolis, Brazil; [salini@neogennium.com](mailto:salini@neogennium.com)*

2 *The University of Texas at Austin, School of Human Ecology, Center for Transportation Research, Austin, United States of America; [bxu@utexas.edu](mailto:bxu@utexas.edu)*

3 *The University of Texas at Tyler, Departments of Civil Engineering and Construction Management, Tyler, United States of America; [msouliman@uttyler.edu](mailto:msouliman@uttyler.edu)*

### ABSTRACT

An accurate and regular survey of the road surface distresses is a key factor for pavement rehabilitation design and management, allowing public managers to maximize the value of the continuously limited budgets for road improvements and maintenance. Manual pavement distress surveys are labor-intensive, expensive and unsafe for highly-trafficked highways. Over the years, automated surveys using various hardware devices have been developed and improved for pavement field data collection to solve the problems associated with manual surveys. However, the reliable distress detection software and the data analysis remain challenging. This study focused on the analysis of a newly-developed pavement distress classification algorithm, called the PICture Unsupervised Classification with Human Analysis (PICUCHA) method, particularly the impact of image resolutions on its classification accuracy. The results show that a non-linear relationship exists between the classification accuracy and the image resolution, suggesting that images with a resolution around 1.24 mm/pixel may provide the optimal classification accuracy when using the PICUCHA method. The findings of this study can help to improve more effective uses of the specialize software for pavement distress classification, to support decision makers to choose cameras according to their budgets and desired survey accuracy, and to evaluate how existing cameras will perform if used with PICUCHA.

### KEYWORDS

Pavement Engineering, Automatic Distress Detection, PICUCHA Method

### INTRODUCTION

The pavement surface condition assessment provides the most important information for a proper pavement management as well as for pavement rehabilitation design. The manual assessments, common decades ago, are no longer viable for many reasons such as high costs, high labor demand, and high risks for staff on current trafficked highways.

Over the years different imaging technologies were developed or adapted for automated pavement surveys, including traditional cameras that take an image covering a rectangular area on every shot, line-scan cameras that take one single line of pixels on every shot, and 3D cameras that read one transversal lane profile on every shot. Despite the progress on the hardware used in the field survey, the distresses detection and analysis software for generating field data remains relatively underdeveloped.

Koutsopoulos and Downey developed an alternative procedure for automated classification of asphalt pavement distresses recorded in video or photographic films based on a model that described the statistic properties of pavement images. In addition to image enhancement and segmentation, the distresses were detected by searching for primitive blocks of pixels to detect different types of cracks [1].

Lin and Liu used Support Vector Machine (SVM), a topology of artificial intelligence to detect potholes in pavement pictures. The pavement texture was detected by using the histogram and a non-linear SVM was built to classify target regions into potholes or non-potholes. The experimental results showed that the approach could achieve satisfactory results [2].

Detecting potholes was also the subject in Koch and Brilakis' study. The images were first segmented into defect and non-defect regions using the histogram-based thresholding. The potential pothole shape was then approximated by utilizing morphological thinning and elliptic regression. The texture inside a potential pothole was then compared with the texture of the surrounding area to decide if it represented a pothole or not. The routine was implemented in MATLAB [3]. After the procedure was improved by using a vision tracker to reduce the computational effort and improve the detection and pothole counting [4].

An approach combining analytic hierarchy process (AHP) and fuzzy logic theory for pavement condition assessment was developed by Sun and Gu. AHP was used to determine a weight from a paired comparison matrix and an evaluation with fuzzy relations, combining the evaluation of five different indicators: roughness, deflection, surface deterioration, rutting and skid resistance. A maximum grade principle and a defuzzified weighted cumulative index were proposed to assess the condition of a road [5].

To detect the pavement distresses on images, Ouyang, et al. tried an approach based on filtering the images to remove the background or pavement texture, image enhancements, segmentation and Canny edge detection [6].

For distresses identification on concrete pavements, Tsao, et al. developed a rule-based vision system [7]. The system had a knowledge database with facts and rules to identify different types of distresses by gathering information on the input images and deciding the optimum sequence of operations for the processing.

Ting, et al. used an approach based on the k-means classification algorithms to identify the pavement distresses on pictures. The images were processed and filtered in order to keep only black-and-white pixels that were assumed as related to cracks. The images were then grouped in clusters as distresses being detected by a decision-tree algorithm capable of recognizing horizontal, vertical, alligator and man-hole-like cracks [8].

Rababaah, et al. did a comparison of different algorithms including genetic algorithms, multilayer perceptron and self-organizing maps subdivided in image processing, crack detection, crack representation and crack classification, and discussed the impact of the representation on the final classification [9].

Nguyen, et al. performed a cracks detection technique using a sort of conditional texture anisotropy to characterize and classify the pixels as "crack" or "crack-free" pixels [10]. The idea was to detect variations of features, including noise, continuity, homogeneity and others. The

authors claimed the method could also detect other patterns such as pavement joints.

Puan, et al. developed an automated pavement imaging program (APIP) for pavement distresses assessment, capable of working with longitudinal, transverse and alligator cracks, and analyzing the crack severity by using a number of different algorithms [11].

Tsai, et al. took image segmentation as a kind of preprocessing for distresses detection and classification. Six different algorithms were used and evaluated with images taken near the city of Atlanta, USA, with varying lighting condition, shadows and cracks [12].

## PICUCHA FOR PAVEMENT DISTRESSES ASSESSMENT

The PICTure Unsupervised Classification with Human Analysis (PICUCHA) method is a new approach for pavement distresses assessment that combines the human flexibility to recognize patterns on images with the neural network ability to match patterns by similarity, expanding the (human) pavement engineer decisions over large image sets.

PICUCHA has been designed to circumvent the limitations commonly found on other methodologies such as the variations on the pavement color and texture, handling all the patterns registered on images, distresses or not. PICUCHA can detect good pavement, raveling, complex or isolated cracks, block or alligator cracks, sealed cracks, patches, potholes, painted horizontal signals, like white or yellow strips, reflective signs attached to the pavement, drainage devices, embedded inductive loops, joints, asphalt bleeding, or any combination of two or more of such patterns, among others. It can analyze road sections with mixed pavement types, like asphalt and concrete, with any kind of surface texture, color or pattern, including anti-slippery strips or cuttings, and with the presence of complex or solid shadows.

PICUCHA is capable of analyzing orthogonal images (“downward facing”) taken in the field with any device technology (line-scan, area scan, laser crack measurement system [LCMS], ...), different sources of illumination (laser, incandescent, LED, ...) and different image dimensions such as 512 x 2048 or 2048 x 2048 pixels. The PICUCHA approach is structured in a few steps including field survey, key patterns extraction, key patterns analysis by a pavement engineer, and the engineer’s decisions expansion to all the images in a given set, as shown in *Figure 1*.

The PICUCHA method is an extension of our previous developments on new methodologies and artificial intelligence applied for pavement engineering, including pavement management with genetic algorithms [13], pavement modeling with neural networks [14], the aside failure criteria that opens a new frontier of possibilities [15], and a deflection basin geometry analysis to calculate strains [16].

### 1 Field survey

The field survey is done with any equipment capable to take downward facing pictures.

The PICUCHA algorithms can process images taken with any device brand or technology including:

- Line-scan or area-scan camera, laser crack measurement systems (LCMS) or other;
- With laser, incandescent, LED or other types of lamps, or just natural illumination; and,
- Images with any size and resolution.

## 2 Key patterns identification

The images are sliced into cells (e.g. 128 x 128 pixels) and a special algorithm will analyze to identify and extract the key patterns. There is no predefinition of distresses or limitations, the self-learning algorithm deal with any kind of pattern existing in a given image set.

## 3 The human pavement expert analysis

The key patterns are analyzed by a human pavement expert that will describe the distresses and other desired characteristics with base on any standard or manual for distresses assessment. This procedure avoids the problem to rely just on software tools and keeps the human expert on top of the process.

## 4 The human pavement expert analysis expanded to all images

The human pavement expert description is used to refeed the algorithms that will expand such decisions to all the images in the given set, generating the final report.

Figure 1 - Flow chart of PICUCHA Method's main steps

## RELEVANCE OF CAMERAS AND IMAGE RESOLUTIONS

Over the years the companies developed different cameras technologies and other devices for pavement surface condition assessment with growing image resolutions. The most common are the area-scan cameras, line-scan cameras and laser crack measurement systems (LCMS). Those devices are available from different suppliers and integrators ("brands"), and can be purchased at different image resolutions. The camera type and resolution have a direct impact on the image quality and an even heavier relevance for the equipment's cost.

Area-scan cameras were the first generation of equipment for pavement survey. They are adaptations of general purpose cameras (*Figure 2.a*) and are notorious for its low cost. Some integrators assemble two cameras together for a higher resolution. This type of camera takes a rectangular image on every shot (e.g. 2048x512 pixels) that results in a number of problems, especially image distortions since some pavement areas are closer to the camera lens than others, and non-homogeneous illumination, because some areas of the pavement are closer to the illumination source than others. Those problems are especially visible when two or more images are assembled together and generate an extra challenge for the distresses detection by software. Area-scan cameras are not compatible with laser illumination, requiring many lamps that usually are strobe flashlights.

Line-scan cameras represent an advance in technology and image quality (*Figure 2.b*). As its name suggests, it takes one single line of pixels on every shot (e.g. 2048 x 1 pixels). Image distortions and illumination heterogeneity are minimal. The line-scanned pixels can be assembled together to generate a consistent and flat rectangular image. It is compatible with laser (beam) illumination in addition to incandescent, LED and others.

The laser crack measurement systems (LCMS) collect two different information at the same time: an image and a transverse profile (*Figure 2.c*). The image is usually a by-product for this equipment and its quality tends to be low. The analysis is performed by using the profile data to locate the cracks over the image. It is especially accurate to identify cracks and rutting. Some

integrators install the LCMS together with line-scan cameras for a better image quality. Other integrators also install high accuracy accelerometers, allowing using the data for a kind of pavement topographical survey. This technology is relatively new and well-known for its high cost, which is frequently higher than one million dollar for a vehicle with a LCMS system.

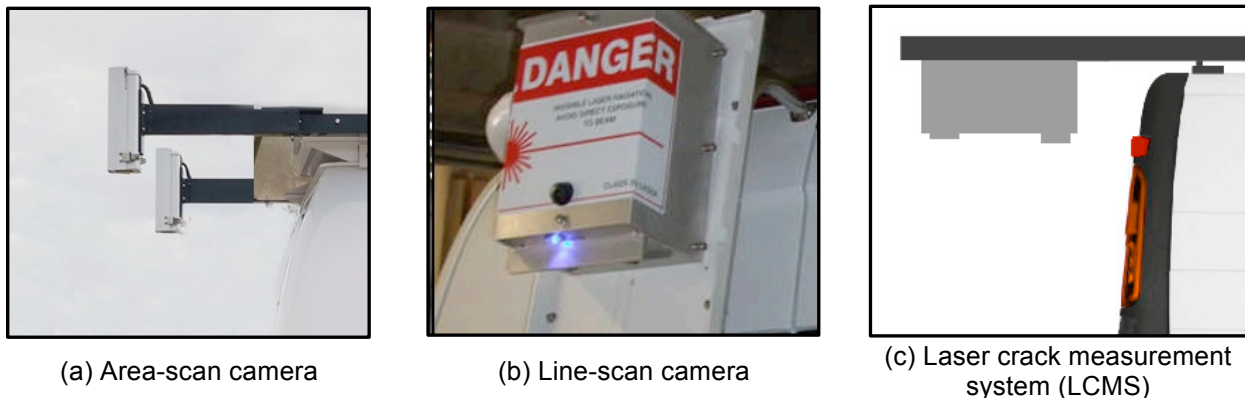


Figure 2 - Camera technologies for pavement surveys

Regardless of the camera technology, there is a consensus that, the higher the image resolution, the easier and more accurate the pavement distresses assessment will be. However, higher resolution implies in higher costs.

Frequently the resolution is improved by raising the number of cameras, e.g. two 2048 pixels resolution cameras are integrated to provide a final resolution of 4096 pixels. Up to eight cameras have been used together so far. Survey systems with higher resolutions are more expensive and complex from a technical perspective, with implications for integration, calibration, operation, data acquisition and storage, and maintenance. Thus, camera resolution is an extremely important factor to be taken in consideration at the time to choose a system for pavement surface survey. On the other hand, a software system capable to provide an accurate distresses assessment working with rather limited resolution images has the potential to make an important and positive impact for this industry, making it feasible to use affordable cameras and revitalizing the use of simple pavement survey systems.

This study explores the PICUCHA method performance for images with different resolutions. For this purpose an image at five different resolutions was tested and the method's error was evaluated regarding to how many cells were misclassified, i.e., how many cells were grouped together with cells showing different characteristics or distresses. The objective is concentrated on evaluating how the PICUCHA self-learning algorithms will perform on the grouping task only, without a final distresses description because it requires additional steps unwanted for this particular study.

### PICUCHA ACCURACY AT DIFFERENT IMAGE RESOLUTIONS

An image taken with a line-scan camera with an original resolution of 2048 x 512 pixels, and covering an area of approximately 3.6 x 0.9 m (Figure 3), was downsized to the tested resolutions. Such image was chosen because it is representative of how PICUCHA performs. In addition it shows different kinds of patterns, including good pavement, raveling, cracks with different severities and a white strip. The 3D points mesh as well as the pixels decks with artificial colors for such image are shown on Figure 4 and Figure 5, respectively. They are part of

PICUCHA intermediate steps for the data processing that are not the focus of this study.

All the image resampling was completed from the original image at full resolution (2048 x 512 pixels) to the required size using bicubic interpolation with a sharpness factor of 0.51, that is the most common method for digital image resizing [17], as shown on *Table 1*.



*Figure 3 - Image with original resolution of 2048 x 512 pixels*

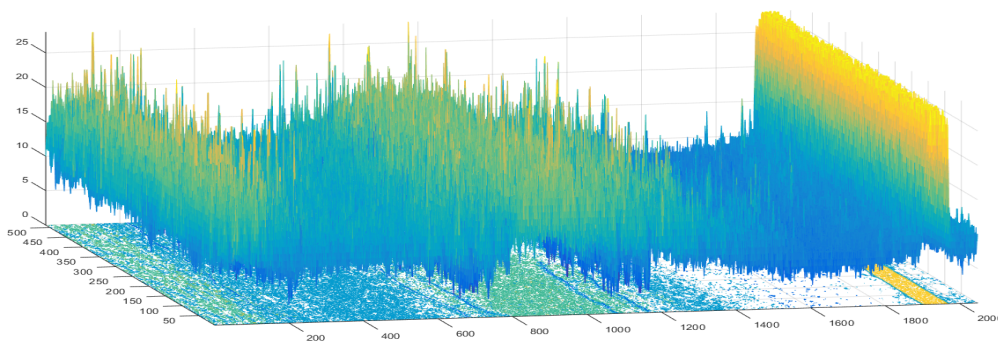


*Figure 4 - The 3D mesh of points representation for the 2048x512 pixels image*

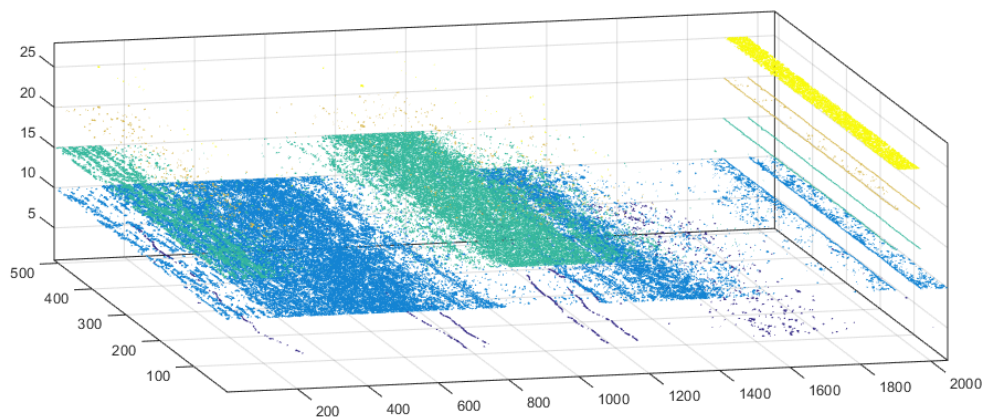


*Figure 5 - The 3D pixel decks for the 2048x512 pixels image*

Table 1 - Resolutions for the tested image

Original image size (pixels)		Reduction	Reduced image size (pixels)		Resolution (mm/pixel)
Horizontal	Vertical		Horizontal	Vertical	
2048	512	0.0%	2048	512	1.76
2048	512	12.5%	1792	448	2.01
2048	512	25.0%	1536	384	2.34
2048	512	37.5%	1280	320	2.81
2048	512	50.0%	1024	256	3.52

The image, at its five different resolutions, was submitted for classification using PICUCHA algorithms. To keep the test consistency and the image slicing to the same number of cells for every case, the cell size was reduced in the same proportion of the image resizing, as shown in Table 2. The classification results are shown in Figure 6-10 where the generated groups can be seen. Because of the unsupervised nature of this artificial intelligence approach the cells marked with the same color belong to the same group and should have the same pattern. The cells that do not attend that criteria, i.e., were included in a group with a different predominant pattern, represent the algorithm error and are marked with a “x”. The identification of misclassified cells was performed by an experienced pavement engineer. In this study the colors are used only for the groups’ identification and, because every image (Figure 6-10) represents a different processing started from the ground, same colors in different images may represent different patterns. Another situation that frequently happens is that the algorithms, while performing the self-learning, may decide to create different groups for cells with patterns that, from a human perspective, look similar. When this situation happens the (human) pavement expert analyst will, in the step 3 of this methodology (Figure 1), set that groups with the same description for the distresses accounting.

Table 2 - Number of misclassified cells according to the image resolution

Image size (pixels)		Resolution (pixels)	Cell size (pixels)	Total number of cells	Misclassified cells	Error (%)
Horizontal	Vertical					
2048	512	1048576	128	64	2	3.1%
1792	448	802816	112	64	5	7.8%
1536	384	589824	96	64	4	6.3%
1280	320	409600	80	64	7	10.9%
1024	256	262144	64	64	6	9.4%

As expected, the number of misclassified cells rose as the resolution dropped, but not in a linear way. At the highest resolution, 2048x512 pixels, the error was the smallest, with just two cells being misclassified among 64. At the lowest resolution, 1024x256 pixels, six cells were misclassified with an error rate of 9.4%. The largest error was found at resolution of 1280x320 pixels with seven cells misclassified, corresponding to an error of 10.9% as shown in Table 2.

Figure 11 shows the found errors graphically with a respective trend line and a prediction equation. On the basis of the trend line, the upper and lower limits can be plotted with a plus and minus standard deviation (3.0%), as shown in Figure 12. By extrapolating the upper limit, the ideal image dimension can be identified at a location near 2 megapixels where the theoretical error is zero. This dimension is equivalent to an image size of 2900x725 pixels, or a resolution of 1.24 mm/pixel.

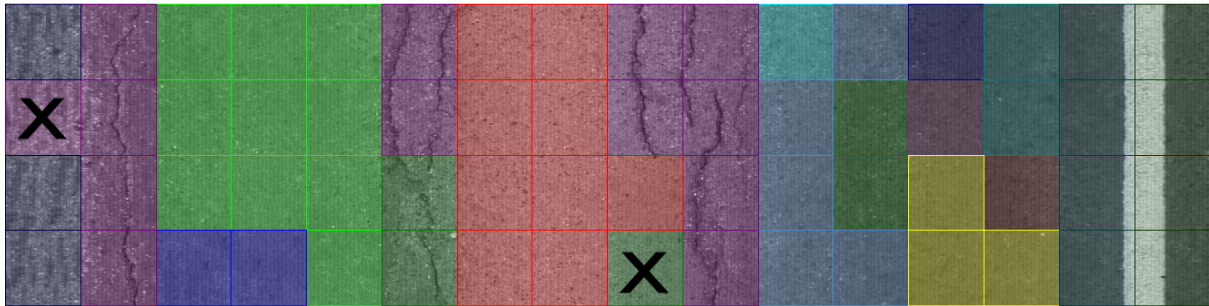


Figure 6 - Cells classification for the 2048x512 pixels image

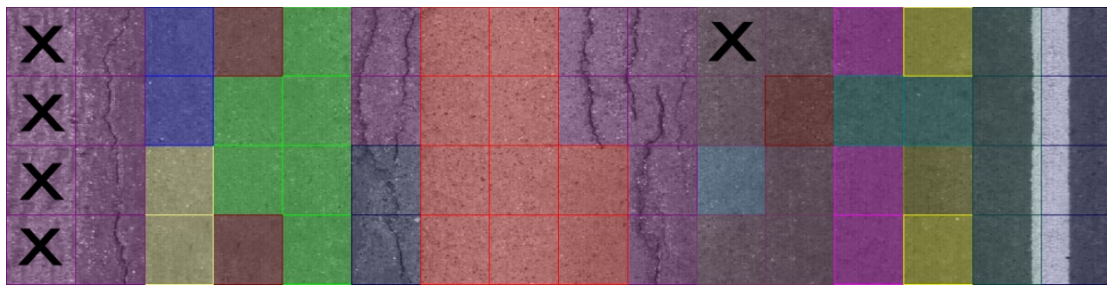


Figure 7 - Cells classification for the 1792x448 pixels image

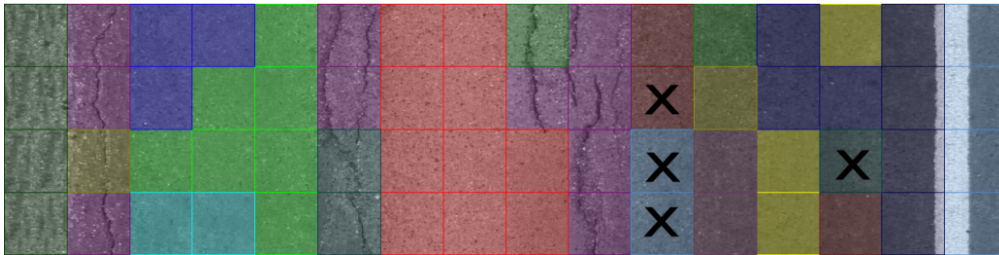


Figure 8 - Cells classification for the 1536x384 pixels image

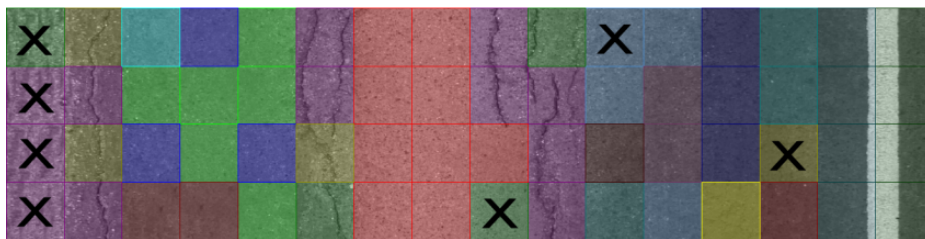


Figure 9 - Cells classification for the 1280x320 pixels image

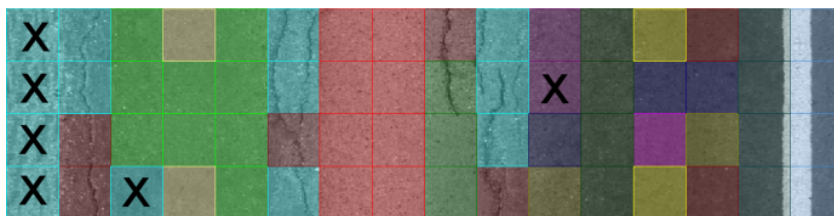


Figure 10 - Cells classification for the 1024x256 pixels image

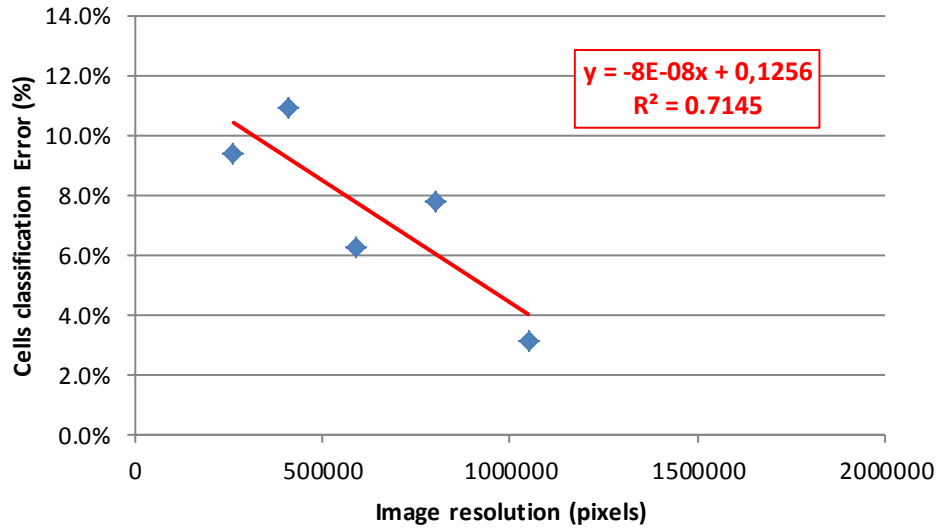


Figure 11 - Classification error according to the image resolution

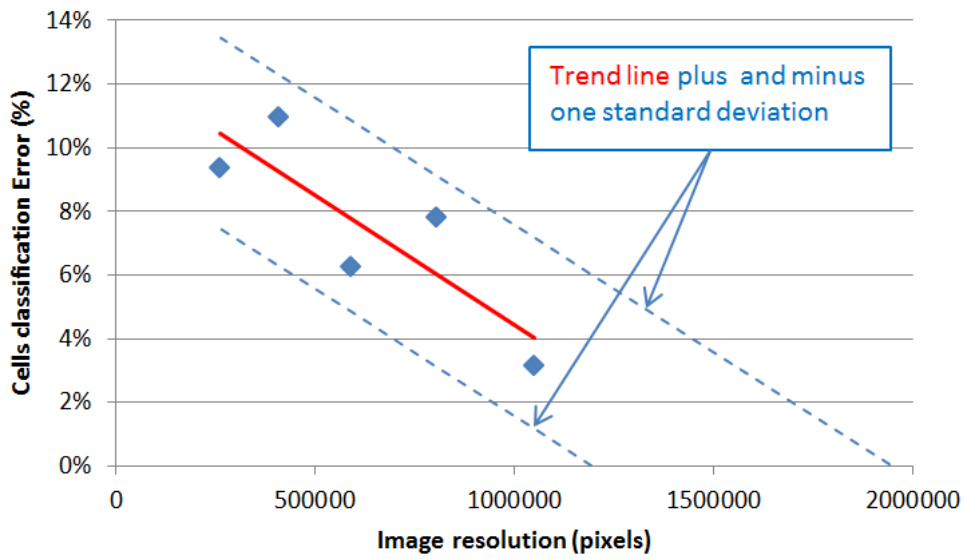


Figure 12 - Projection of ideal image resolution for PICUCHA method

## CONCLUSIONS

The PICUCHA method can be used to properly handle and classify the image at all tested resolutions. The error expressed in the number of cells misclassified, i.e. classified in groups with different predominant characteristics, rose in a non-linear way when the image resolution dropped, but was relatively low in all cases. The minimum error was 3.1% for the image with the highest resolution (2048x512 pixels) and the maximum error was 10.9% for the image with 1280x320 pixels. The image with the lowest resolution (1024x256 pixels) had 9.4% of the cells misclassified.

The error trend line analysis suggests the optimum transverse image resolution should be more than 2900 pixels, i.e., around 1.24 mm/pixel. Although this should not be assumed as a definitive parameter, it is a good resolution reference for selecting a camera system for pavement surveys when PICUCHA will be used for the analysis.

## REFERENCES

- [1] Koutsopoulos, H.N., Downey, A.B. 1993. Primitive-Based Classification of Pavement Cracking Images. *J. Transp. Eng.*, 119 (3), p. 402–418.
- [2] Lin, J., Liu, Y. 2010. Potholes detection based on SVM in the pavement distress image. *Proc. - 9th Int. Symp. Distrib. Comput. Appl. to Business, Eng. Sci. DCABES 2010*, p. 544–547.
- [3] Koch, C., Brilakis, I. 2011. Pothole detection in asphalt pavement images. *Adv. Eng. Informatics*, 25 (3), p. 507–515.
- [4] Koch, C. et al. 2013. Automated Pothole Distress Assessment Using Asphalt Pavement Video Data. *J. Comput. Civ. Eng.*, 27 (4), p. 370–378.
- [5] Sun, L., Gu, W. 2011. Pavement Condition Assessment Using Fuzzy Logic Theory and Analytic Hierarchy Process. *J. Transp. Eng.*, 137 (9), p. 648–655.
- [6] Ouyang, A. et al. 2010. Surface Distresses Detection of Pavement Based on Digital Image Processing. In: *IFIP Advances in Information and Communication Technology*. Nanchang, China, p. 368–375.
- [7] Tsao, S. et al. 1994. Image-Based Expert-System Approach to Distress Detection on CRC Pavement. *J. Transp. Eng.*, 120 (1), p. 52–64.
- [8] Ho, T. et al. 2010. Pavement distress image recognition using k-means and classification algorithms. In: *Computing in Civil and Building Engineering, Proceedings of the International Conference* (Editor: W. Tizani). Nottingham, UK: Nottingham University Press, p. 73–78.
- [9] Rababaah, H. et al. 2005. Asphalt Pavement Crack Classification: A Comparison of GA, MLP, and SOM. In: *Genetic and Evolutionary Computation Conference (GECCO'2005)* (Editor: F. Rothlauf). Washington, D.C., USA.
- [10] Nguyen, T.S. et al. 2010. Pavement Cracking Detection Using an Anisotropy Measurement. In: *11ème IASTED International Conference on Computer Graphics and Imaging (CGIM)*. Innsbruck, Austria.

- [11] Puan, O.C. et al. 2007. Automated Pavement Imaging Program (APIP) for Pavement Cracks Classification and Quantification. *Malaysian J. Civ. Eng.*, 19 (1), p. 1–16.
- [12] Tsai, Y. et al. 2010. Critical Assessment of Pavement Distress Segmentation Methods. *J. Transp. Eng.*, 136 (1), p. 11–19.
- [13] Salini, R. et al. 2015. Application of artificial intelligence for optimization in pavement management. *Int. J. Eng. Technol. Innov.*, 5 (3), p. 189–197.
- [14] Salini, R. 2010. INTELLIPave: Uma Abordagem Baseada em Inteligência Artificial para a Modelagem de Pavimentos Asfálticos. University of Minho.
- [15] Salini, R. et al. 2009. INTELLIPave - Considering aside failure criteria and unknown variables in evolutionary intelligence based models for asphalt pavement. In: *Proceedings - 23rd European Conference on Modelling and Simulation, ECMS 2009*. Madrid, Spain, p. 624–629.
- [16] Salini, R. 2004. Salini Method 2004. *Comput. Mech. Proc. Sixth World Congr. Comput. Mech. Conjunction with Second Asian-Pacific Congr. Comput. Mech.*, 2, p. 148–155.
- [17] Keys, R.G. 1981. Cubic Convolution Interpolation for Digital Image Processing. *Trans. Acoust. Speech, Signal Process.*, ASSP-29 (6), p. 1153–1160.

# NUMERICAL ANALYSIS OF THE EFFECT OF SURCHARGE ON THE MECHANICAL BEHAVIOR OF GEOCELL REINFORCED RETAINING WALL

Fei Song<sup>1</sup>, Haibo Chai<sup>1</sup>, Jian Zhao<sup>2</sup>, Mingrui Yang<sup>2</sup>

1 Institute of Geotechnical Engineering School of Highway Engineering, Chang'an University, Xi'an, 710064, P.R.China; E-mail: songf1980@163.com

2 Guizhou Electric Power Design Institute and Research Institute, Guiyang, 550002, P.R. China

## ABSTRACT

Geocell reinforced retaining structure has been widely used in civil engineering for the protection of slopes due to its advantages. In this paper, the effects of surcharge on the horizontal displacement of the wall back, the size of the sliding wedge and the factor of safety of geocell reinforced retaining wall are numerically analyzed by employing the geotechnical finite element method software Plaxis. The research results show that, when the distance of surcharge from the wall face is small, the maximum and the minimum deformation of the wall back takes place near the top of the wall and the wall bottom respectively. After the distance of surcharge from the wall face exceeds about 13% of the wall height, the surcharge has little effect on the horizontal deformation of the wall back, the size of the sliding wedge and the safety factor of geocell reinforced retaining wall. The horizontal deformation of the wall back gradually increases with the increase of the length of the surcharge until it reaches a certain value. The effect of the length of the surcharge on the failure surface is not significant. Besides, the factor of safety of the wall gradually decreases with the increase of length of the surcharge. However, with the increase of the distance of the surcharge from the wall face, the influence of the length of the surcharge on the safety factor gradually becomes small. The study results can supplement theoretical basis for the design of geocell reinforced retaining walls in engineering practices.

## KEYWORDS

Geocell reinforced retaining wall, surcharge, sliding wedge, horizontal displacement, safety factor

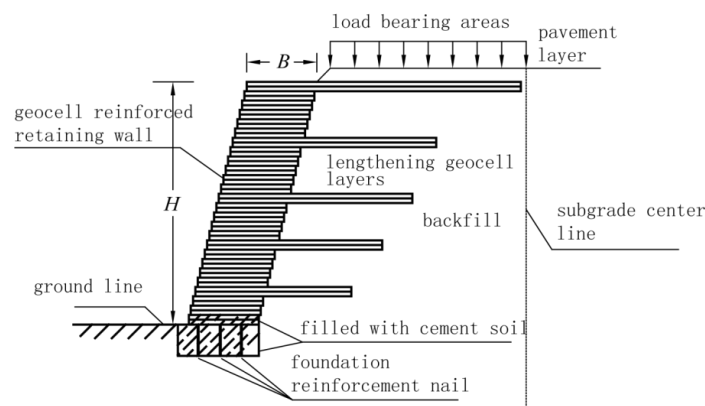
## INTRODUCTION

Geosynthetics are widely used as reinforcing members in the construction of earth structures due to its superior properties compared with other materials, such as those of Zigler and and Pokorný (2005) [1], Liu (2016) [2]. In recent years, the use of geosynthetic materials for reinforced slopes and retaining walls has increased significantly throughout the world because of the increasing infrastructural development demands. A lot of research efforts have been made to study geosynthetic-reinforced soil structure.

Leshchinsky (1989) conducted a limit equilibrium analysis for the internal stability of geosynthe-reinforced vertical walls and studied the influences of two possible extreme inclinations of the reinforcement's tensile resistance [3]. Wong and Broms (1994) conducted a series of model tests to study the failure modes of a geotextile-reinforced soil wall [4]. Porbaha and Goodings (1996) studied the effect of the foundation soil, the slope inclination angle and the geotextile strengths on the reinforced wall behavior by centrifuge model tests of twenty-four models of geotextile-reinforced cohesive-backfill retaining walls [5]. Rowe and Skinner (2001) performed a numerical examination of the behavior of an 8 m high geosynthetic reinforced soil wall constructed on a layered foundation stratum [6]. Koerner and Soong (2001) presented the evolution and a cost survey of geosynthetic reinforced segmental retaining walls in general [7]. They also compared three design methods in detail. Yoo (2004) explored the possible causes of distress and unexpected large lateral wall movements of a 6-year-old geosynthetic-reinforced segmental retaining wall and recommended several remedial measures [8]. Hatami and Bathurst (2005) developed a numerical model to simulate full-scale, geosynthetic-reinforced soil walls under working stress conditions [9]. Bathurst et al. (2006) investigated the influence of facing type and stiffness on the reinforcement loads by the measurements of two instrumented full-scale walls with different facing stiffness [10]. Benjamim et al. (2007) measured the internal distribution of reinforcement strains, the overall vertical and horizontal movements within the reinforced soil mass, as well as face displacements by field monitoring a geotextile-reinforced soil-retaining prototype wall [11]. Won and Kim (2007) measured local deformation of geosynthetics, such as geogrids, and nonwoven and woven geotextiles, to analyze the stability of geosynthetic-reinforced soil (GRS) structures [12]. Sabermahani et al. (2009) studied the seismic deformation modes of reinforced-soil walls by conducting a series of 1-g shaking table tests on 1 m high reinforced-soil wall models [13]. Bathurst et al. (2009) studied the influence of reinforcement stiffness and compaction method on wall displacement by field monitoring four geosynthetic-reinforced soil walls [14]. Leshchinsky (2009) established a benchmark test and examined the validity of the three existing design methods in the United States [15]. Ehrlich et al. (2012) performed a physical model study of the influence of compaction on the behavior of geogrid-reinforced soil walls [16]. Suksiripattanapong et al. (2012) performed a numerical analysis of the bearing reinforcement earth wall by PLAXIS 2D [17]. Liu (2012) estimated the lateral facing displacement at the end of construction as well as after years of creep of geosynthetic-reinforced soil segmental retaining walls by FEM analysis [18].

Although considerable interest has been shown in reinforced walls, little has been published concerning geocell retaining structures, shown in *Figure 1*. Due to its unique three-dimensional geometry, geocell can provide great lateral confinement to the infill soil without relying on the interlocking or friction with the infill soil. The geocell reinforced retaining structures have been used extensively in embankment and slope protection due to the advantages of simple installation, cost-effectiveness and ecological protection. Xie and Yang (2009) studied the deformation and mechanical properties of geocell retaining walls by the FEM numerical simulation [19]. Chen and Chiu (2008) performed on nine model geocell retaining walls and examined the facing displacement and settlement of backfill [20]. Song et al. (2011) analyzed the effects of the aspect ratio, slope inclination angle and surcharges on the deformation behavior of the geocell retaining wall by the numerical analysis [21]. Chen et al. (2013) assessed the stability and deformation of geocell structures with various layouts by numerical analysis [22]. Song et al. (2013a) investigated the failure process of the geocell reinforced retaining wall with surcharge acting on the backfill surface by means of the centrifugal model tests [23]. Song et al. (2013b) studied the effects of soil strength and the strength of geocell structure on the failure surface of geocell reinforced retaining wall by numerical simulation [24]. Song et al. (2014a) performed a series of centrifuge model tests on geocell reinforced retaining wall to study the effect of aspect ratio and the slope inclination on

the failure surface. In addition, they compared measured failure surfaces with those predicted by Coulomb and Rankine's earth pressure theories and revealed the differences [25]. Song et al. (2014b) studied the optimum sectional form of the geocell reinforced retaining wall by numerical analysis [26]. Song et al. (2014c) formulated mathematical expression of the failure surfaces of geocell reinforced retaining walls with different height-width ratios and backfill strengths [27]. However, the mechanical behavior of geocell reinforced retaining walls with surcharge acting on is not systematically investigated.



(a) Schematic diagram of geocell reinforced retaining wall



(b) Photo of geocell reinforced retaining wall

Figure 1 - Geocell reinforced retaining structures used for embankment protection

In this paper, by employing the geotechnical finite element method software Plaxis, the numerical models of geocell reinforced retaining walls with surcharge acting on are formulated and the mechanical behavior of the wall is studied by numerical simulation. On the basis of analysis of the numerical simulation results, the effects of the distance of the surcharge from the wall face and the length of the surcharge on the horizontal displacement, the sliding surface and the safety factor of the wall are investigated. The research results provide theoretical basis and references for the design of the wall.

### Model and parameters of calculation

By employing the geotechnical finite element method software Plaxis, the mechanical behavior of a geocell reinforced retaining wall with surcharge acting on is numerically simulated in order to study the effect of the surcharge on the horizontal deformation, the failure surface and the

safety factor on the wall. In this study, the geocell reinforced soil is treated as a composite material with addition cohesive strength and stiffness resulted from the confinement effect. Because of its convenience and simplification, such 2-dimensional equalient model has been employed and its effectiveness has been validated by Mhaiskar and Mandal (1996) [27], Bathurst and Knight (1998) [28], Latha (2000) [29], Rajagopal et al. (2001) [30], Latha et al. (2006) [31], Latha and Rajagopal (2007) [32], Latha et al. (2008) [33], Xie and Yang et al. (2009) [19], Latha et al. (2009) [34], Chen et al. (2013) [22], Mehdipour et al. (2013) [35]. In the computation, the 15-node triangular element is employed in this analysis to model soil, the geocell reinforced soil and the foundation. An elastic-plastic model employing the Mohr-Coulomb criterion is adopted for the backfill, the geocell reinforced soil and the foundation. In addition, the interface element is set between each geocell structure layer, between the wall back and backfill, and also between the foundation and the soil to model the interaction between the structure and the soil. Phi-c reduction in Plaxis is employed to calculate failure surfaces and safety factors of the wall. The details of constitutive model of the materials, the interface element, the phi-c reduction method and the definition of safety factor in Plaxis can be referred to Brinkgreve and Broere (2000) [36], Song et al. (2013b) [24].

With references to calculation parameters adopted by Wang (2004) [37], Xie and Yang (2009) [19], based on the analysis of the mechanical property tests of geocell by Yang (2005) [38], the mechanical parameters of the wall body, the foundation and the backfill in this study are selected and listed in Table 1. In order to be conservative, the magnitudes of the strength and modulus of the geocell wall body are a little smaller than the ones previously adopted.

Table 1 - Calculation Parameters of Model

Material	Wall Body	Foundation	Backfill
$\gamma/(\text{kN/m}^3)$	18	20	17
$\gamma_{\text{sat}}/(\text{kN/m}^3)$	20.5	22	20
$c/\text{kPa}$	45	70	30
$\phi/(\text{°})$	30	45	25
$E/\text{MPa}$	50	65	30
$\nu$	0.25	0.2	0.35
$R_{\text{inter}}$	0.67	0.67	0.67

The calculation model illustrated in *Figure 2* is composed of the geocell structure layers, the foundation and the backfill. *a* and *b* in *Figure 2* represent respectively the distance of the surcharge from the face and the length of the surcharge. In the computation, the height of the geocell reinforced retaining wall is 10m, the width of the wall is 4m and the slope ratio is 1:0.25. In addition, the height of each geocell layer is 40cm. The geocell reinforced retaining wall and the foundations are built by stage construction in nine steps. The foundation is constructed in the first step and the embankment and geocell reinforced retaining wall are filled by 2m/d in the following eight steps. As is shown in *Figure 2*, ten representative points are selected along the wall back in order to study the horizontal deformation of the wall in different conditions. If the wall toe is selected as coordinate origin, the coordinates of the ten points from the wall top to the wall bottom are respectively A(6.5, 10.0), B(6.3, 9.0), C(6.0, 8.0), D(5.7, 7.0), E(5.5, 6.0), F(5.2, 5.0), G(5.0, 4.0), H(4.7, 3.0), I(4.4, 1.5), J(4, 0). After the construction is finished, surcharge is exerted on the backfill surface and the horizontal deformation is predicted by a plastic calculation. After that, the failure surface and the factor of safety are calculated by the strength reduction method built in Plaxis.

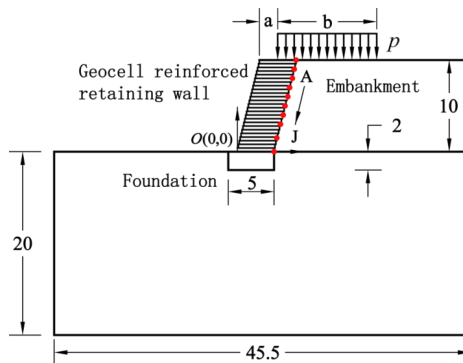


Figure 2 - Sketch of the calculation model (Unit: m)

### EFFECT OF DISTANCE OF SURCHARGE FROM THE WALL FACE

The initial stress field is produced by  $K_0$  procedure in Plaxis. The deformation caused by the initial stress has no actual physical meanings and is therefore removed in the first step of the calculation, which can eliminate the effect of the deformation induced by the initial stress on the successive stress and displacement field. In the successive analysis,  $p$  and  $H$  represent the magnitude of the surcharge and the wall height respectively. In the computation,  $b=5\text{m}$ , i.e.  $b/H=0.5$ , and only the value of  $a$  is changed. In some cases, for example, when  $a/H=0.1\sim 0.4$ ,  $p=150\text{kPa}$ , the soil body collapses and the calculation cannot be completed. The horizontal deformation of the wall back with different  $a/H$  values is shown in Figure 3. The case of the wall without surcharge acting on is superimposed in the figure for comparison.

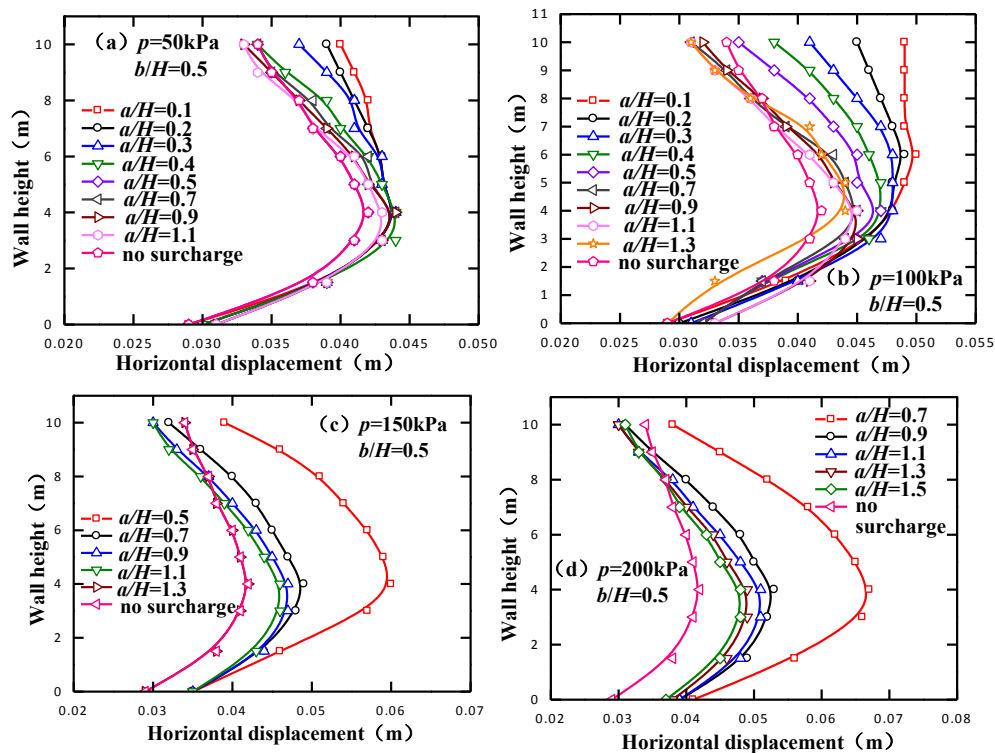
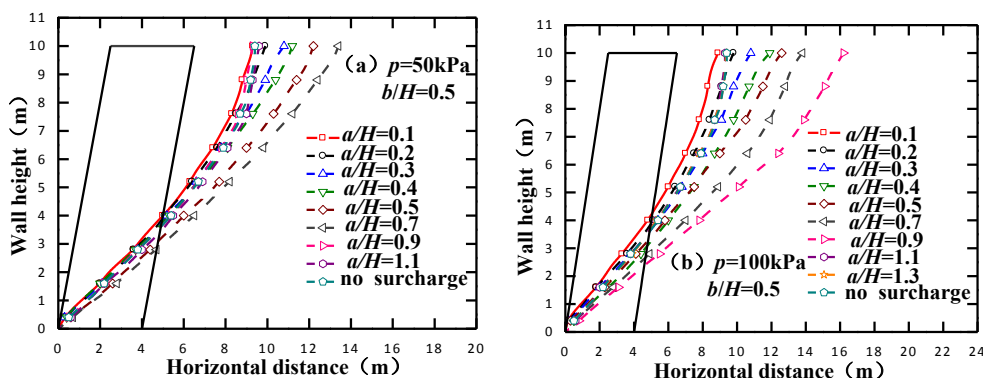


Figure 3 - Effect of distance of surcharge from wall face on the horizontal deformation (Unit: m)

It can be observed from *Figure 3* that when the surcharge is near the wall face, the maximum deformation of wall back takes place near the top of the wall for the cases of  $p=100\text{kPa}$  and the difference between the horizontal deformation of the top of the wall and that at about  $H/3$  above the wall heel is relatively small for the cases of  $p=50\text{kPa}$ . For the case of  $p=100\text{kPa}$ , with the increase of the distance of the surcharge from the wall face, the location where the maximum deformation of wall back occurs gradually descends and the shape of the curve representing the deformation of the wall back changes. For all the cases, with the increase of the distance of the surcharge from the wall face, the horizontal displacement gradually decreases and the shape of the curve becomes the one with the largest horizontal deformation at location about  $H/3$  above the wall heel, from which the horizontal deformation gradually decreases toward the wall top and wall heel respectively, which is the same case with the wall without surcharge revealed by the previous studies of Song et al. (2011). This indicates that with the increase of the distance of the surcharge from the wall face, the effect of the surcharge on the horizontal displacement gradually becomes less significant. Particularly, for the cases of  $p=150\text{kPa}$  and  $200\text{kPa}$ , the turning points from which the horizontal deformation sharply decreases are  $a/H=0.7$  and  $a/H=0.9$  respectively. Besides, after  $a/H$  value becomes larger than  $0.4$  and  $0.7$  respectively for the cases of  $p=50\text{kPa}$  and  $100\text{kPa}$ , the horizontal deformation decreases slowly.

The failure surfaces of the retaining wall and the backfill with different  $a/H$  values are shown in *Figure 4*, from which it can be seen that when the value of  $a/H$  is small, the location where the sliding surface intersects with the wall back is relatively high and the distance between the top of the sliding surface and the wall is relatively small, indicating that the size of the sliding wedge is small. However, with the increase of  $a/H$ , the location where the sliding surface intersects with the wall back gradually descends and the distance between the top of the sliding surface and the wall gradually increases, leading to the enlargement of the size of the sliding wedge. Nevertheless, it is very interesting to note that after  $a/H$  increases to a certain value, the size of the sliding wedge does not increase any more. On the contrary, it begins to decrease and maintain almost a constant value with the continuing increase of  $a/H$ . The turning points for the case of  $p=50\text{kPa}$ ,  $100\text{kPa}$ ,  $150\text{kPa}$  and  $200\text{kPa}$  are  $a/H=0.7$ ,  $0.9$ ,  $1.1$  and  $1.3$  respectively. After  $a/H$  value becomes larger than that of the turning point, the surcharge has little influence on the failure surface of the geocell reinforced retaining wall and the failure surface becomes the same one with that of the wall without surcharge acting on.



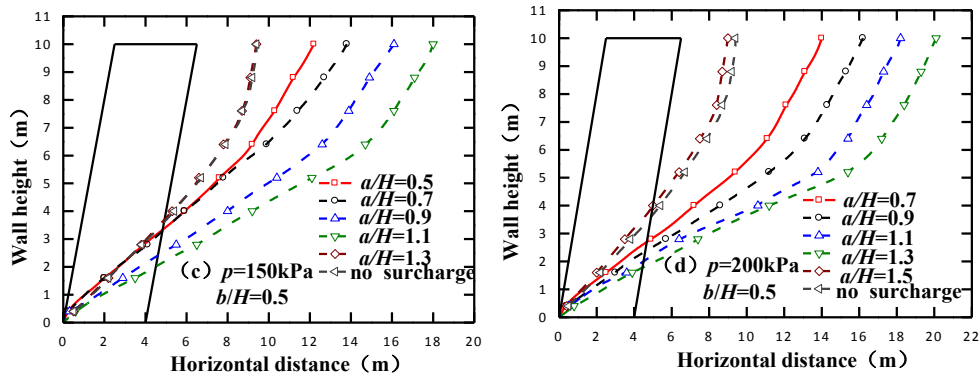


Figure 4 - Effect of distance of surcharge from wall face on the sliding surface (Unit: m)

The variation of the safety factor with  $a/H$  values is illustrated in Figure 5. It can be known that the safety factor of the wall without surcharge acting on is 1.423 by computation. It can be observed from Figure 5 that the safety factor increases with  $a/H$  value. However, after  $a/H$  increases to a certain value, about  $0.5H$ ,  $0.9H$ ,  $1.1H$  and  $1.3H$  for the cases of  $p=50\text{kPa}$ ,  $100\text{kPa}$ ,  $150\text{kPa}$  and  $200\text{kPa}$  respectively, the safety factor maintains a constant value which is about the same one with that of the wall without surcharge acting on, showing that the effect of surcharge on the safety factor becomes small after  $a/H$  value increases to the one larger than that of the turning point.

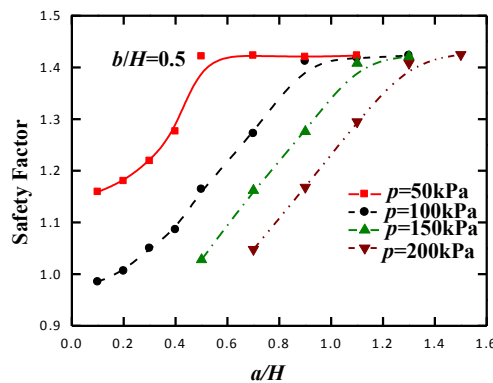


Figure 5 - Effect of distance of surcharge from wall face on the safety factor

### Effect of length of surcharge

The effect of the length of the surcharge on the horizontal deformation, the sliding surface and the safety factor are also computed and analyzed by employing the geotechnical finite element method software Plaxis and  $p=100\text{kPa}$  in the computation. The deformation of the wall back with  $b/H=0.5$ ,  $1$ ,  $1.5$ , and  $2$  for different  $a/H$  values are shown in Figure 6, from which it can be seen that the horizontal deformation of the wall back is relatively small with small  $b/H$  values and it gradually increases with the increase of  $b/H$ . However, after the  $b/H$  value increases to be larger than a certain value, about  $1.0$  for the cases of  $a/H=0.2$ ,  $0.5$  and  $0.8$ , the horizontal deformation changes very little. For the case of  $a/H=0.2$ , with the increase of the length of the surcharge, the location where the maximum deformation of wall back occurs gradually rises to the middle part of the wall. The maximum deformation of the middle part of the wall is much larger than the other part of the wall, resulting in an acute angle in the middle part of the deflection curve.

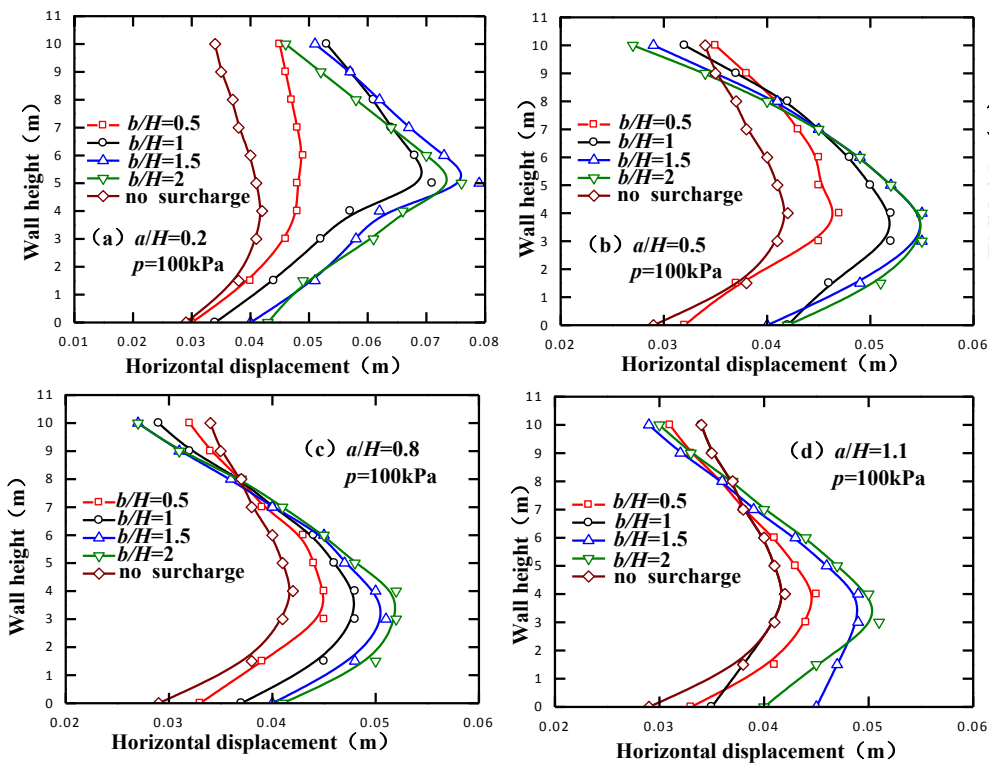
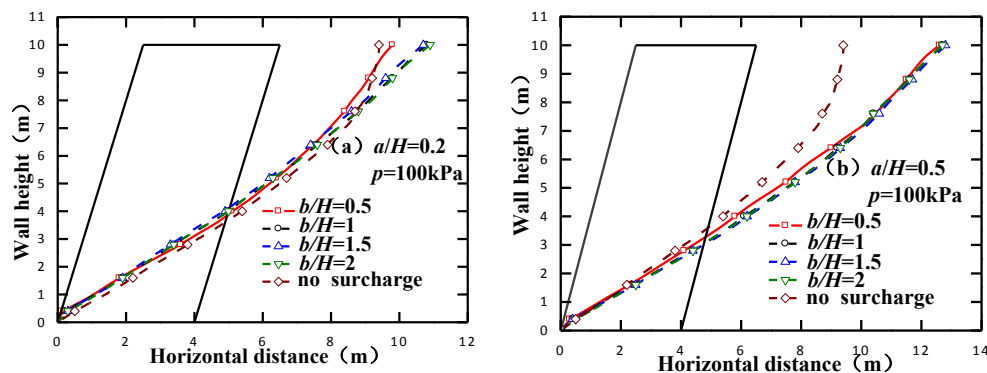


Figure 6 - Effect of length of surcharge on the horizontal deformation (Unit: m)

The sliding surfaces of the wall and the backfill with  $b/H=0.5, 1, 1.5$  and  $2$  for different  $a/H$  values are provided in Figure 7, from which it can be observed that the sliding surfaces with different  $b/H$  values are almost the same one, indicating that the effect of the length of the surcharge on the sliding surface is not obvious. When  $a/H$  is small, the sliding surface is almost the same one with the wall without surcharge acting on. With the increase of the value of  $a/H$ , the size of the sliding wedge gradually increases. However, when  $a/H$  increases to be larger than  $1.1$ , the size of the sliding wedge reduces to be the one with the wall without surcharge acting on, which has been discussed previously concerning the influences of the distance of the surcharge from the wall face.



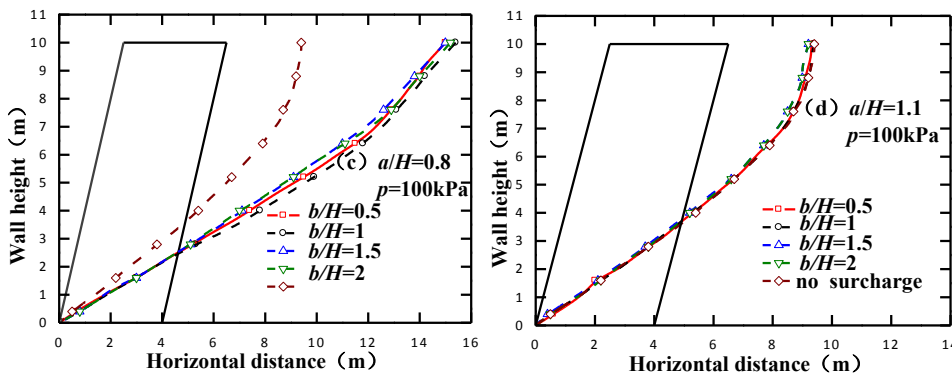


Figure 7 - Effect of length of surcharge on the sliding surface

Safety factors of the wall with  $b/H=0.5, 1, 1.5$  and  $2$  for different  $a/H$  values are computed by phi-c reduction method and shown in Figure 8. It can be observed from Figure 8 that the safety factor of the wall is large with small  $b/H$  values. However, it gradually decreases with the increase of the value of  $b/H$ . Nevertheless, with the increase of  $a/H$ , the influence of the length of the surcharge on the safety factor gradually becomes small. For example, when  $a/H=1.1$ , the length of the surcharge has no effects on the safety factor of the wall, which does not vary with the value of  $b/H$  and remains the same value with that of the wall without surcharge acting on.

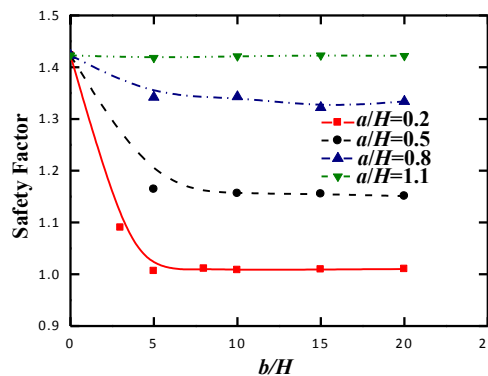


Figure 8 - Variation of Safety factors of the wall with  $b/H$  values

## CONCLUSION

In this paper, the effect of the distance of the surcharge from the wall face and the length of the surcharge on the horizontal deformation, the failure surface and the factor of safety is studied by employing the geotechnical finite element method software Plaxis. The following conclusions can be primarily drawn on the basis of the analysis of the numerical simulation results.

(1) When the distance of the surcharge from the wall face is small, the horizontal deformation of the wall back is large. When the surcharge moves away from the wall face, the horizontal displacement gradually decreases and the shape of the curve representing the horizontal deformation of the wall back becomes the same one of the wall without surcharge acting on.

(2) When the distance of the surcharge from the wall face is small, the size of the sliding wedge is small. However, with the increase of the distance of the surcharge from the wall face, the size of the sliding wedge gradually increases. Nevertheless, after  $a/H$  increases to a certain value, the

size of the sliding wedge does not increase any more. On the contrary, it begins to decrease with the continuing increase of  $a/H$  and maintain almost a constant value almost the same with that of the wall without surcharge acting on.

(3) The factor of safety increases with the distance of the surcharge from the wall face. However, after  $a/H$  increases to a certain value, the safety factor maintains a constant value which is about the same one with that of the wall without surcharge acting on, showing that the effect of the surcharge on the safety factor becomes small in this case.

(4) The horizontal deformation of the wall back is relatively small when the length of the surcharge is small and it gradually increases with the increase of  $b/H$ . However, after the  $b/H$  value increases to be larger than a certain value, the horizontal deformation changes very little.

(5) The effect of the length of the surcharge on the sliding surface is not significant. Besides, the safety factor of the wall gradually decreases with the increase of the length of the surcharge. However, with the increase of  $a/H$ , the influence of the length of the surcharge on the safety factor gradually becomes small and after  $a/H$  becomes larger than a certain value, the length of the surcharge will have no effect on the safety factor.

## ACKNOWLEDGEMENTS

The authors wish to express their sincere gratitude to the Key Industrial Science and Technology Project of Shaanxi Province (No. 2015GY149) and the Scientific Project funded by the Ministry of Housing and Urban-Rural Development of the People's Republic of China Council (No. 2015-K2-008).

## REFERENCES

- [1] Zigler R., Pokorny M., 2015. Fire protection of timber structures strengthened with FRP materials. Civil Engineering Journal, 4: 1-8.
- [2] Liu J., 2016. Design method of bending capacity of continuous composite slab. Civil Engineering Journal, 1: 1-9.
- [3] Leshchinsky D., 1989. On the Design of Geosynthetic-Reinforced Walls. Geotextiles and Geomembranes, 8(4): 311-323.
- [4] Wong K.S., Broms B.B., 1994. Failure Modes at model tests of a geotextile reinforced wall. Geotextiles and Geomembranes, 13(6): 475-493.
- [5] Porbaha A., Goodings D.J., 1996. Centrifuge modeling of geotextile-reinforced cohesive soil retaining walls. Journal of Geotechnical Engineering, 122(10): 840-848.
- [6] Rowe R.K., Skinner G.D., 2001. Numerical analysis of geosynthetic reinforced retaining wall constructed on a layered soil foundation. Geotextiles and Geomembranes, 19: 387-412.
- [7] Koerner R.M., Soong T.Y., 2001. Geosynthetic reinforced segmental retaining walls. Geotextiles and Geomembranes, 19(6): 359-386.

- [8] Yoo C., 2004. Performance of a 6-year-old geosynthetic-reinforced segmental retaining wall. *Geotextiles and Geomembranes*, 22(5): 377-397.
- [9] Hatami K., Bathurst R.J., 2005. Development and verification of a numerical model for the analysis of geosynthetic-reinforced soil segmental walls under working stress conditions. *Canadian Geotechnical Journal*, 42(4): 1066-1085.
- [10] Bathurst R.J., Vlachopoulos N., Waiters D.L., Burgess P.G., Allen T.M., 2006. The influence of facing stiffness on the performance of two geosynthetic reinforced soil retaining walls. *Canadian Geotechnical Journal*, 43(12): 1225-1237.
- [11] Benjamim C.V.S., Bueno B.S., Zornberg J.G., 2007. Field monitoring evaluation of geotextile-reinforced soil-retaining walls. *Geosynthetics International*, 14(2): 100-118.
- [12] Won M.S., Kim Y.S., 2007. Internal deformation behavior of geosynthetic-reinforced soil walls. *Geotextiles and Geomembranes*, 25(1): 10-22.
- [13] Sabermahani A., Ghalandarzadeh A., Falkher A., 2009. Experimental study on seismic deformation modes of reinforced-soil walls. *Geotextiles and Geomembranes*, 27(2): 121-136.
- [14] Bathurst R.J., Nernheim A., Walters D.L., Allen T.M., Burgess P., Saunders D.D., 2009. Influence of reinforcement stiffness and compaction on the performance of four geosynthetic-reinforced soil walls. *Geosynthetics International*, 16(1): 43-59.
- [15] Leshchinsky D., 2009. On global equilibrium in design of geosynthetic reinforced walls. *Journal of Geotechnical and Geoenvironmental Engineering*, 135(3): 309-315.
- [16] Ehrlich M., Mirmoradi S.H., Saramago R.P., 2012. Evaluation of the effect of compaction on the behavior of geosynthetic-reinforced soil walls. *Geotextiles and Geomembranes*, 34: 108-115.
- [17] Sksiripattanapong C., Chinkulkijniwat A., Horpibulsuk S., Rujikiatkamjorn C., Tanhsutthinon T., 2012. Numerical analysis of bearing reinforcement earth (BRE) wall. *Geotextiles and Geomembranes*, 32: 28-37.
- [18] Liu H.B., 2012. Long-term lateral displacement of geosynthetic-reinforced soil segmental retaining walls. *Geotextiles and Geomembranes*, 32: 18-27.
- [19] Xie Y.L., Yang X.H., 2009. Characteristics of a new-type geocell flexible retaining wall. *Journal of Materials in Civil Engineering*, ASCE, 21(4): 171-175.
- [20] Chen R.H., Chiu Y.M., 2008. Model tests of geocell retaining structures. *Geotextiles and Geomembranes*, 26(1): 56-70.
- [21] Song F., Xu W.Q., Zhang L.Y., Peng Y.G., 2011. Numerical analysis of deformation behavior of geocell flexible retaining wall. *Rock and Soil Mechanics*, 32(supp.1): 738-742.
- [22] Chen R.H., Wu C.P., Huang F.C., Shen C.W., 2013. Numerical analysis of geocell-reinforced retaining structures. *Geotextiles and Geomembranes*, 39: 51-62.
- [23] Song F., Xie Y.L., Yang X.H., Zhang L.Y., 2013a. Failure mode of geocell flexible retaining wall with surcharge acting on backfill surface. *Chinese Journal of Geotechnical Engineering*, 35(supp.1): 152-155.

- [24] Song F., Cao G.R., Zhang L.Y., Tan X.M., 2013b. Numerical analysis of failure mode of geocell flexible retaining Wall. ASCE Geotechnical Special Publication, 232: 136-145.
- [25] Song F., Yong L.X., Yang Y.F., Yang X.H., 2014a. Analysis of failure of flexible geocell-reinforced retaining walls in the centrifuge. Geosynthetics International, 21(6): 342-351.
- [26] Song F., Li Y. L., Zhang K., Zhang L. Y., 2014b. Study on the optimum sectional form of geocell reinforced retaining wall. // International Journal of Earth Sciences and Engineering, 7, 2, pp. 571-577.
- [27] Mhaikar S.Y., Mandal J.N., 1996. Investigations on soft clay subgrade strengthening using geocells. Construction and Building Materials, 10(4): 281-286.
- [28] Bathurst R.J., Knight M.A., 1998. Analysis of Geocell Reinforced-Soil Covers over Large Span Conduits. Computers and Geotechnics, 22(3/4): 205-219.
- [29] Latha G.M., 2000. Investigations on the Behavior of Geocell Supported Embankments. Ph.D. thesis, Indian Institute of Technology Madras, Chennai, India.
- [30] Rajagopal K., Krishnaswamy N.R., Latha G.M., 2001. Finite element analysis of mbankments supported on geocell layer using composite model. In: Desai, C.S. (Ed). Computer Methods and Advances in Geomechanics. Balkema, Rotterdam, the Netherlands, 1251-1254.
- [31] Latha G.M., Rajagopal K., Krishnaswamy IV.R. 2006. Experimental and theoretical investigations on geocell supported embankments. International Journal of Geomechanics, 6(1): 30-35.
- [32] Latha G.M., Rajagopal K., 2007. Parametric finite element analyses of geocell-supported embankment.// Canadian Geotechnical Journal, 44, 8, pp. 917-927.
- [33] Latha G.M., Dash S.K., Rajagopal K., 2008. Equivalent continuum simulations of geocell reinforced sand beds supporting strip footings. Geotechnical and Geological Engineering, 26: 387-398.
- [34] Latha G.M., Dash S.K., Rajagopal K., 2009. Numerical simulation of the behavior of geocell reinforced sand in foundations. International Journal of Geomechanics, 9(4): 143-152.
- [35] Mehdipour I., Ghazavi M., Moayed R.Z., 2013. Numerical study on stability analysis of geocell reinforced slopes by considering the bending effect. Geotextiles and Geomembranes, 37: 23-34.
- [36] Brinkgreve R.B.J., Broere W., 2000. PLAXIS 2D Version 9 Reference Manual. PLAXIS bv P.O. Box 572.2600 AN DELFT Netherlands.
- [37] Wang L.P., 2004. Simulation analysis of engineering behavior of geocell flexible retaining wall. M. Eng. Thesis, Geotechnical and Tunneling Department, School of Highway, Chang'an University, Xi'an, China.
- [38] Yang X.H., 2005. Study on engineering character and applied technique of geocell. Ph.D. Thesis, Geotechnical and Tunneling Department, School of Highway, Chang'an University, Xi'an, China.

# SEISMIC ANALYSIS OF NUCLEAR POWER PLANT CANNED MOTOR PUMP UNIT BASED ON INTEGRAL CALCULATION METHOD

Li Zhenggui<sup>1</sup>, Li Muyu<sup>1</sup>, Zhang Jiarong<sup>1</sup>, Li Bo<sup>1</sup>, Liu Xiaobing<sup>1</sup>, Yang Fengyu<sup>1,2</sup>

1 Key Laboratory of Fluid and Power Machinery, Ministry of Education, Xihua University, Chengdu, 610039, China; lzhgui@126.com

2 Institute of Energy and Power Engineering, Lanzhou University of Technology, Lanzhou 730050, China

## ABSTRACT

The canned motor pump is a device in one of the most important loops in the nuclear power plant system and key technology research project, of which the seismic requirements shall be checked by Category A. It is required that the structural integrity and electric drive assembly performability of the unit can be ensured during or after operating basic earthquake (OBE) or safe shutdown earthquake (SSE). The author uses Ansys software workbench module to carry out appearance-based three-dimensional modeling, finite element meshing, intrinsic mode analysis, and carry out structural overall element analysis and calculation considering dead weight load and earthquake spectrum load. The results show that the unit major structure rotary and static parts, gear system, bearing parts, bolt and screw strengths meet the requirements and the structure maintains integrity, the relative deformation of the unit rotary and static parts shall be less than the specified value of gap among them, so as to keep the performability and not interfere with the operation. The appearance-based seismic analysis method not only can ensure the calculation accuracy, but also can greatly reduce the workload in calculation and checking, has a certain learning value.

## KEYWORDS

Nuclear power plant, Canned motor pump, Ansys integral calculation, Earthquake spectrum analysis

## 1. INTRODUCTION

The canned motor pump is a device in one of the most important circuit in ACP100+ nuclear power plant system and key technology research project and a valve turning speed governing fully enclosed actuator (hereinafter referred as Canned Motor Pump Drive Assembly). The seismic category shall be considered as 1A, if the performance is ineligible, the unit vibration swing may exceed the allowable value, which will result in high dynamic stress on rotary parts and support system, collision and friction among rotors and stators may occur, which will result in wear and damage, and thus do great harm to the system safe and reliable operation and even lead to accidents in the nuclear power plant. It is required that the structural integrity and electric drive assembly performability of the unit can be ensured during or after operating basic earthquake (OBE) or safe shutdown earthquake (SSE). In recent years, in seismic aspects the researches of

scholars at home and abroad mainly focus on nuclear power plant building and equipment static performance[1~3], there are fewer literatures relating to the pump equipments[4~6], and the classical equipment seismic calculation methods mainly include equivalent static method, time history analysis method and response spectrum method. The response spectrum method, which features simple calculation principle, mature theory and considered dynamic characteristics of structure, can determine the structure dynamic response to random load. With sufficient parameters of vibration mode, based on integral analysis, in this article the response spectrum method is applied for seismic calculation of ACP 100+ nuclear power plant system canned motor pump drive assembly.

## 2. SEISMIC REQUIREMENTS AND MODELS

### 2.1 Operating characteristics

The canned motor pump drive assembly impellers rotate synchronously with the motor. The structure of canned motor pump drive device is shown in *Figure 1*. The assembly mainly consists of pump main parts (static) (14 and 18), pump main parts (rotary) (13), gear system (24,27 and 30), bearing parts(15,30 and 31) and bolts (21). The basic design parameters are shown in *Table 1*. The material mechanical properties of various parts are shown in *Table 2*. Under earthquake and other load cases, it is required that the major structure static and rotary parts, bearing system, bearing parts, bolt and screw strengths meet the requirements and the structure maintain integrity; the relative deformation among the rotary parts and static parts of the assembly shall be less than the specified value of the gap among them and the performability maintains.

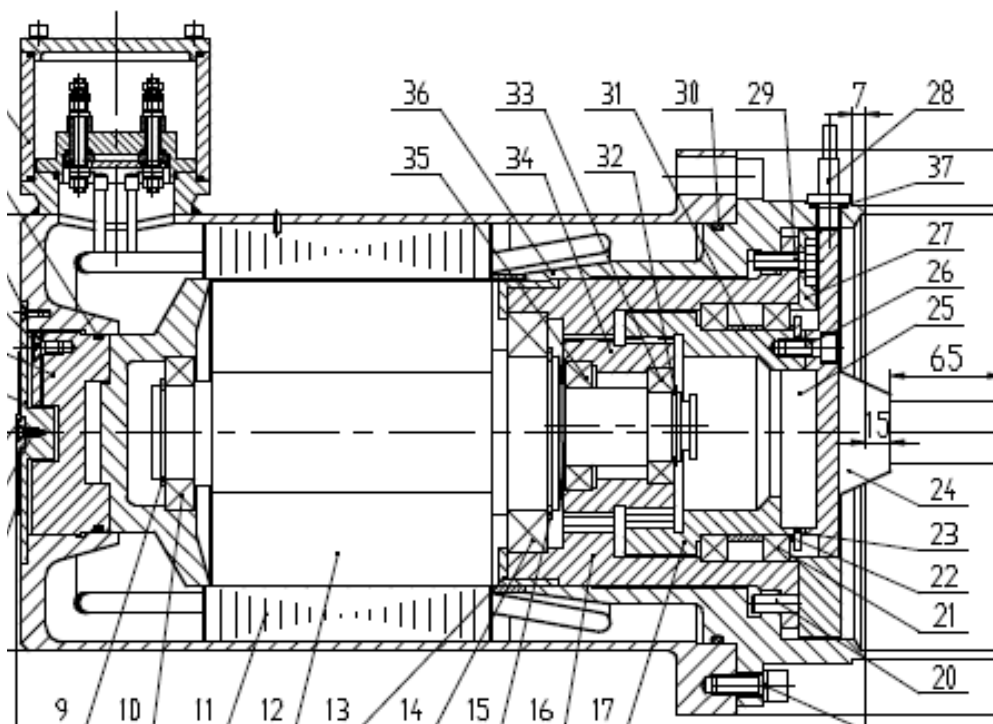


Figure 1 - Canned Motor Pump Drive Assembly Structure

*Table 1 - Assembly Ratings*

Rated Power (kw)	Rated Speed (r/min)	Air gap (mm)	Allowable air-gap offset (%)
300	1480	1	10%

*Table 2 - Material Mechanical Properties of Various Parts*

Name	Material and Modulus of Elasticity E /N•m-2	Poisson's Ratio $\mu$	Yield Stress $\sigma_s$ /MPa	Tensile Strength $\sigma_b$ /MPa	Allowable Stress Sm/MPa	Allowable Stress under Seismic Condition Si/MPa
Pump Main Parts (static)	$2.06 \times 10^{11}$	0.27	460	980	245	368
Pump Main Parts (rotary)	$2.06 \times 10^{11}$	0.24	510	500	125	188
Gear system	$2.06 \times 10^{11}$	0.26	235	417	123	125
Bearing Part	$2.06 \times 10^{11}$	0.26	345	490	125	185
Bolt	$2.06 \times 10^{11}$	0.27	460	980	245	368

## 2.2 Structural model

The canned motor pump drive assembly is applied with solid element, beam element, quality element and spring element to build the model under unified consideration that the assembly composed by pump main parts (static), pump main parts (rotary), gear system, bearing parts, bolts and etc. In the calculation model, the pump main parts (rotary) are described by beam element, the total weight of the rotors and other parts are evenly put on the length of corresponding axis of various parts. The pump main parts (static) are described by 8-node Solid 45 element. The axial vents and other gaps of the stator yoke are just considered as simple mass decrement [7]. The support bearing of the canned motor pump drive assembly is applied with multi-point constraint method and is a simply-support structure, the fastener bolts and other parts are connected rigidly. The finite element model of the whole structure includes 3838 solid elements, 36 beam element, 24 quality elements, 64 spring elements, 5036 elements and 6756 nodes in all. The finite element model refers to Fig 2.

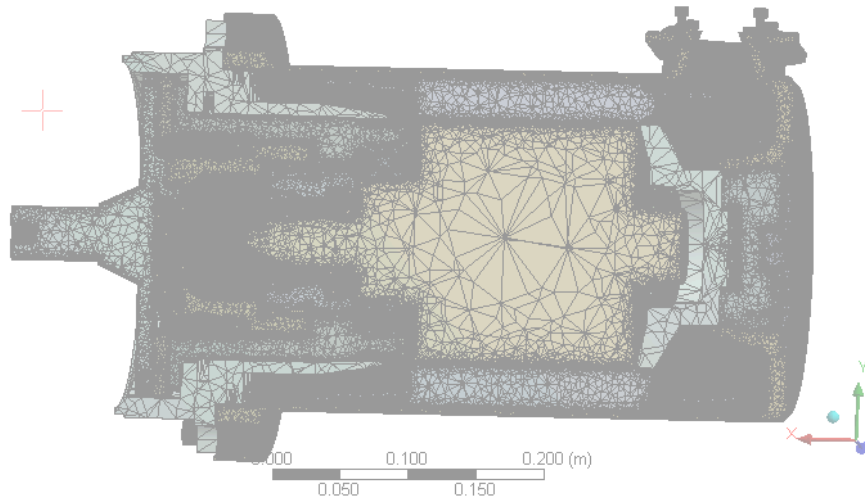


Figure 2 - Finite Element Mesh Model

### 3. THEORETICAL EQUATION

Through response spectrum concept, the response spectrum method not only considers the relationship between structure dynamic characteristics and seismic dynamic characteristics, but also makes full use of the static theory, skillfully staticizes the dynamic problem, makes the complicated earthquake action on structure and its effect calculation easy and simple [8-10]. Under seismic load, multi-freedom motion matrix equation [11-13] is:

$$\overset{\bullet\bullet}{M} \overset{\bullet\bullet}{x} + \overset{\bullet\bullet}{C} \overset{\bullet\bullet}{x} + \overset{\bullet\bullet}{K} \overset{\bullet\bullet}{x} = \overset{\bullet\bullet}{M} \overset{\bullet\bullet}{x}_g \quad (1)$$

Where, M refers to the structure mass matrix, C refers to the structure damping matrix, K refers to the structure rigidity matrix and x refers to the displacement vector.

The modal analysis is the basis of response spectrum method and dynamic transient and impact analysis and mainly solves the structure frequency and vibration mode. In dynamical property analysis without regard to damping, the free vibration master equation is:

$$\overset{\bullet\bullet}{M} \overset{\bullet\bullet}{x} + \overset{\bullet\bullet}{K} \overset{\bullet\bullet}{x} = 0 \quad (2)$$

In modal analysis, the characteristic value represents the square of structure natural frequency (without regard to damp effect), the characteristic vector represents the vibration mode corresponding to that natural frequency .

The modal analysis simplifies the multi-degree-of-freedom system earthquake response into an independent single-degree-of-freedom system earthquake response for calculation. In case of horizontal earthquake, the horizontal earthquake action standard value at Particle i, Vibration Mode j in multi-degree-of-freedom system is:

$$F_{ij} = \alpha_j \gamma_j X_i G_i, \quad i,j=1,2,\dots,n \quad (3)$$

Where,  $F_{ij}$  refers to the horizontal earthquake action standard value,  $\alpha_j$  refers to the earthquake influence coefficient;  $\gamma_j$  refers to the vibration mode participation coefficient;  $X_i$  refers to the horizontal relative displacement;  $G_i$  refers to the representative value of gravity load focusing on Particle i.

All of the earthquake actions of various vibration modes determined by the response spectrum method is the maximum value, while they do not always occur at the same time and moreover is not necessarily in same direction. Therefore, when solving the total effect  $S$  of earthquake actions, as the max absolute value is taken from various time-history responses during spectrum curve making, a larger result will be attained by simply adding the  $S_j$ . For this reason, the modalities are required to be combined. Considering the probability, the seismic code uses the method of Square Root of Sum of Squares (SRSS), calculates the structure earthquake action effect  $S_j$  according to the earthquake action standard value  $F_{ij}$  of multi-degree-of-freedom system Vibration Mode  $j$  Particle  $i$ , then it calculates the square root and square of  $S_j$  at the same position of various vibration modes as well as the total seismic effects of that position, i.e.

$$S = \sqrt{\sum_{j=1}^n S_j^2} \tag{4}$$

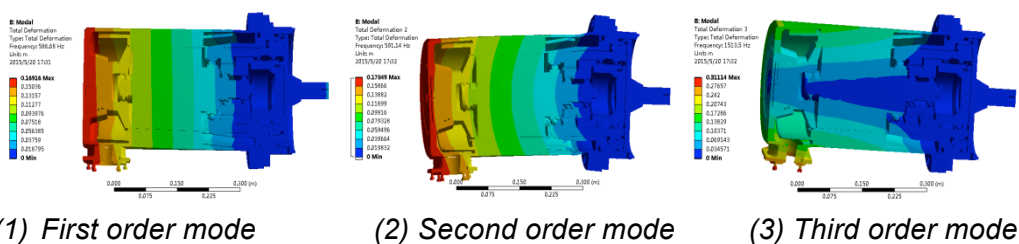
Where:  $S$  refers to the total seismic effect,  $S_j$  refers to the effect of action caused by Type  $j$  horizontal earthquake. In this article modal combination is applied with SRSS method and in the meanwhile the high order mode of which the seismic response is not more than 10% is neglected.

#### 4. MODAL ANALYSIS

With modal calculation for the canned motor pump drive assembly and assembly basic structure mechanical property analysis, this has calculated the electric drive assembly overall 9-order mode. As seen in vibration mode Fig 3, the first two orders of the vibration mode of different parts of that electric drive assembly are the vibration mode of spindle. During modal analysis, the constraints are set single as possible as it can be, therefore the above modal calculation result is relatively conservative, the third and fourth order of the vibration mode is in Y and Z direction, from the fifth to ninth order the vibration is in X direction. Table 3 shows: the first order natural frequency of various parts is greatly higher than 33Hz. In accordance with nuclear safety code HAF0215, methods including equivalent static method can be applied for assembly seismic analysis.

Table 3 - Integral natural frequency (Unit: Hz)

Order	1	2	3	4	5	6	7	8	9
Natural Frequency	586.68	591.14	1513.5	1619.7	2033.6	2064.2	2999.2	3097.6	3101.6



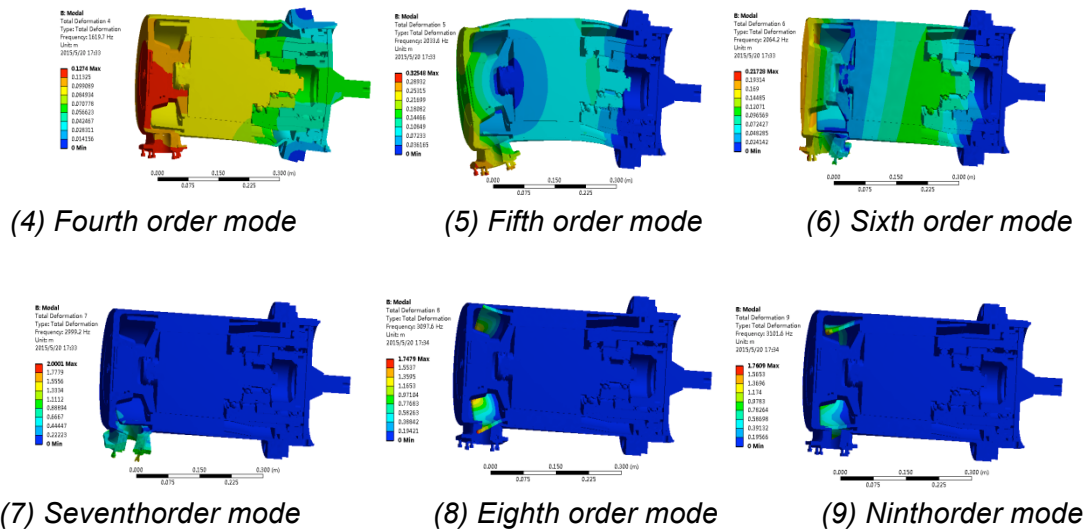


Fig 3 Electric Drive Assembly Integral Mode

## 5 CALCULATION AND ANALYSIS

### 5.1 Load and constraint

This calculation mainly considers the dead weight and earthquake response spectrum load and in the meanwhile rationally considers the resistance ratio. The dead weight load actually is a kind of mass force, including the assembly weight and medium weight, all loads act on the unit of every part of the canned motor pump drive assembly and belong to static load. *Table 4* is the response spectrum in horizontal direction (elevation:0.0m) and *Table 5* is the response spectrum in vertical direction (elevation:0.0m). As shown in *Table 6*, the main factors having influences on the resistance ratio during vibration are structure vibration mode, material characteristics, strain and vibration frequency. When defining the earthquake response spectrum, in nuclear power equipment codes of various countries different items are come up with quantitative damping ratio. This article applies a damping ratio of conservative 2%.

Table 4 - Response Spectrum in Horizontal Direction (Elevation: 0.0m)

Frequency(Hz)	Acceleration (g)				
	2%	4%	5%	7%	10%
0.2	0.04	0.04	0.03	0.03	0.03
2.50	0.47	0.36	0.31	0.28	0.25
3.50	0.47	0.37	0.34	0.31	0.27
5.58	1.02	0.70	0.62	0.51	0.43
7.80	1.02	0.70	0.62	0.51	0.43
9.14	0.85	0.59	0.50	0.41	
11.50	0.35	0.29	0.27	0.25	0.24
21.50	0.35	0.29	0.27	0.25	0.24
27.00	0.20	0.18	0.18	0.18	0.18
40.00	0.16	0.16	0.16	0.16	0.16
100.00	0.16	0.16	0.16	0.16	0.16

Table 5 - Response Spectrum in Vertical Direction (elevation: 0.0m)

Frequency(Hz)	Acceleration (g)				
	2%	4%	5%	7%	10%
0.2	0.03	0.028	0.03	0.025	0.023
2.30	0.33	0.24	0.22	0.18	0.16
8.25				0.21	0.19
13.1	0.38	0.26	0.24		
17.5					0.16
17.6	0.38	0.26	0.23	0.19	
20.0	0.15	0.14	0.14	0.14	0.14
31.50	0.092	0.092	0.092	0.092	0.092
100.00	0.092	0.092	0.092	0.092	0.092

Table 6 - Typical Item Damping Ratio

Item	Damping Ratio	
	%	
	SSE	OBE
Welding Structure	4	3
Bolted Structure	7	5
Equipment, main Condenser Circulating System, parts	3	2
Pipeline System	4	3

Considering OBE and SSE standards, the calculation shall be relatively conservative, the three accelerations of the earthquake spectrum (2 mutually perpendicular horizontal accelerations and 1 vertical acceleration), i.e. for components in x, y and z three directions determine the acceleration by the earthquake response spectrum, then multiply a coefficient of 1.5. As shown in Table 7, when the load is SL-2 (limiting safety seismic motion), make 6g in the three directions simultaneously; under SL-1 (operating basis seismic motion), apply 4.8g specification requirement in three direction simultaneously, for gravity load, in a direction vertically downward, with the acceleration as 1g and g representing the acceleration of gravity =9.8m/s<sup>2</sup>.

Table 7 - Part calculation constrains and load conditions

No	Name	Constrains	Load
1	Pump Main Parts (static)	Impose constraints on end and no	4.8g、6g Seismic load, self-weight load
2	Pump Main Parts (rotary)	constraints on rotation, thus the	4.8g、6g Seismic load, self-weight load
3	Fixation System	results are	4.8g、6g Seismic load, self-weight load
4	Bearing Parts	conservative	4.8g、6g Seismic load, self-weight load
5	Bolt		4.8g、6g Seismic load, self-weight load

### 5.2 Load combinations and boundary conditions

The canned pump overall seismic analysis considers two kinds of load cases separately: (1) the loads under safe operation condition (Class B) are: dead weight+ torque+ OBE; (2) the loads under accident condition (Class C) are: dead weight+ torque +SSE. The operating conditions and stress criteria applied in the calculation are shown in *Table 4*. The material properties and acceleration of gravity given in the self-weight load will be calculated by the software itself, in a direction of vertically downward; the torque will be respectively applied at the both ends of the spindle in the opposite direction. Respectively calculate the seismic load in three directions for OBE and SSE load, combine by square root of sum of squares method, at last combine with the stress caused by other loads. *Table 8* shows the stress limits under different loads.

*Table 8 - Stress Limit under Different Load*

Operating Condition	Load Combination	Stress Limit
Class B	Dead Weight, Torque, OBE seismic load	$\sigma_m \leq 1.1S$
		$\sigma_m (\text{or } \sigma_L) \sigma_b + \leq 1.65S$
Class C	Dead Weight, Torque, OBE seismic load	$\sigma_m \leq 1.5S$
		$\sigma_m (\text{or } \sigma_L) \sigma_b + \leq 1.80S$

Under seismic load, calculate the earthquake response spectrum, with an elevation of 0.0m, a damping ratio of 2% and 6 times of load. *Figure 4* is the earthquake response spectrum input curves.

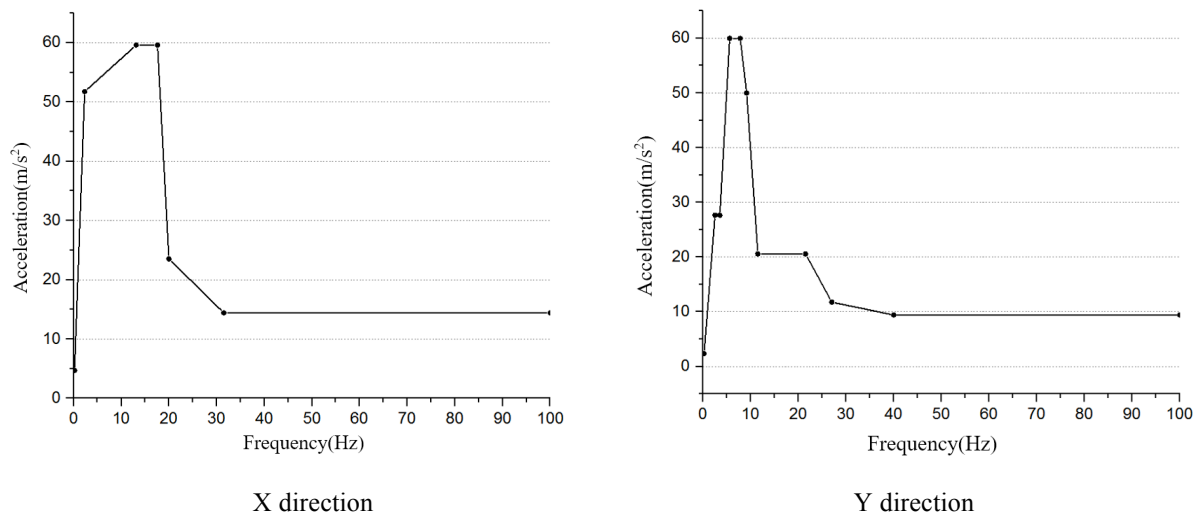


*Figure 4 - Earthquake Response Spectrum Input Curve*

## 6. RESULT AND SEISMIC PERFORMANCE ANALYSIS

### 6.1 Integrity analysis:

Under seismic load, with overall analysis, the calculations show that the max stress appears on the corresponding roller in the middle of the stator shield (in very small areas and cannot see it clearly), as 1.8MPa, mainly induced by large deformation in the middle of the stator shield; in case of much less than the allowable stress (roller main material tensile strength is 560MPa and the min allowable stress is 373MPa), it is as *Figure 5*. For max value refers to *Table 9*.

*Table 9 - Integral Earthquake Response Spectrum Equivalent Stress Analysis (Max)*

Equivalent Stress (Pa)	Equivalent strain (m/m)
1.8473e6	1.0429e-5

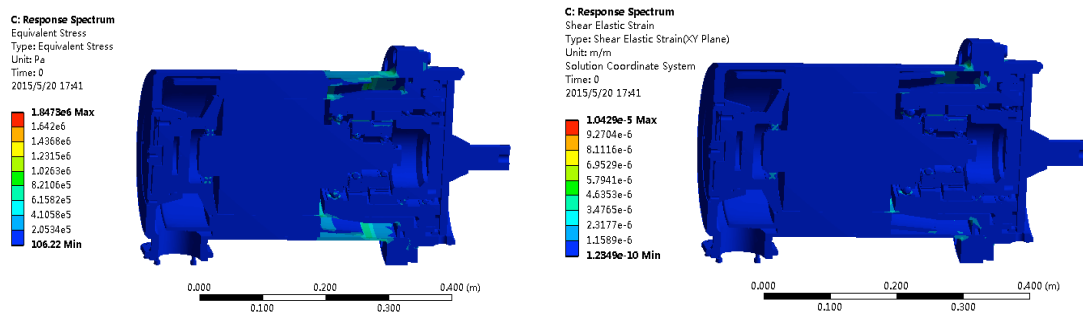


*Figure 5 - Integral Earthquake Response Spectrum Stress*

### 6.2 Performability analysis

During an earthquake response spectrum calculation, the integral deformation in rear cover position is larger, in the middle is smaller, in the output end is minimum and even, the value in X direction is relatively smaller, the deformation is relatively even, the value in Y and Z direction is smaller and increases locally, the max deformation in X direction is 5.5267e-7, 1.007e-6 in Y direction and 1.0789e-6 in Z direction, all of which are relatively smaller, **it has** no influences on the electric drive assembly performability. The distribution is shown in Fig 6 and the max deformation value is shown in *Table 11*.

*Table 11 - Integral Earthquake Response Spectrum Deformation Analysis (Max)*

Deformation in X direction (m)	Deformation in Y direction (m)	Deformation in Z direction (m)
5.5267e-7	1.007e-6	1.0789e-6

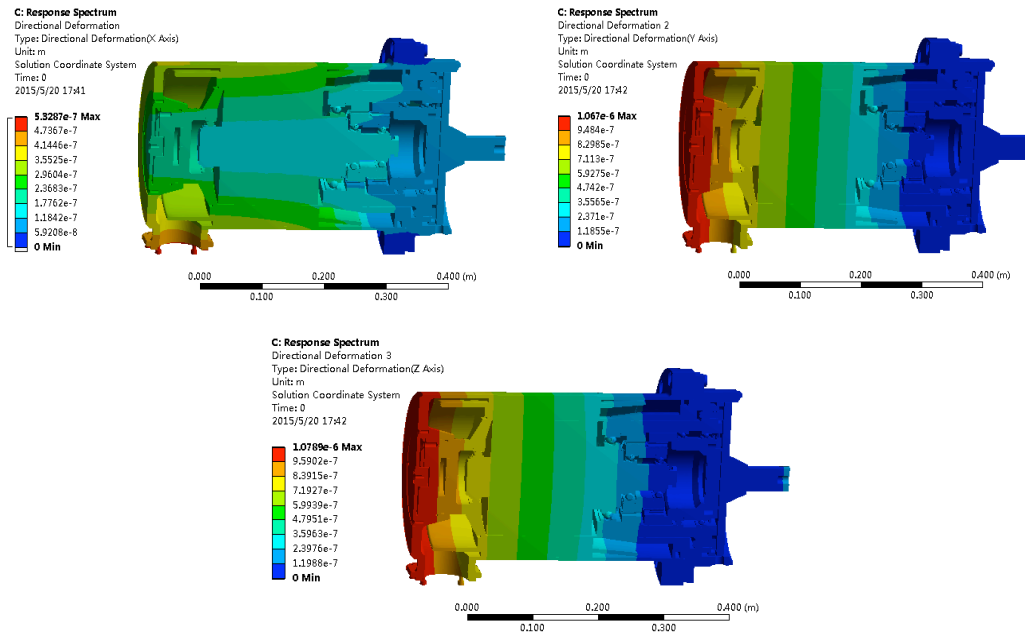


Figure 6 - Integral Earthquake Response Spectrum Deformation

### 6.3 Evaluation and conclusion

In accordance with nuclear power plant evaluation system, as shown in *Table 12*, based on integral calculation, the max calculated stress of the part is much less than the value required in evaluation criterion and qualified in the check. The seismic analysis of the canned pump requires that under the interaction of SSE seismic load, dead weight and other loads, the performance shall be maintained, the relative deformation between the rotor and stator shall be less than the gap between them, so as not to interfere with operation. Due to the strong integral structure rigidity, the absolute displacement of various parts is very small, the max displacement is in the upper cover position of the canned pump, with a value of 0.007mm. The displacement of the canned pump shaft is 0.006mm, mainly are rigid body displacement, the relative deformation between the stator and rotor of the canned pump is 0.007mm, less than 10% of the air gap, as shown in *Table 13*.

Table 12 Equipment Integrity Check

Position	Analysis Method	Load	Calculated Stress (MPa)	Evaluation Criterion (MPa)	Evaluation Result
Integral	Response Spectrum	4.8g Seismic Load	1.23	<347	Pass
		6g Seismic Load	1.84	<347	Pass

Table 13 - Integral Performability Evaluation Motor Designed Air Gap 1mm

Position	Analysis Method	Load	Deformation (%)	Evaluation Criterion	Evaluation Result
Integral	Response Spectrum	6g	Self-weight	X direction <1%	< Designed
		Seismic	Load	Y direction <0.5%	Air Gap
		Load	Load	Z direction <0.5%	10%

Based on canned motor pump drive assembly integral analysis method, this article applies with response spectrum method for seismic calculation of ACP100+ nuclear power plant system canned motor pump drive assembly and draws the following conclusions, under self-weight and seismic load: the parts of the electric drive assembly (main part rotary and static parts, drive gear assembly, bearing and fasteners) meet the RCC-M requirements and can ensure that the integrity of the structure is maintained under safe shutdown earthquake. The deformation of assembly stator and rotor system and gear drive system under seismic load is less than the min operating air gap and meet the performability. The GB50267 Code for Seismic Design of Nuclear Power Plants, HAF102-2004 Regulation on Safety for Nuclear Power Plants Design and HAF103-2004 Regulation on Safety for Nuclear Power Plant Operation is met, the result accuracy is ensured and calculation work amount is greatly reduced. The results of this paper have a certain reference significance for seismic analysis of nuclear power plant canned motor pump unit.

## ACKNOWLEDGMENT

The authors would like to thank Xihua University Natural fund (Z1510416) for their financial support, National Science Foundation (51279172).

## REFERENCES

- [1] Birkhofer A., 1997. Seismic Design of Nuclear Facilities in Germany. Nuclear Engineering and Design, vol.172: 247-260.
- [2] Zhang Zheng-ming, He Shu-yan, Xu Ming, 2007. Seismic Analysis of Liquid Storage Container in Nuclear Reactors. Nuclear Engineering and Design, Vol. 237: 1325-1331.
- [3] LI Shui-an, 2002. Calculation of anti-seismic design for Xi'an pulsed reactor. Nuclear Power Engineering, Vol. 23(6): 12-15.
- [4] SHENG Xuanyu, LUO Xiaowei, FU Jiyang, 2005. Aseismic strength analysis of main nuclear reactor pump based on real three dimension model. Nuclear Power Engineering, Vol. 26(5): 471-474.
- [5] Hu Shaoqing, Sun Baitao, 2006. Seismic analysis for three phase asynchronous motor used in nuclear power generating station. Earthquake Engineering And Engineering Vibration, Vol. 26(6):133-137.
- [6] Victor V Kostarev, Andrei V etrenko, Peter S Vasilyev, 2007. An advanced Seismic Analysis of an NPP Powerful Turbogenerator on an Isolation Pedestal. Nuclear Engineering and Design, Vol. 237: 1315-1324.
- [7] YANG Xiao-feng, ZHANG Yong, SUN Bai-tao, HU Shao-qing, 2007 Seismic analysis on canned

---

motor pump used in nuclear power generating station. World Earthquake Engineering, Vol, 23(3):47-5

- [8] XIAO Yan-wu, 2010. Limitations and Recent Improvements of Earthquake Response Spectrum. Journal of Water Resources and Architectural Engineering, Vol.(6) 56-58.
- [9] YANG Pu, LI Yingmin, LAI Ming, 2000. A new Method for selecting inputting waves for time-history analysis. China civil Engineering Journal, Vol. (6):33-37.
- [10] Zhang Xiaozhi, Xie Lili, Yu Haiying, 2004. Precision problems in calculating response spectra by using numerical method, (6):15-20
- [11] FU Qiang, YUAN Shou-qi, ZHU Rong-sheng, OU Ming-xiong, YANG Ai-ling, 2010. Seismic Analysis for SEC Drum-Shaped Filter of 1000 MW Nuclear Power Plant. Nuclear Power Engineering, Vol.31(6):10-14
- [12] Wanda I C, Russell A G, 2007. Damping correction factors for horizontal ground-motion response spectra Bulletin of the Seismological Society of America, Vol. 97(3):934-960.
- [13] Newmark N W, Hall W J., 1982. Earthquake spectra and design. Oakland: Earthquake Engineering Research Institute, 29-47.

## COMPLEX ANALYSIS AND DOCUMENTATION OF HISTORICAL BUILDINGS USING NEW GEOMATICS METHODS

*M. Falýnová<sup>1</sup>, P. Raeva<sup>1</sup>, Z. Poloprutský<sup>1</sup>, E. Matoušková<sup>1</sup>, E. Housarová<sup>1</sup>*

1. *Czech Technical University In Prague, Faculty of Civil Engineering, Department of Geomatics, Praha 6, Thákurova 7, 166 29, Czech Republic; [faltynova@gmail.com](mailto:faltynova@gmail.com)*

### ABSTRACT

Documentation of a historical building is very important process preceding to every restoration or reconstruction work. It helps to preserve even minor information about objects shape, state, position and is often used for work advancement planning. Documentation is usually done using precise 3D model creation from which demanded cuts like ground plan are created.

This papers shows how new geomatics methods can be used for 3D model creation and its placement in the area, that can be very interesting in terms of north-south position. As a case study two historical churches located in Czech Republic (towns of Holubice and Kralovice) has been used. Photogrammetry and laser scanning methods for 3D model creation are introduced.

### KEYWORDS

Historical building analysis, Geomatics, 3D modelling, Photogrammetry, Laser scanning, Reflectance spectroscopy, Church, Kralovice, Holubice

### INTRODUCTION

Documentation of cultural heritage objects is very important issue and 3D modelling and other non-invasive methods provide an excellent tool in order to study and preserve historical buildings. Photogrammetry and laser scanning are two methods that are recently very popular for 3D model creation since they provide fine information about the object shape and when supplemented with classical geodetic survey objects global position in desired coordinate system can be determined. Photogrammetric methods use photographs taken from various locations around object of interest with high overlap (min 60%) to derive the point cloud. Special software based on image based modelling methods [1] is applied. Laser scanning is a non contact mass measurement of 3D points, it uses a special active device that transmits high numbers of laser beams that are reflected by the object. Using distances and angles of these reflections a 3D model is created [2]. Comparison and more information regarding mentioned methods in cultural heritage documentation field can be found in following papers [3], [4], [5], [6].

Non-invasive documentation is highly demanded method for analysis of historical objects. It provides specific information without the need to touch and therefore to harm or even damage the object of interest. Besides the two formerly mentioned methods, there are others such as reflectance spectroscopy and GPR. Reflectance spectroscopy is a technology based on spectral analysis of a specific material can provide information of the object chemical composition. Testing of this method on historical plasters can be found in [7]. Sometimes there is a need to analyse objects that are hidden under surface and Ground Penetrating Radar (GPR) is a great tool for that. The GPR uses electromagnetic radiation in the microwave band of the radio spectrum and analyses signals reflected from the subsurface structures. The antenna transmitter emits impulses of sine wave that travels through the material until it begins to reflect back to the antenna receiver by boundaries between the layers or the objects with different dielectric characteristics. The velocity of the radiation depends on the electromagnetic characteristics surveyed material [8].

## PHOTOGRAMMETRY

Romanesque Nativity of Mary sexton has been chosen as a test site for photogrammetric 3D model creation. The sexton has been found by Ottokar I. of Bohemia and its origin is dated back to years 1124 – 1125 as it was mentioned in the seal of the Pelhřim bishop, that was found in 1865 when the old altar had been replaced. The sexton's core is a circular rotunda with semicircle apsis made from ashlar. The tower, second apsis and the north sacristy are later annexes; tower's wooden superstructure has been added at the end of 17<sup>th</sup> century. The sexton is surrounded by high load-bearing walls from three sites and by former cemetery. Well preserved original Romanesque and early gothic frescoes can be found inside the sexton.



*Figure 1 – Holubice Nativity of Mary sexton  
West view*

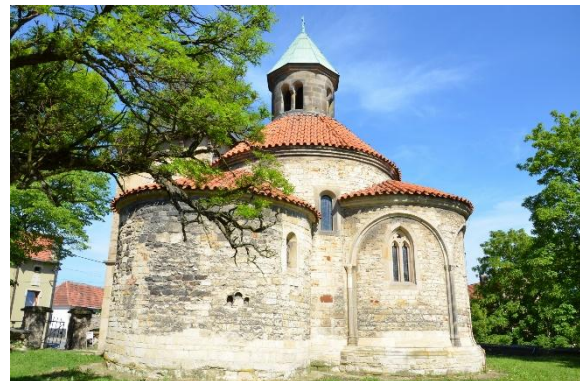


*Figure 2 - Holubice Nativity of Mary sexton  
South view*



*Figure 3 – Holubice – Photogrammetry derived point cloud section, North view*



*Figure 4 – Holubice – Longitudinal vertical section, North view*



*Figure 5 – Holubice – Ground plan point cloud section, Top view*

Interior and exterior structural objects has been documented for the purpose of complex photogrammetric survey [9]. Local surveying network has been created and used as a spatial framework for detailed measurements. The survey has been connected to the national height coordination system (Baltic Vertical Datum – After Adjustment - Bpv). Polar survey has been used as a main mapping method. Together with detailed measurements, a photogrammetric photo

documentation has been acquired. Photographs has been used for further processing in the Agisoft Photoscan software. Reference points have been chosen manually from the detail survey database. Processing parameters are listed below.

## Processing parameters

### **General**

Cameras	474
Aligned cameras	470
Markers	185
Coordinate system:	Local Coordinates (m)
Camera model:	Nikon D7000

### **Model**

Faces	22,331,560
Vertices	11,186,366
Texture	4,096 x 4,096, uint8

### **Point Cloud**

Points	118,697 of 731,814
RMS reprojection error	0.19196 (0.688 pix)
Max reprojection error	0.740856 (13.747 pix)
Mean key point size	3.476 pix
Effective overlap	4.492

### **Ground Control Points**

Count	181
X error (cm)	2.38
Y error (cm)	2.49
Z error (cm)	2.33
XY error (cm)	3.44

### **Dense Point Cloud**

Points	105,393,931
--------	-------------

Total (cm)	4.16
Image (pix)	4.85

When taken into account the jaggedness of the object the created point cloud can be a fine tool for horizontal and vertical section creation. Several "holes" can be found in the pointcloud are due to an unfavourable scanning configuration since only terrestrial photography have been performed. This issue can be solved by using an RPAS or a high crane to obtain photographs from the missing angles. Besides these defects the pointcloud and its outputs are suitable for future building archaeology survey [10] and provides sufficient information for research work.

## LASER SCANNING

As a test site for laser scanning a St. Peter and Paul Church in the town of Kralovice was chosen. This Renaissance fortified church was build according plans of Boniface the Wolmut. It belongs to the group of Florian Griesbecks properties, a highly educated Tyrolean aristocrat, private secretary and close adviser to Emperor Ferdinand I. It should be noted that at this place pre-existed gothic church which Florian Griesbeck rebuilt from 1575 to 1581. Parts of the remaining gothic walls were enclosed inside the walls done during Griesbecks reconstruction phase, so their exact structure and geometry cannot be ascertained. Interesting features are the arches on the outer side of the two longitudinal sides of the building and their fairly large thickness.

The main question was to confirm the hypothesis that its orientation seems to follow the cardinal points.

**Measurements:**

Interior and exterior of the church was documented by terrestrial laser scanning technology (Surphaser 25HSX) with special accent on orientation of walls. Walls were recorded approximately up to 4m high above terrain. Scans were acquired from 16 different scan stations using tripod (12 exterior and 4 interior). The position of each scan station was chosen with respect to conditions on site to ensure sufficient overlay of neighboring scans. The density of scanning was set to 1cm in distance of 5m.

Additional measurements were taken to ensure georeferencing of generated model. Coordinates of four points in immediate surrounding were acquired by RTK method using GNSS receiver. The receiver immediately transform the coordinates from global coordinate system to S-JTSK (Datum of Uniform Trigonometric Cadastral Network - local positioning system) and Bpv (Baltic Vertical Datum – After Adjustment) using global transformation key. These points serve as a base - selected points on surveyed object were determined by the method of intersection from distances (measured by survey tape) from the points determined by GNSS receiver.

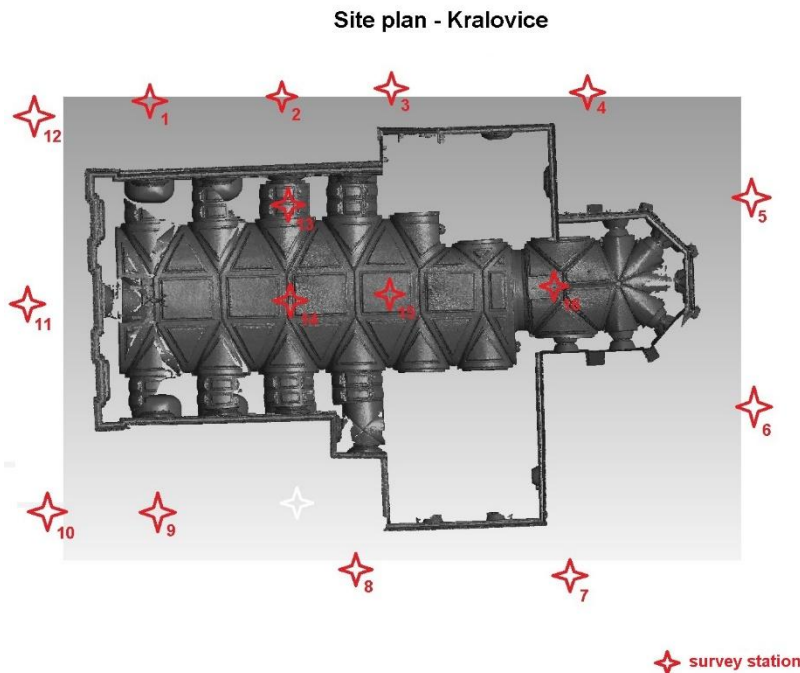


Figure 6 – Kralovice Site Plan

**Data processing**

The processing of point clouds was done using Geomagic Studio software. Each point cloud was cleaned using manual and semiautomatic selection tools. Point clouds registration (transformation into one common coordinate reference frame) followed. This step is divided into two parts: manual and global registration. The first – manual – is an approximate registration using

manually selected identical points and the second – global – is a precise automatic registration using ICP (Iterative Closest Point) algorithm.

Afterwards, the dual coordinates of identical points (one set derived from point cloud and other derived using GNSS receiver) serve for computation of transformation parameters (congruent transformation consisting of translation and rotation was used). The rotation parameter was used to adjust the orientation of the model according S-JTSK axes. However, the axes of S-JTSK are not parallel to axes of geographic coordinate system and that is why the orientation of the model was adjusted again using the value of meridian convergence (angle between cartographical projection of the meridian and parallel to the X-axis). The orientation of resulting model corresponds to the orientation in geographic coordinate system (WGS84).

Finally, the resulting point cloud was used to create polygonal model in the form of TIN (Triangulated Irregular Network). The final outcome serves as a base for cross-section and ground plan production. Cross-sections were exported for further editing using CAD software.

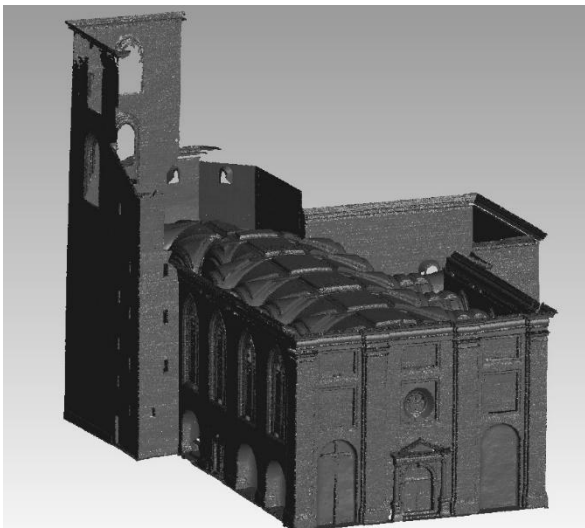


Figure 7 - North-west view

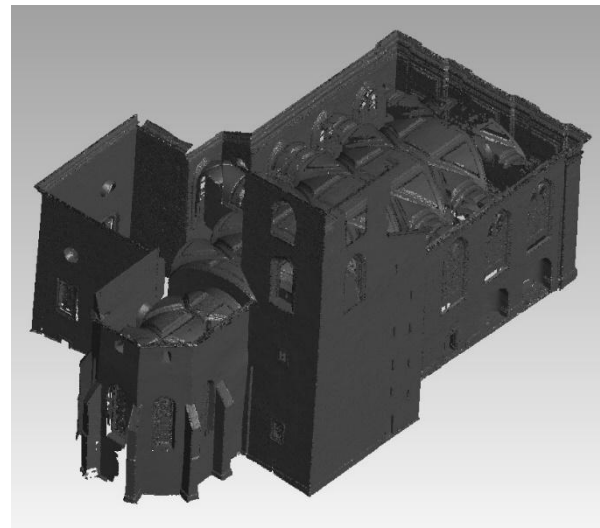


Figure 8 – North-east view

## Outputs

Main output of the survey is a detailed model of the church in form of dense point cloud. This model is oriented to geographic coordination system. Other outputs are: wall projections, ground plan and cross-sections. Expected accuracy of model orientation based on used methods is  $\pm 0,2$ gon.

The angle between the longitudinal axis of the church and the true north is 88 degrees 11 minutes that confirms the fact that its orientation follows the cardinal astronomic points – facing east. The aim of the designer was to face the sacristy to the place where sun rises on equinox days. The deviation (1.89deg) was probably created when building the church. It has been found that younger Renaissance structures follows the geometry of former gothic walls since no difference in their thickness or other parameters has been discovered on the model geometry.



Figure 9 – Model East projection



Figure 10 – Model North projection

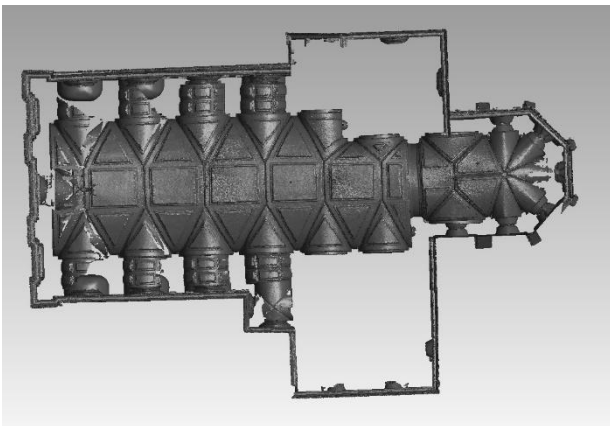


Figure 11 – Model top projection

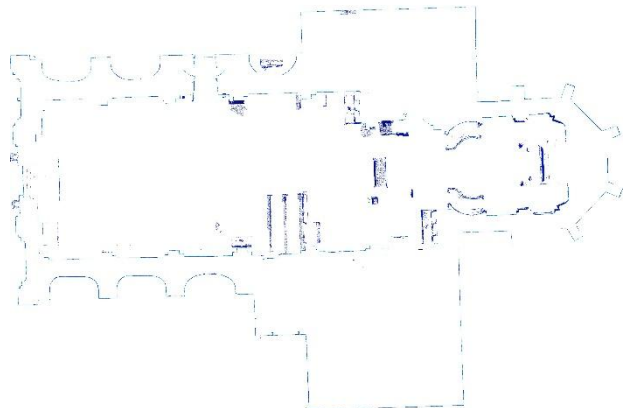


Figure 12 - Gound plan derived from the model

## CONCLUSION

A 3D model of a historical building can provide unique information regarding the objects structure, shape and position. Two 3D modelling methods were tested (photogrammetry and laser scanning) on churches in the Czech Republic. Created 3D model affords creating views from various perspective or cross sections with high accuracy suitable for precise analysis. These designs together with the 3D model itself can be exported to CAD software for further investigation.

Presented methods provide results describing the size and shape of documented objects, but they are limited to surface recognition. When there is need of inner structure quality assessment of the building, it is appropriate to complement the survey by other non-invasive methods (e.g. GPR).

## ACKNOWLEDGEMENTS

This research has been created under the Czech Ministry of Culture Project "New methods of non-invasive cultural heritage documentation" (DF13P01OVV002). More information regarding this project can be found at the project website <http://lfgm.fsv.cvut.cz/naki/index.html>.

## REFERENCES

- [1] Remondino, Fabio, and Sabry El-Hakim. "Image-based 3D modelling: a review." *The Photogrammetric Record* 21.115 (2006): 269-291.
- [2] Pfeifer, N.; Briese, Ch., 2007. *Laser scanning – principles and applications*. [http://publik.tuwien.ac.at/files/pub-geo\\_1951.pdf](http://publik.tuwien.ac.at/files/pub-geo_1951.pdf)
- [3] Remondino, F.; Campana, S., 2014. *3D Recording and Modelling in Archaeology and Cultural Heritage: Theory and Best Practices*. Archaeopress, p.171, ISBN 978-1-4073-1230-9.
- [4] Bayaram, B. et al., 2015. *Comparison of Laser Scanning and Photogrammetry and Their Use for Digital Recording of Cultural Monument Case Study: Byzantine Land Walls-Istanbul*. The ISPRS Annals of Photogrammetry, Remote Sensing and Spatial Information Sciences, I-3, p. 17-24, Taipei.
- [5] Grussenmeyer, P. et al., 2008. *Comparison Methods of Terrestrial Laser Scanning, Photogrammetry and Tacheometry Data for Recording of Cultural Heritage Buildings*. The International Archives of Photogrammetry, Remote Sensing and Spatial Information Sciences, 37(B5), p. 213-218, Beijing.
- [6] Skarlatos, D.; Kiparissi, S., 2012. *Comparison of Laser Scanning, Photogrammetry and SFM-MVS Pipeline Applied in Structures and Artificial Surfaces*. The ISPRS Annals of Photogrammetry, Remote Sensing and Spatial Information Sciences, I-3, p. 299-304, Melbourne.
- [7] Matoušková, E., Hůlková, M. and Šedina J. A. HISTORICAL PLASTER COMPOSITION DETECTION USING REFLECTANCE SPECTROSCOPY. *Stavební obzor - Civil Engineering Journal* [online]. 2016, **25**(4), - [cit. 2017-02-26]. DOI: 10.14311/CEJ.2016.04.0023. ISSN 18052576. Dostupné z: [http://www.civilengineeringjournal.cz/archive/issues/2016/2016\\_4/4-2016-0023.pdf](http://www.civilengineeringjournal.cz/archive/issues/2016/2016_4/4-2016-0023.pdf)
- [8] Pavelka, K.; Hůlková, M.; Matoušková, E.; Havlín, J. *Exploration of the Charles Bridge in Prague by GPR and TLS Technology*. Interdisciplinarity in Theory and Practice. 2016, 2016(11), 264-268. ISSN 2344-2409. Dostupné z: <http://www.itpb.eu/index.php/ct-menu-item-3/14-engineering/406-11-cislo-clanok-50>
- [9] VESELÝ, Jan. *Měřická dokumentace historických staveb pro průzkum v památkové péči*. Praha: Národní památkový ústav, územní odborné pracoviště středních Čech v Praze ve spolupráci s Národním památkovým ústavem, generálním ředitelstvím, 2014. ISBN 978-80-86516-79-0.
- [10] BERÁNEK, Jan a Petr MACEK, ed., 2015. *Metodika stavebněhistorického průzkumu*. Odborné a metodické publikace. Praha: Národní památkový ústav, generální ředitelství. ISBN 978-80-7480-037-5.